Mechanical Properties of Nickel-based Superalloys A Multiscale Atomistic Investigation

Bianchini, Federico

Awarding institution:
King's College London

Mechanical Properties of Nickel-based Superalloys

A Multiscale Atomistic Investigation

Federico Bianchini

Department of Physics

King's College London
United Kingdom

A thesis presented for the degree of
Doctor of Philosophy

5th August 2016

Declaration of Authorship

I, Federico Bianchini, declare that this thesis is the result of the work undertaken between September 2012 and May 2016 at the Department of Physics, King's College London under the supervision of Prof. Alessandro De Vita. I certify that this thesis is the result of my own work and that ideas from the work of other people have been acknowledged. This thesis has not been previously submitted, in whole or in part, for any degree or diploma at this or any other university.

Part of the work presented here was published:

- F Bianchini, J R Kermode and A De Vita, "*Modelling defects in Ni–Al with EAM and DFT calculations*", Modelling and Simulation in Materials Science and Engineering, Volume **24**, Number 4

Signed

Date

Abstract

Nickel-based superalloys are high performance structural materials that exhibit excellent strength and creep resistance at high temperatures, even in chemically aggressive environments. This makes them ideal for use in the construction of efficient turbines for energy generation or aerospace applications. These superalloys are usually manufactured as single crystals, with their high strength resulting from dislocation pinning at interfaces between the fcc matrix an $L1_2$-ordered precipitates. Chemical impurities such as rhenium also affect dislocation mobility, and their inclusion in commercial materials is standard practice. However, there is currently no detailed understanding of the atomic-scale mechanisms underlying these processes. This problem is here addressed at the atomistic level. The typical accuracy level of first principle methods is required to describe bond breaking in the distorted region surrounding a dislocation core and for including impurities in the fcc matrix, but model systems must be large enough to accommodate the strain gradients typical of long-range elastic interactions due to the presence of dislocations. Multiscale methods are therefore required for simulating these chemo-mechanical processes. The 'Learn on the Fly' (LOTF) technique is a non-uniform precision quantum mechanical/molecular mechanical approach. It offers a predictor/corrector algorithm for speeding up calculations, and the possibility of modelling a moving quantum region, useful for fast dislocation motion due to high simulating temperature or load condition. The scope of this thesis is to apply this method to metallic systems to conduct, for the first time, quantum mechanical accurate simulations of dislocation motion in Ni-based alloys. The QM/MM method corrects the deficiencies of the classical interatomic potential related to inaccurate energetics for the hcp phase, relevant to the geometry of dislocation cores, and it is capable of reproducing the correct separation between Shockley partials at high temperature conditions.

Acknowledgement

I would like to thank my supervisor, Prof. Alessandro De Vita, for giving me the possibility of following this path, for his enthusiasm and for sharing his experience. I am deeply grateful to the US Air Force for funding my PhD project European Office of Aerospace Research and Development. I also wish to acknowledge discussions with Lt Col Randall 'Ty' Pollak (EOARD, London) and Dr. Christopher Woodward (Wright-Patterson AFB, Dayton, OH) for discussions and encouragement during the project. Many thanks to Dr James Kermode for 'updating' my expertise in computational Physics, for guiding me during the first stages of my project and for proofreading this work. Many thanks to Julia Kilpatrick for sorting out the bureaucratic work.

I am grateful to the people that made my experience at KCL more enjoyable, in particular the 'old school' PhD students: Massimo, Giovanni P, Nick, Giovanni D, Luca, Zhenwei, Paolo, Tevong and Spyros. Special thanks to the Sunday workers, Alena and Thomas, for keeping me company during the thesis writing sessions, and to the 'Seminar Room heroes': Gianmarco, Dom, Marcello, Pooya, John, Lorenzo and Josep. I would like to thank the following people for 'saving me from boredom during office hours': Dan, Max, Martina, Mateusz, Krzysiek, Katy, Chiara, Chakrit. Special thanks to Marco for being my desk neighbour for almost four years, and to my new neighbour, Henry, for proofreading this work. I wish good luck to the new generation of KCL PhD students Aldo, Kevin, Patrick, Stefano, Claudio.

I would like to extend my gratitude to the people outside the microcosm of KCL Physics, in particular to my good friends Andrea and Maria. Special thanks to the people from my wild homeland that managed to find me even though I was hiding in a big city: Carlo, Sandro, Teno, Simone, Alessandro.

Finally, I would like to thank my family (Gerardo, Maria Bruna, Sara, Giuliana, Giampaolo, Livio) for their continuous support and my amazing girlfriend Lill-Grethe for taking good care of me.

Contents

List of Figures

List of Tables

Acronyms

APB	Antiphase Boundary
APT	Atom probe Tomography
BZ	Brillouin Zone
CSF	Complex Stacking Fault
DFT	Density Functional Theory
DOS	Density of states
DXA	Dislocation Analysis
EAM	Embedded Atom Method
ESF	Extrinsic Stacking Fault
EXAFS	Extended X-ray Absorption Fine Spectroscopy
GGA	Generalised Gradient Approximation
GSF	Generalised Stacking Fault
IP	Interatomic Potential
LDA	Local Density Approximation
LOTF	Learn on the Fly
MD	Molecular Dynamics
MM	Molecular Mechanics
MP	Monkhorst Pack
NEB	Nudged Elastic Band
n.n.	Nearest Neighbours
n.n.n.	Next Nearest Neighbours
IPB	Interphase Boundary
ISF	Intrinsic Stacking Fault
OBC	Open Boundary Conditions
PAW	Projector Augmented Wave
PBC	Periodic Boundary Conditions
PBE	Perdew Burke Ernzerhof
PDoS	Projected Density of States
PES	Potential Energy Surface
QM	Quantum Mechanics
QM/MM	Quantum Mechanics / Molecular Mechanics
scf	self-consistent field
SISF	Super Intrinsic Stacking Fault
SP	Shockley Partial
STEM	Scanning Transmission Electron Microscope
TEM	Transmission Electron Microscopy
USF	Unstable Stacking Fault
XC	eXchange Correlation

CHAPTER 1

Introduction

Nickel based superalloys are high performance structural materials, manufactured as single-crystals for the production of turbine blades for energy generation and aerospace applications [1; 2]. The high strength of this class of materials is due to the precipitation of a $L1_2$-ordered phase, denoted γ', within the fcc γ matrix. Elementary cubic cells for these two phases are reported in Figure 1.1. Dislocations are pinned at the semicoherent interphase boundary, relieving the lattice misfit strain and strengthening the alloy. Vacancies are emitted or absorbed by dislocations climbing at this interface, changing the morphology of the material through a mass transfer mechanism. Chemical impurities, such as rhenium, are known to greatly improve the plastic response of the material at high temperature conditions. However, adding these impurities is expensive, and there is currently no detailed understanding of the atomic-scale mechanisms underlying these processes.

The goal of this project is to provide fundamental insight at the nanoscale, allowing for the design of materials with improved properties, with the ultimate objective of raising the operational temperatures (and, thus, the engine efficiency) and at the same time the turbine lifetime. The problem is extremely complex if approached from an atomistic perspective: quantum-accurate methods, such as Density Functional Theory (DFT) [3], are required

to accurately describe chemical impurities and atoms at the dislocation core. At the same time, the system must be large enough to accommodate the strain gradients typical of long-range elastic interactions. For this reason, the current state of the art of atomistic methodology for the description of processes relative to superalloy plasticity is limited to the usage of interatomic potentials. While these approaches, based on a parametrisation of the Embedded Atom Method (EAM) [4] produced by Y. Mishin [5], provide insight on dislocation interactions at the interphase boundary (IPB) [6], they are unable to characterise the chemical complexity of the alloy.

This issue is here addressed by the usage of non-uniform precision techniques, such as the 'Learn on the Fly' (LOTF) scheme [7], which would guarantee DFT-level accuracy and chemical transferability, and computational efficiency due to the predictor/corrector scheme implemented to avoid unnecessary electronic structure calculations while propagating the dynamics. This promising method, successful in describing the fracture of Silicon [8], has not been extensively applied to metallic systems [9]. Its validation in the case of superalloys is therefore crucial.

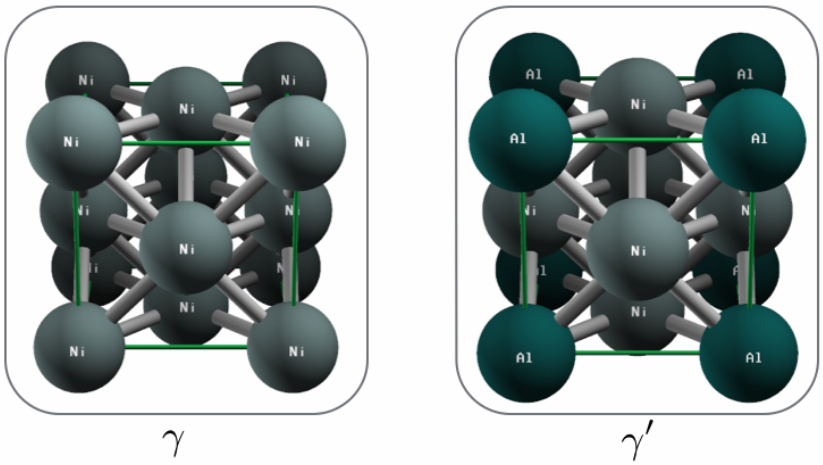

Figure 1.1: Conventional cubic cells for γ and γ'.

The main focus of this thesis is the calculation of a number of properties of these systems, comparing DFT and EAM results. Crucial testing for parameters of the embedding scheme is then performed, and the LOTF scheme is used to model matrix dislocations at different conditions (temperature, stress and chemical complexity). A significant improvement with respect to the results from the classical interatomic potential is found in the local description of dislocation core geometries.

This thesis is structured as follows:

- In Chapter 1 a general introduction to the work is provided, together with a detailed literature review comprising of three sections. The first two are strictly related to Ni alloys, describing their main deformation mechanism and the experimental and theoretical investigation of the 'rhenium effect'. In the third section a brief review of the existing methodologies of non-uniform precision simulations of plasticity in metallic systems is provided, and some links to higher scale models are provided.

- The theoretical foundations to this work are provided is Chapter 2. Methods based on Quantum Mechanics (QM) are briefly described, focussing on DFT and on the approximations used for practical electronic structure calculations. The interatomic potentials of the EAM class are described, according to the parametrisation provided in Reference [5]. A brief description of algorithms used for integrating the equations of motion, performing structural optimisation and exploring reaction coordinates is provided. Finally, non-uniform precision techniques are introduced, with particular focus on the LOTF method. Given the large number of topics included in the Chapter, the descriptions are not complete by any means, and are are supposed to provide a quick reference to people inexperienced in this atomistic simulations field.

- In Chapter 3 a selection of structural and electronic properties of Ni alloys, evaluated using both DFT and EAM, is presented with the aim of characterising simple bulk structures while verifying the overall accuracy of the interatomic potential. A selection of defects relevant to superalloys is characterised, including vacancies and chemical impurities (Re, Al, W). Some transferability issues of the EAM potential are found, affecting the calculation of (i) the elastic energy of Ni hcp and (ii) the adhesive energy of an isolated Al atom in the γ matrix. Finally, a detailed study of the generalised stacking fault energy surface, important to determine dislocation properties, is provided, focussing on the effect of chemical impurities.

- Chapter 4 is dedicated to the study of matrix dislocations, using the EAM potential. A brief theoretical part is included, describing the Nye tensor technique for tracking the core of dislocations by comparing the deformed lattice with a perfect fcc reference. The capability of tracking a dislocation core during a simulation at high temperature is necessary for defining and updating the quantum region to be used in the QM/MM embedding scheme. The phonon drag model is then introduced, and glide velocities for a screw dislocation are calculated as a function of stress and temperature. A γ/γ' interphase boundary is then modelled, and dislocation pinning is studied.

- Chapter 5 is fully dedicated to the development of a LOTF scheme for metallic systems. Crucial testing of the QM region size is provided, together with the average EAM error with respect to reference DFT calculations. This study is performed for a number of γ phase defects including dislocation, vacancies and impurities. The scheme is then extended to the α phase of iron, a more challenging material due to its magnetic properties. Finally, the LOTF scheme is applied to the glide process of screw dislocations in the γ matrix, where it corrects

a deficiency of the EAM potential, related to the elastic properties of the hcp phase and therefore influencing the average distance between Shockley partial dislocations.

- In Chapter 6 some concluding remarks are made, and some prospects for future work are outlined.

Technical Notes

Density Functional Theory calculations are performed using VASP [10; 11]. More details can be found in Section 3.1. Interatomic potentials based on the embedded atom method are used for classical calculation, following the parametrisation of Reference [5] for Nickel and [12] for Iron. Rendering of atomic system is done using Ovito [13]. Data are plotted using either gnuplot [14] or matplotlib [15]. These libraries are used also for fitting of data.

I acknowledge PRACE for awarding access to resource Fermi based in Italy at Cineca and Juqueen based in Germany at Jülich Supercomputing Centre. An award of computer time was provided by the Innovative and Novel Computational Impact on Theory and Experiment (INCITE) program. This research used resources of the Argonne Leadership Computing Facility, which is a DOE Office of Science User Facility supported under Contract DE-AC02-06CH11357. I acknowledge King's College London for the access to local parallel supercomputers (Capablanca, now decommissioned, and Ada).

1.1 Literature Review

Deformation Mechanisms

Single crystal Ni superalloys turbine blades, first introduced during the 80s on military engines, allowed for a significant increase in the operational temperature and in the velocity of the rotor [16]. They are characterised by the absence of grain boundaries in the material, and by the higher volume fraction of ordered intermetallic precipitates (γ') in the γ matrix. The creep deformation of these materials presents a strong dependence on temperature, stress and orientation of the crystal.

In Reference [17] a characterisation of a CMSX-6 commercial alloy is provided for a $\langle 110 \rangle \{001\}$ shear system. During the primary creep phase (low stress, medium temperature), the glide of the system is associated with microscopic slip systems of the $\frac{a}{2}\langle 110 \rangle \{111\}$ type, restricted to the γ channels. Dislocation lines are straight in the γ corridors, but curve along the [001] direction while approaching the edge of a cuboidal precipitate. Dislocations with cubic Burgers vector $a\langle 100 \rangle$ are observed. Their role is not important during primary creep, but at a later stage they can penetrate the precipitates [18]. During this stage of creep the edges of the cuboidal precipitate start to round off, but rafting (transition from cuboidal precipitates to lamellar structure, as exemplified in Figure 1.2) is not observed.

During secondary creep the morphology of the alloy evolves. The γ-channels become narrow, and the precipitates start to lose their cuboidal shape. The interphase boundary becomes covered with a dislocation network, relieving the strain due to lattice misfit and preventing dislocations cutting through the precipitate [19]. As rafting takes place, the dislocation network follows the shape of the evolving γ' precipitates. A combination of climb and cross-slip processes is associated with the evolution of the network, originally generated during primary creep by glide mechanisms [17].

A schematic model for rafting is given in Figure 1.2. The flux of vacancies is due to dislocation climb at the interphase boundary.

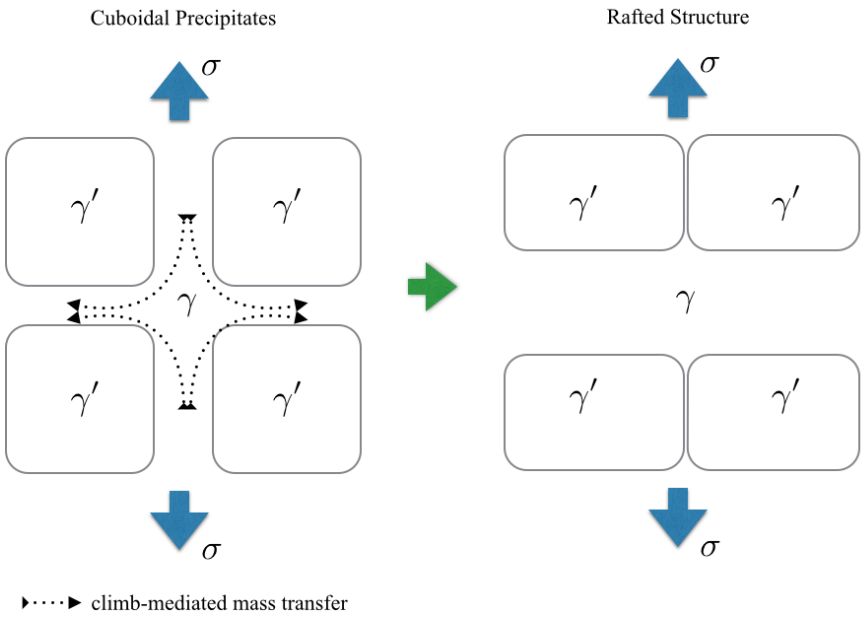

Figure 1.2: Schematic model for rafting due to material transport caused by diffusing dislocations.

A simplified scheme for this process is provided in Figure 1.3. Matrix dislocations glide on {111} planes towards the cubic precipitates and are pinned at the interface. In order for a dislocation to continue its motion, a climb event has to occur, involving vacancy absorption or emission, as exemplified in Figure 1.3. On average, the number of emitted and absorbed vacancies is the same. This mass transport mechanism results in rafting of the material, as shown in Figure 1.2. This model is proposed in Reference [20] and used to rationalise the effect of γ phase impurities. The precipitate is assumed to be impenetrable (low stress regime).

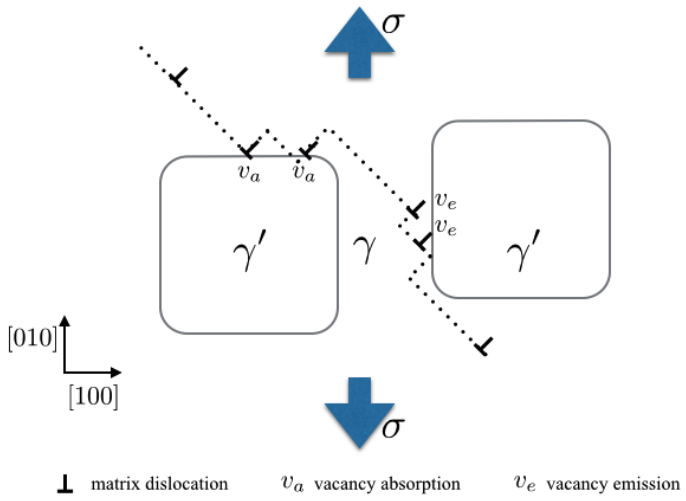

Figure 1.3: Schematic model for climb-assisted glide of matrix dislocations.

Tensile creep tests on specimen of CMSX-4, presented in Reference [21], prove that there is a threshold of about 0.5 GPa after which primary creep (as opposed to rafting) is observed. This deformation is associated to the propagation of $a\langle 112\rangle$ dislocation ribbons (also known as super dislocations), capable of penetrating the γ' phase. These structures originate in the γ channels from two matrix dislocations with an angle of 60° between their respective Burgers vectors. Cubic dislocations cutting the precipitates are also observed, e.g. in Reference [22] for a CMSX-6 alloy, at a low stress high temperature regime.

Molecular dynamics simulations of relevant processes in these systems are notoriously challenging, because of the geometrical complexity of dislocated region, and because of the chemical complexity of the alloys. In Reference [23] a classical interatomic potential based on the Embedded Atom Method (EAM) is used to study dislocation nucleation processes at the interphase boundary. An idealised periodic system is used. The lattice mismatch between the matrix and the precipitates is neglected, and several cubic pre-

cipitates are included in the matrix. The resulting trajectories show a loop of partial dislocations nucleated at the corner of a precipitate. Dissociation into Shockley partial dislocations is observed upon emission in the γ channel. The emitted dislocation glides in the matrix phase, until it is pinned at another interphase boundary. In References [24; 25] large supercells are created to model misfit dislocations using three dimensional periodic systems. Structural and energetic properties are investigated for a selection of orientations of the γ/γ' interface. The Voter Chen potential [26] used in that work predicts the incorrect energetic ordering for the interfaces, stating that $\{111\}$ interphase boundaries are the most favourable, in disagreement with experimental data and *ab initio* calculations (cf. for instance Reference [27]). More recently, in Reference [28], the interaction between matrix dislocations and the misfit dislocation network is studied, using the interatomic potential developed in Reference [5], recognised to be the most accurate for γ/γ' geometries. The misfit network is found to act as a sink of matrix dislocations. This hinders pile up at the interface, strengthening the material. Some cubic dislocations are formed upon recombination of the network, confirming the experimental findings of Reference [22]. Whenever a series of successfully emitted screw dislocations glides towards the interphase boundary, the network is capable not only of absorbing part of them, but also of creating pinning points, preventing them from gliding away. The state of the art of atomistic modelling of plasticity processes in superalloys can be observed in the recent work presented in Reference [6]. The idealised simulation cells, periodic and with sharp interphase boundaries, are abandoned in favour of more realistic systems, designed starting from experimental atom probe tomography results. The effect of the interface curvature is studied. Super dislocations with an $a\langle 112\rangle$ Burgers vector, capable of cutting into the precipitate, are observed, and the presence of Lomer-Cottrell [29] locks at the interface, observed by transition electron microscope experiment in Reference [30], is verified.

The role of rhenium

The addition of rhenium is known to enhance the high-temperature properties of single-crystal Ni-based superalloys, allowing the construction of more durable turbine blades and an improved energy efficiency. The so called 'rhenium effect' is so important that, since its discovery in the late 70s, superalloys are classified according to their rhenium content. Superalloys without rhenium are referred to as 'first generation superalloys'. The second generation of superalloys, manufactured during the 90s, is characterised by 2–3 wt.% Re content. In third generation materials, developed during the 00s, the rhenium percentage is as high as 5–6 wt % [1]. rhenium strongly partitions to the γ phase, where it is thought to affect dislocation mobility thus improving the plastic response of the material [31]. This is particularly important at the tertiary creep regime, observed beyond 1100 K for stresses below 500 MPa. At this conditions, dislocations are confined to the matrix channels, and climb-assisted glide has to occur to make them transit around the precipitate and thus contributing to the deformation of the crystal [1]. Fourth and Fifth generation superalloys benefit from the inclusion of ruthenium, which causes refractory elements (such as Re) to partition more strongly to the γ' phase, reducing the formation of topological close packed phases in γ and giving an overall better performance.

The first observation of the beneficial effects of rhenium in single-crystal superalloys is reported in [32]. A lower γ' coarsening kinetics is observed for increasing percentage of rhenium, due to the fact that this element is the slowest-diffusing transition metal [33; 34; 35] and it partitions to γ phase, as verified by scanning transmission electron microscope (STEM) and X-ray analysis microstructure characterisations [36]. This results in longer rupture lives at operating high-temperature conditions, when directional coarsening (rafting) becomes problematic [37]. Whereas this effect is well understood, the strengthening effect observed during tertiary creep is not yet explained from a microscopic perspective [38]. This understanding would improve the

design of materials for high temperature applications. In this Section a general revision of the experimental and theoretical efforts made to investigate this issue is provided.

The first hypothesis on the atomistic mechanism responsible for the 'rhenium effect' originated from the atom probe work presented in Reference [39]. The one dimensional analysis of the sample confirmed the partitioning of rhenium to the γ phase. Cumulative profiles of its distribution revealed the presence of discontinuities, associated with clusters of ~ 1 nm diameter. The presence of these extended defects within the fcc phase can influence the plastic response of the system, effectively hindering glide and climb processes of matrix dislocations. Note that, due to the lack of three dimensional resolution of the experimental technique employed, the obtained results predict short-range ordering, not necessarily clustering of rhenium. A subsequent experimental work, also based on one dimensional atom probe, confirms the presence of either short-ordering distribution or clustering of rhenium atoms in the matrix [40]. This study also provides extra information about the distribution of other impurities in CMSX-4 alloys. The γ/γ' interface is found to be sharp, and enriched with Ti for reducing the lattice mismatch.

The advent of the three-dimensional atom probe allowed for a better investigation of impurities within alloys. In Reference [41] this technique is used to characterise RR3000, a third-generation Ni-based alloy. For the first time instruments with sufficient mass resolution to distinguish between Re, W and Ta are employed. No evidence of rhenium clustering is found. This element is found to pile up at the γ/γ' interphase boundary, both for the cuboidal γ' particles (primary precipitates) and the spherically-shaped fine dispersion between these, known as secondary precipitate. This is an expected result as, upon cooling from service temperatures, both the precipitate phases grow at the expense of γ, Re is ejected because of its partitioning properties. This phenomenon cannot be the cause for the 'rhenium effect', as it is related to cooling from high temperatures. A different chemical com-

position between primary and secondary precipitates is found. The main rafts are Ta enriched, while the secondary ones contain more Al. The latter form upon cooling, and Ta has an higher diffusion barrier with respect to Al. A successive study presented in [42] on a RE31 alloy, based on TEM and on three dimensional atom probe techniques, confirmed the presence of short-range ordering of rhenium. A clear distinction between clusters and statistical scatter is not observed. Rhenium atoms distribute according to a quasi-periodic structure of about 20 nm wavelength. More recent experimental work based on 3DAP studies has been carried out [43] in order to investigate the presence of rhenium clusters. A number of different Ni–X binary alloys is considered, and a friends-of-friends algorithm used to investigate the presence of impurity clusters. Clustering is not observed for any of the atomic species considered (Ta, W, Re, Ir and Pt), and similar results are obtained upon repetition of the experiment on a CMSX-4 alloy, for which Re-enrichment at the interface is observed upon cooling as in [41]. Rhenium clustering in Ni superalloys was also investigated using extended x-ray absorption fine spectroscopy (EXAFS) [44; 45]. With this technique the local environment of an atom can be determined by studying the oscillations in x-ray absorption coefficient. In both cases, the nearest neighbours of Re are found to be Ni atoms. Rhenium clustering is not observed in modern days experiment, consistently with the fact that this element is found to have a low impact on low-temperature properties, as demonstrated in Reference [46] by means of instrumented indentation techniques on binary alloys.

Theoretical modelling also contributed to clarify the rhenium clustering issue. Density functional theory is used in Reference [47] for calculating Re–Re binding energy, finding that configurations in which rhenium atoms are nearest neighbours are energetically unfavourable, in full agreement with the EXAFS measurements [44; 45]. The Re–Re binding energies go rapidly to zero for increasing distances between the impurity atoms. This implies that the Re–Re interaction has a local character, and short range ordering

is possible, as observed with atom probe techniques. Further investigation of the Ni–Re phase diagram via first principle techniques are carried out in References [48; 49]. In the first work [48], density functional theory is used to explore Re–X alloys. In the Re–Ni case, two stable configurations are found, Ni_4Re and $NiRe_3$, with symmetries $D1_a$ and DO_{19} respectively. The latter configuration is found to be energetically favourable, but its existence does not apply to superalloys as the local density of rhenium is never as high as 75%. In Reference [49] a cluster expansion method is used, based on DFT data, to explore all the symmetrically inequivalent configurations that can be obtained using a basis of 20 atoms for different concentrations of Re (0–33%). Also in this case, a Ni_4Re $D1_a$ phase is found to be stable at low temperatures. The existence of this phase is shown to be consistent with the EXAFS data presented in [44]. This phase was not previously included in the Ni–Re phase diagram [50], and its existence at low temperature can explain the short-range ordering of Re within the γ matrix. This quasi-periodicity can play an important role, as the rhenium clusters are not favourable and an isolated vacancy has a negligible effect on dislocation glide. The only theoretical result predicting rhenium clustering is presented in Reference [51]. The calculations are based on a ternary MEAM potential, capable of describing Ni-Re-Al alloys. The lattice parameters evaluated with this potential show a non-negligible deviation with respect to DFT data, and therefore its results are not completely reliable, as pointed out in Reference [47]. On top of that, the interatomic potential does not predict the partitioning of Re, in disagreement with all the available experimental evidence.

A second atomistic interpretation for the 'rhenium effect' was also formulated [20; 43; 44; 47]. At operating conditions, creep plasticity in superalloys is limited to the γ phase, and dislocations move along the interphase boundary by means of a thermally-activated climb process, ruled by the rate at which vacancies are emitted and reabsorbed. The rate is significantly reduced by the presence of slow-diffusing atoms [20]. rhenium is shown to be

the element with the slowest diffusion rate when compared with other typical elements added to superalloys [33; 34], its diffusion rate being one order of magnitude smaller with respect to tungsten. This is due to the formation of directional *d* Re–Ni bonds, which are less compressible, and therefore hinder the diffusion of these chemical impurities [35; 52]. The quantitative effect of local chemistry on dislocation climb rate is also important from a multiscale perspective, as this data would fit modern implementations of Discrete Dislocation Dynamics (DDD) capable of an explicit description of this process [53; 54]. Density functional calculations for this are presented in References [55; 56] for different impurity atoms (Re, W, Ta, Mo). The diffusion coefficient shows a dependence on chemistry which is not large enough to explain the great strengthening due to the presence of rhenium. Rhenium affects also in another way dislocation climbing at the γ/γ' interface. Dislocations in fcc crystals are usually dissociated into Shockley partials, which have to constrict in order to climb or to cross-slip [1]. Their distance is proportional to the inverse of the intrinsic stacking fault energy [29], which is lowered by the presence of chemical impurities, as can be appreciated from the TEM images presented in Reference [57]. A longer distance between partials would retard dislocation recombination and therefore hinder the climbing of dislocation. This effect is included in the model presented in Reference [31], based on DFT calculations for the stacking fault energy. This phenomenon does not explain the 'rhenium effect', as tungsten has a larger effect on the stacking fault energy with respect to rhenium [31; 58]. It is therefore evident that an isolated rhenium atom cannot be the cause of the great strengthening observed during tertiary creep. An explanation for the 'rhenium effect' can arise from the short-range ordering of this element in the matrix, that can form vacancy traps, as suggested in Reference [55], thus reducing climb velocities.

Non-uniform precision Simulations of Metallic Systems

The first non-uniform precision model for a dislocation in a metallic system was proposed by S.I. Rao and C. Woodword in Reference [59]. The atomistic simulations are coupled to continuum modelling by means of flexible boundary conditions implemented within the lattice Green function formalism, originally proposed in Reference [60]. This method is general and can be incorporated into several potential interaction schemes, either QM or MM. With this technique accurate results are obtained using a simulation cell whose radius is the same as the core QM region, corresponding to a 90% reduction of the atomistic region [59]. The analytic form of the lattice Green function can be modified in order to match the periodicity of the system, allowing for simulations of 2D (periodic along the dislocation line) and 3D systems, required to study dislocation defects such as kinks and jogs.

The method has been applied to a variety of cases. In the first implementation [59], screw dislocations in Ni and Fe are modelled using EAM potentials. For the Ni system, the 2D implementation is used, and the dependance of the distance between Shockley partial dislocation on the system size is studied. The distance obtained using a minimal system and flexible boundary conditions matches the one obtained for a much larger simulation cell and fixed boundaries condition, validating the approach. In the case of Fe, where a 3D system including a kink is simulated, accurate results are also obtained using systems 90% smaller with respect to the typical size required for traditional techniques. In Reference [61] the method is used for a 3D Ni system to study the energetics of cross-slip processes, using again an EAM potential. In References [62; 63] the scheme is extended for the first time to DFT calculations. The equilibrium core structure of isolated $\frac{a}{2}\langle 111\rangle$ screw dislocations in bcc Mo and Ta is calculated, finding a symmetric spread on three conjugate (110) planes. Converged results are obtained using 2D systems with less then 200 atoms. A successive DFT study [64] on a $\frac{a}{2}\langle 110\rangle\{111\}$ screw dislocations in γ TiAl predicts a non-planar core region.

A similar configuration is also found in the case of fcc iridium, although unfavourable with respect to the planar one, in Reference [65] using an implementation of the flexible boundary conditions method to a bond-order potential. Transformation from one minimum to the other occurs under applied stresses that reduce the distance between SPs. Thermal activation or full constriction of the partials are not required, and the cross-slip rate is thus much higher with respect to other fcc systems. Equilibrium structures for edge and screw dislocations in fcc Al are presented in Reference [66], using again DFT. This work helps validate IPs; in particular their capability for reproducing the distance between SPs. The more accurate one is found to be the EAM parametrisation of Y. Mishin, presented in Reference [67]. Other EAM-based potentials [68] greatly overestimate this distance.

The DFT implementation of this Green function flexible boundary conditions method has full chemical transferability, and can be used to study dislocation cores and their response to an applied strain. See Reference [69] for a modern review of the method. Results obtained with this technique can be used to inform large scale methods. In Reference [70] a continuum analytic model is used to study the softening of bcc molybdenum as a function of Re and Pt concentration over a range of temperatures. The model is informed by DFT flexible boundary conditions calculations, used to compute the interaction energies between screw dislocation and chemical impurities. This energy landscape is used to parametrise the double-kink nucleation and kink-migration enthalpy barriers, thus fully characterising the plastic deformation of the alloy at low temperature. Similarly, in Reference [71] an analytic model of strengthening of fcc Al is parametrised using the interaction energies between dislocations and impurities. These *ab initio* energies are used to balance the line tension due to the formation of kinks, allowing for an accurate description of dislocation motion at different strain regimes. The yield stress is thus calculated as a function of the alloy composition.

Another multi-precision technique coupling QM-based atomistic simulations to continuum modelling in described in Reference [72]. A finite element method mesh is used for the continuum embedding, effectively replacing the analytical lattice Green function with numerical solutions of continuum deformation. The DFT calculations are performed on a cluster system, comprehensive of the core QM region and a buffer region used to decouple the former from surface effects. Within this approach, a fixed, large atomistic QM region is used, as opposed to the minimal and adjustable one typical of the LOTF method [73]. The size of the typical QM systems make the self-consistent calculation hard to converge, so much so a very large gaussian smearing width (1 eV) is used. Despite this approximation, the method, named quantum mechanics coupled atomistic discrete dislocation (QM-CADD), is very successful in reproducing the equilibrium geometry of a screw dislocation in aluminium, matching the results obtained in Reference [66] using the lattice Green function. This recently developed technique is used for predicting the critical stress required for nucleating a partial dislocation at the crack tip of an Al crystal, and for determining the effect of surface impurities on this process [74]. It is found that atoms exhibiting a strong electronegativity, such as oxygen and hydrogen, increase the critical nucleation load. Hydrogen is identified as the material with the most effect on dislocation nucleation: its presence leading to crack advancement by a single atomic spacing and dislocation nucleation on the newly exposed slip plane. This effect is found to have a purely electronic origin, as it is related to localised charge transfer, measured by means of Bader analysis [75]. The advancement of the crack is not observed in any other case. A continuum Peierls model to predict the critical load at which a dislocation will nucleate from the crack tip is also implemented, informed from QM calculations of the stacking fault energy curve. Critical nucleation loads predicted using this model are in good agreement with the QM-CADD simulations.

These multi-precision QM-continuum models can be very accurate, and allow for a complete characterisation of relaxed dislocation core structures in a chemically complex environment, under different stress conditions. However, these methods have a major drawback: the inability in describing finite temperature effects [64] for which a QM/MM atomistic simulation is perfectly suited. The two methods appear to be complementary, as the first one aims at the description of the equilibrium structure, whereas QM/MM methods are in general less accurate (e.g. because of the error due to buffer size in force mixing-schemes) but capable of describing the evolution of the system at high temperature.

Two energy-mixing QM/MM schemes are applied to a metallic system (screw dislocation in Al) in Reference [76]. These two methods use different definition of the interaction energy between the QM and the MM regions. The simplest scheme is based on the ONIOM formulation [77] (cf. Equation (2.78)). Forces in the MM region are fully determined by the lP, while forces in the QM zone are determined by both classical and quantum energetics, supposed to provide cancellation of errors at the surface of the cluster. This method is found to be not particularly accurate in reproducing the QM charge density. On the other hand, it is suitable for the modelling of chemical impurities, as a MM parametrisation is not required (provided that the defect is not close to the surface of the QM cluster). Within the second method devised, the interaction energy is evaluated using the Orbital Free Density Functional Theory (OF-DFT) method [78]. The QM region is still modelled using traditional Kohn-Sham DFT, so that this QM/MM approach effectively employs three calculators. Forces in the QM are in this case fully determined by the QM engine, and the charge density is accurately reproduced and joined smoothly with the MM density supported by the embedding-atom picture [4]. Remarkably, this method gives less accurate results in the MM region, due to a non-vanishing contribution of the interaction energy.

The traditional ONIOM scheme devised in Reference [76] is extended in a successive work [79], combining it with a quasi-continuum method [80]. The technique is applied to the study of the equilibrium geometry of the core of an edge dislocation in aluminium. The separation between SPs is found to be $\sim$ 5 Å, in contrast with the EAM prediction of $\sim$ 15 Å. These results were subsequently confirmed by both lattice Green function and QM-CADD methods [66; 72]. In addition, the effect of hydrogen on the dislocation core is investigated, finding an increased separation between SPs ($\sim$ 13 Å).

An improved QM/MM method is proposed in Reference [81]. The QM region is now surrounded by a set of buffer atoms. The DFT forces on these atoms are substituted with the MM ones, calculated for a system without surfaces. making this an abrupt force-mixing scheme The total energy of the system can still be defined by adding an energy correction, which, on the other hand, makes the Hamiltonian explicitly time-dependant. The total energy of the system is consequently not conserved. Nevertheless, the force errors are much reduced as compared with the ONIOM scheme.

More recently, the 'Learn on the Fly' (LOTF) scheme [7] has been applied to the study of nanoindentation and nanoscratching of single-crystal Cu [9], using tight binding as the QM calculator. Given the large size of the system requiring QM augmentation and of the buffer region, monoatomic QM regions are used, and the potential is locally refitted to each configuration. This implementation takes the name of 'divide and conquer' LOTF. Temperature (300 K) effects are explicitly included in the calculation for the first time, by means of a The Nosé–Hoover thermostat [82; 83]. It is found that, while the interatomic potential would favour amorphous plastic deformation in nanoindented Cu systems, the LOTF method predicts brittle fracture. However, the two method produced qualitatively similar result for macroscopic quantities, such as indentation or scratch hardness.

Future Challenges

Theoretical modelling is aimed at providing a basic understanding of alloy design and performance. A significant improvement of the simulation techniques has been recently observed, for both atomistic and mesoscale approaches. The creation of more realistic discrete dislocation dynamics algorithms, capable of modelling dislocation climb [54], helped elucidate the climb-assisted glide mechanism [84], relevant to low stress plastic deformation. From the atomistic viewpoint, geometrically complex γ/γ' interfaces are studied, modelled on experimental APT results [6]. This allowed for the simulations of more complicated dislocation arrangements, comprising Lomer–Cottrell lock. Techniques based on the embedding of an atomistic calculation in a continuum medium have been proposed [59; 72]. These works helped elucidate the effect of impurities on dislocation core geometries [71]. However, these approaches can not explicitly model thermal effects.

The next step is to design algorithms capable of a closer match with the stress/temperature conditions of experimental settings or practical applications, while retaining the chemical transferability of QM methods. This would allow for the understanding of complex mechanism, such as the one generating the rhenium effect. it has been proposed [55] that chemically complex vacancy trap can hinder dislocation mobility in the γ channel. While the exploration of this chemical space can be accomplished by means of DFT theory, calculations including the strain gradient typical of an IPB or extended dislocation cores, would benefit from multi-precision methods, which would allow the QM-accurate computation of quantities such as the drag coefficient for dislocation glide and the climb rate at the γ/γ' interface in presence of Re atoms. Mesoscale models based on the DDD model could then be parametrised using these data, in order to add chemical complexity to the approach. In addition to Ni alloys, a special effort is made by the community to explore the high temperature properties of Co-based single crystal superalloys [85].

CHAPTER 2

Theoretical Methods

2.1 Introduction

The aim of this Chapter is to provide a theoretical background to the thesis, focussing on typical simulation methods for atomistic system. The range of topics covered is large, as in this work ideas from both quantum and classical physics are employed.

In Section 2.2 Quantum Mechanics (QM) based approaches are described, underlying the typical approximations taken for electronic structure calculations and focussing on Density Functional Theory (DFT). I will then move (Sec. 2.3) to Molecular Mechanics (MM) methods based on interatomic potentials, focussing on the Embedded Atoms Model (EAM), widely used for simulating properties of metallic systems. In the following Sections I will describe how either QM or MM methods can be used to optimise atomistic structures (Sec. 2.5) or to simulate their dynamics within various thermodynamical ensembles (Sec. 2.4). The Nudged Elastic Band (NEB) method, used for calculating energy barriers between local minima of a given structure, is described in Section 2.6. Finally, in Section 2.7, I briefly examine the most common non-uniform precision techniques for QM/MM simulation, focussing on the 'Learn on the Fly' (LOTF) method.

2.2 The Quantum Approach

This section is devoted to explaining the main approaches based on quantum mechanics. The core problem is the solution of the Schrödinger equation

$$H|\psi\rangle = E|\psi\rangle \tag{2.1}$$

for a many-body system, described as an ensemble of atoms (nuclei and electrons) whose Hamiltonian H assumes the form [1]

$$\begin{aligned} H = &-\frac{1}{2}\sum_{i=1}^{n}\nabla_i^2 + \sum_{\substack{i,j=1\\ i<j}}^{n}\frac{1}{|\mathbf{r}_i-\mathbf{r}_j|} - \sum_{I=1}^{N}\sum_{i=1}^{n}\frac{Z_I}{|\mathbf{r}_i-\mathbf{R}_I|} + \\ &-\frac{1}{2}\sum_{I=1}^{N}\frac{\nabla_I^2}{M_I} + \sum_{\substack{I,J=1\\ i<j}}^{N}\frac{Z_I Z_J}{|\mathbf{R}_I-\mathbf{R}_J|} \end{aligned} \tag{2.2}$$

The lower case indices i, j are summed over electrons, the upper case ones I, J over the nuclei, n is the total number of electrons, N is the number of nuclei, $\{Z_I\}$ the charge of the nuclei, $\{\mathbf{R}_I\}$ and $\{\mathbf{r}_i\}$ the positions of nuclei and electrons. The first term represents the electronic contribution to the kinetic energy, while the fourth is the ionic one. Electron-electron and electron-ion interaction are described by the second and the third terms, while the last one is the potential energy due to the pure ionic interactions. This many-body problem has analytical solution only for the simple case of a hydrogen atom and can be numerically solved only for small systems. In the following pages I will describe the main approximations that are made to solve electronic structure problems. These calculations are called *ab initio* because they do not require empirical parameters, and are therefore highly transferable.

[1] In writing down the equation I use atomic units. Lengths are measured in Bohr and energies in Hartree. The charge of the electron is unitary, and so is its mass. The velocity of light in vacuum is $c = 137$

The Electron Density

The electron density, defined as the measure of the probability of an electron being present at a specific point in space, represents a crucial quantity for the *ab initio* description of an atomistic system. It is a scalar field depending on spatial variables. By definition, it is a non-negative quantity whose integral over the whole space returns the total number of electrons in the system. Its importance in modern day electronic structure is considerable, in light of the success of DFT over the last twenty years [3].

The electron density for a system with n electrons is formally defined as:

$$\rho(\mathbf{r}) = \sum_{s_1}\sum_{s_2}\cdots\sum_{s_n}\int d\mathbf{r}_2\cdots\int d\mathbf{r}_n|\Psi(\mathbf{r},s_1,\mathbf{r}_2,s_2,\cdots,\mathbf{r}_n,s_n)|^2 \qquad (2.3)$$

where $\Psi(\{r_i\},\{s_i\})$ is the normalised wave function, $\{\mathbf{r}_i\}$ the spatial and $\{s_i\}$ the spin coordinates for each electron. It can be conveniently rewritten as the expectation value of the density operator $\hat{\rho}(\mathbf{r})$, defined as

$$\hat{\rho}(\mathbf{r}) = \sum_{i=1}^{n}\sum_{s_i}\delta(\mathbf{r}-\mathbf{r}_i) \qquad (2.4)$$

where $\delta(\mathbf{r})$ is the Dirac delta function.

In electronic structure theories such an Hartree-Fock and density functional theory, where the many electron wave function is represented with a single Slater determinant, the electron density assumes the simplified form

$$\rho(\mathbf{r}) = \sum_{i=1}^{n} n_i|\phi_i(\mathbf{r})|^2 \qquad (2.5)$$

where ϕ_i is the atomic orbital and n_i its occupation number.

The Born-Oppenheimer Approximation

The Born-Oppenheimer approximation [86] allows decoupling of nuclear and electronic degrees of freedom, simplifying the many body problem defined in Equations (2.1), (2.45). Let us a consider a system with N atoms and n electrons, and rewrite equation (2.45) in the compact form:

$$H = T_e(\mathbf{r}) + V_{ee}(\mathbf{r}) + V_{Ne}(\mathbf{r}, \mathbf{R}) + T_N(\mathbf{R}) + V_{NN}(\mathbf{R}) \tag{2.6}$$

where T_e, T_N are the kinetic energy terms for electrons and nuclei respectively, V_{Ne}, V_{ee}, V_{NN} the sum of the two body interaction potential operators. The mixed term V_{Ne} prevents the separation of variables in Equation (2.6), which would allow to recast the wavefunction as the product of the eigenstates of the electronic and of the ionic problem $\Psi(\mathbf{R}, \mathbf{r}) = \psi(\mathbf{r})\chi(\mathbf{R})$.

The Born-Oppenheimer approximation is introduced at this point, stating that this separation of variables is physically correct to a certain extent, as electrons are much lighter than nuclei and can be assumed to immediately relax to their instantaneous eigenstate as the atomic spacial coordinates $\{\mathbf{R}_I\}$ are updated. The latter are thus taken as a parameter for the mixed interaction term, and the electronic problem is written as:

$$H_e|\psi_{\mathbf{R}}\rangle = E_{\mathbf{R}}|\psi_{\mathbf{R}}\rangle \tag{2.7}$$

where $H_e = T_e(\mathbf{r}) + V_{ee}(\mathbf{r}) + V_{Ne}(\mathbf{r}; \mathbf{R})$ is the electronic Hamiltonian. The quantity $E_{\mathbf{R}}$ is called the Potential Energy Surface (PES). It defines the potential field, due to the electrons, in which the nuclei are moving, via the equation

$$(H_n + E_{\mathbf{R}})|\chi_n\rangle = E_n|\chi\rangle \tag{2.8}$$

with $H_n = T_N(\mathbf{R}) + V_{ee}(\mathbf{R})$. This problem is usually solved using a classical approximation, using the forces obtained from the procedure defined by the Hellmann-Feynman theorem, described below.

The Hellmann-Feynman Theorem

The Hellmann-Feynman Theorem [87] provides a practical algorithm for evaluating the forces on atoms starting from the electron density. It proves that the derivative of the expectation value of a diagonal operator $\hat{O}_\lambda$ with respect to a parameter λ equals the expectation value of the derivative of the operator. This is formally written as:

$$\frac{dO_\lambda}{d\lambda} = \left\langle \psi_\lambda \middle| \frac{d\hat{O}_\lambda}{d\lambda} \middle| \psi_\lambda \right\rangle. \tag{2.9}$$

where O_λ and $|\psi_\lambda\rangle$ are respectively the eigenvalues and the eigenstates of the operator. The proof is trivial and follows directly from the orthonormality of the eigenstates.

In the context of atomistic QM calculations, the operator $\hat{O}_\lambda$ is the electronic Hamiltonian of the system (2.7), and the fixed parameters are the coordinates of the atoms. Once a set of eigenfunctions $|\psi_{\mathbf{R}}\rangle$ is found, the force acting on the atom I along the generic direction $\mathbf{x}$ is obtained as:

$$F_{X_I} = -\frac{\partial E}{\partial x_I} = -\left\langle \psi_{\mathbf{R}} \middle| \frac{dH}{dX_I} \middle| \psi_{\mathbf{R}} \right\rangle \tag{2.10}$$

where X_I is the projection along $\mathbf{x}$ of the coordinates of the I^{th} atom. This equation can be rewritten in terms of the electronic density as

$$F_{x_I} = -Z_I \int d\mathbf{r}\rho(\mathbf{r}) \frac{x - X_I}{|\mathbf{r} - \mathbf{R_I}|} + Z_I \sum_{\substack{I=1 \\ J \neq I}}^{N} Z_J \frac{X_J - X_I}{|\mathbf{R}_J - \mathbf{R}_I|} \tag{2.11}$$

The first term arises from the electron-ion interaction, while the second term is a constant depending only on the ionic positions. The evaluation of quantum mechanical forces is therefore easily performed once the electronic density has been calculated. In the following Section a common method for calculating this term is presented.

Density Functional Theory

Density functional theory (DFT) is a technique providing an approximate solution to many-body electron problems. It states that the properties of a many-electron system can be determined by expressing the energy of the system as a functional of the spatially dependent electron density $n(\mathbf{r})$.

DFT is one among the most popular and versatile methods available in condensed matter computational science, as a good agreement with experimental data can be achieved at a computational cost relatively low when compared to traditional methods based on the many-electron wavefunction.

Theoretical Background

The Hamiltonian of a system of N electrons subjected to an an external potential V_{ext} (e.g. due to the interaction with the nuclei) can be written in the schematic form:

$$H = T + U + V_{ext} \tag{2.12}$$

where T is the kinetic part and U the internal (electronic) potential. The first Hohenberg-Kohn (HK) theorem [88] proves that the ground-state electron density uniquely determines the external potential. The HK functional

$$F[n] = T[n] + U[n] \tag{2.13}$$

is therefore identical for all N-electron systems. According to the second HK theorem [88], $F[n]$ exists for any number of electrons and for any external potential $V_{ext}(\mathbf{r}) = \sum_{i=1}^{N} v(\mathbf{r} - \mathbf{r}_i)$. The energy functional

$$E_v[n] = F[n] + \int d\mathbf{r}\ v(\mathbf{r})n(\mathbf{r}) \tag{2.14}$$

obtains its minimal value at the ground state density, and this value is the total energy of the system.

While the HK theorems are very important from a theoretical point of view, they do not provide any information on how to construct the unknown functional, and some more considerations have to be taken in order to solve the electronic problem. The Kohn Sham (KS) assumption [89] states that for each system described by the Hamiltonian (2.45) an effective external potential v_{KS} exists such that the ground state density of a non-interacting system of particles is equal to the ground state density of the real interacting electron system. This is called the Kohn-Sham potential and it allows the electronic problem to be rewritten in the simplified single-particle form:

$$\left(-\frac{1}{2}\nabla^2 + v_{\mathrm{KS}}(\mathbf{r}) \right) \varphi_i(\mathbf{r}) = \epsilon_i \varphi_i(\mathbf{r}), \qquad i = 1, \cdots, N \tag{2.15}$$

The single-particle wavefunctions φ_i are called Kohn-Sham orbitals. The many-body wavefunction for this system is the Slater determinant of the KS orbitals, and the ground state density assumes the form (2.5).

The energy functional (2.14) for this system is written as

$$E_{\mathrm{KS}}[n] = T_{\mathrm{S}}[n] + E_{\mathrm{H}}[n] + \int d\mathbf{r}\; n(\mathbf{r}) v(\mathbf{r}) + E_{\mathrm{XC}}[n] \tag{2.16}$$

where T_{S} is the kinetic energy of the non-interacting system, E_{H} the Hartree potential and E_{XC} the exchange-correlation term defined as

$$E_{\mathrm{X}C}[n] = T[n] - T_{\mathrm{S}}[n] + U[n] - U_{\mathrm{H}}[n] \tag{2.17}$$

The minimisation of the functional (2.16) gives the form of the KS potential:

$$v_{\mathrm{KS}}(\mathbf{r}) = v(\mathbf{r}) + v_{\mathrm{H}}(\mathbf{r}) + \frac{\delta E_{\mathrm{X}C}[n]}{\delta n(\mathbf{r})} \tag{2.18}$$

This can then be inserted in the Kohn-Sham Equations (2.15).

At this point the theory is exact, apart from the analytic form of the exchange-correlation term which is unknown. Approximations for this term are required in order to practically solve the electronic problem. The Local Density Approximation (LDA) was the first method developed for this purpose [90; 91]. It calculates the XC energy per particle of a non-uniform gas as if it was locally equal to the XC energy of a uniform interacting system:

$$E_{\mathrm{XC}}^{\mathrm{LDA}}[n] = \int d\mathbf{r}\ \epsilon_{\mathrm{XC}}^{\mathrm{hom}}[n(\mathbf{r})]n(\mathbf{r}) \tag{2.19}$$

A more accurate approximation for the XC term is the Generalised Gradient Approximation (GGA). Within this method the XC energy does not depend on the density only, but also on its gradient (semi-local dependence).

In this work the parametrisation for GGA given by Perdew, Burke and Ernzerhof (PBE) [92] is used. More sophisticated calculations make use of meta-GGA or hybrid functionals [93], incorporate part of the exchange from Hartree–Fock theory with exchange and correlation from other sources. This hierarchy of approximations has been described by John Perdew as a "Jacob's ladder" towards chemical accuracy [94]. The superior accuracy of the higher "rungs" is complemented by the transparency of the lower ones.

Plane-Wave Basis Set

In solid state physics it is common to model periodic systems. Since the Hamiltonian has the same periodicity as the lattice, the Bloch theorem [95] applies and the wavefunction can be written as the product of a periodic function and a plane wave. The eigenstates of the Hamiltonian are

$$\varphi_{i\mathbf{k}}(\mathbf{r}) = \frac{1}{\sqrt{N_{\mathrm{cell}}}} \mathrm{e}^{i\mathbf{k}\cdot\mathbf{r}} u_{i\mathbf{k}}(\mathbf{r}) \tag{2.20}$$

where $\mathbf{k}$ is a vector in the BZ and $u_{i\mathbf{k}}(\mathbf{r})$ has the same periodicity as the direct lattice. This function can be expanded as a Fourier series:

$$u_{i\mathbf{k}}(\mathbf{r}) = \frac{1}{\Omega_{cell}} \sum_{m=-\infty}^{+\infty} C_{mi}(\mathbf{k}) \mathrm{e}^{i\mathbf{G}_m \cdot \mathbf{r}} \tag{2.21}$$

An infinite number of plane waves is in principle required to reproduce the exact wavefunction. The size of the basis set used is controlled by the largest wavevector in the expansion of (2.21). Given that the kinetic energy of an electron with wavevector $\mathbf{k}$ is $E_{\mathbf{k}} = \frac{1}{2}(\mathbf{k} + \mathbf{G})^2$, truncation is equivalent to imposing a cut-off on the kinetic energy.

The advantage of expanding the wavefunction in plane waves rather than using localised orbitals centred on atoms/bonds is that this set is unbiased: all space is treated in the same way. Furthermore it is complete from a mathematical viewpoint and there is only one convergence parameter, the kinetic energy cutoff. The main disadvantage is also related to periodicity: when systems with open boundary conditions are studied, it may be necessary to add large regions of vacuum in order to avoid fictitious self-interaction and, since all the space is treated in the same way, the cost of the calculation is greatly increased. The usage of real space projector methods speeds up the calculations in these cases [96].

The Pseudopotential Approximation

The nearly free electron-picture is good for describing valence electrons (in which we are mainly interested) but not for the electrons close to the atomic core. Atomic wavefunctions are eigenstates of the Hamiltonian, and therefore orthogonal by construction. Since core states are localised in proximity to nucleus, wavefunctions are bound to have rapid oscillations in order to maintain orthogonality. An accurate description therefore requires a large kinetic energy for the valence electrons in the core region, which roughly cancels

the large potential energy Coulombic interaction. It is thus convenient to replace the all-electron potential with a smoother, weaker pseudopotential in the region encircling the nucleus. The resulting pseudo wavefunctions have no nodes in that region, so that good accuracy can be obtained using a basis set with fewer plane waves.

Pseudopotentials [97] are normally constructed from all-electron calculations on isolated atoms. Valence wave functions are modified to remove oscillations close to the core, and the Schrödinger equation is inverted to find the potential. Pseudopotentials are not unique, and can be defined in different ways. It used to be common practice to require norm-conservation for the pseudopotential, i.e. to constrain the charge in the core region to be the same as for the full-electron calculation. Relaxing this conditions lead to a class of pseudopotential known as ultra-soft, capable of producing accurate results with even fewer plane waves for the wave function [97]. The cutoff for the calculation is reduced, but an augmentation part must be included within the core region. The closely related more recently developed Projector-augmented wave (PAW) method [98] reconstructs the all-electron wave functions from the pseudo wavefunction via a linear transformation (pseudo operator).

Brillouin Zone Integration

The calculation of many quantities such as total energy and charge density involves integrals over the first Brillouin zone. In practice, a grid of $\mathbf{k}$ points is employed. If the system is large enough in real space, the centre zone point Γ may be enough to obtain converged results. This brings also the extra advantage of speeding up the calculation, as real wavefunctions can be used. In a more general case, more points are required. The most common technique, proposed by Monkhorst and Pack in Reference [99], is a uniformly spaced grid of special points in the irreducible Brillouin zone, weighted with coefficient $w_{\mathbf{k}}$ in order to account for symmetries. This grid

does not necessarily include Γ. In some cases shifted grids are known to converge faster to accurate results, but including the centre zone point can be crucial for certain properties. While only few **k**-points are usually required for obtaining converged results in insulators and semiconductors, in metals the situation is different. This is because electronic bands cross the Fermi level, and therefore there is a sharp discontinuity in reciprocal space between occupied and unoccupied states. This leads also to charge sloshing within the self-consistent field (scf) calculation, which results in slow convergence. This is addressed by smoothing out the discontinuity at Fermi level, so that the scf can converge faster with respect to the number of **k**-points. This technique is called smearing, and several methodologies are available. The first and more physical one consist of introducing a fictitious electronic temperature, in such a way that the step function describing occupancies as a function of energy in the integral gets replaced by a Fermi-Dirac distribution. Other approaches rely on writing the step function as the integral of a delta function and approximating the latter with a Gaussian. This is referred to as Gaussian smearing. Techniques from the same family are Methfessel-Paxton (MP) [100] and Marzari-Vanderbilt [101] smearing techniques. Within the MP scheme, the Gaussian is multiplied by a series of Hermite polynomials. This enhances the smoothness of occupancies near the Fermi level and results in a faster convergence with respect to the sampling mesh. The only drawback is the introduction of unphysical negative occupancies, usually negligible for standard simulation settings. This problem is solved within the Marzari-Vanderbilt approach, by multiplying the Gaussian by a first order polynomial. This results in a less smooth convergence with respect to the previous method, and it is generally used in cases for which negative occupancies are not negligible. While smearing helps the convergence of the scf calculation, it modifies the electronic structure. Large values for the Gaussian broadening must therefore be avoided to make a compromise between accuracy of the electronic structure and smoothness of the scf convergence.

Mixing Parameters for Large Metallic Systems

The main goal of DFT is to solve the Kohn-Sham equations (2.15). An iterative self-consistent approach is used: an initial guess is made for the charge density of the system and KS orbitals are obtained. A new charge density is thus defined, and the process is iterated until the difference in energy between two consequent steps is below a certain threshold. A complete charge update at every iteration may lead to non-convergent behaviours, and it usually slows down calculations. A smooth mixing technique is therefore employed, and the charge density is updated only by a certain percentage. Iterative solving of the KS equations as implemented in the Vienna Ab Initio Simulation Package (VASP) aims at the minimisation of the residual vector $R[\rho_{in}]$, defined as the difference between the charge density and its value at the previous step. Linearisation of the residual vector around ρ_{sc} (linear response theory) leads to

$$R[\rho_{in}] = \rho_{out}[\rho_{in}] - \rho_{in} = J(\rho_{in} - \rho_{sc}) \tag{2.22}$$

The charge dielectric function J is defined as

$$J = 1 - \chi U(q) \quad , \quad U(q) = (4\pi)/q^2 \tag{2.23}$$

where q is the modulus of a vector spanning the reciprocal space, $U(q)$ the Fourier transform of the Coulomb potential and χ the susceptibility. A broad spectrum of J slows convergence. For insulator and semiconductors its width is not size dependant, while for metals it is proportional to the square of the longest dimension of the cell (metallic screening). This causes slow convergence (charge sloshing). A model dielectric function of the type

$$J^{-1} \approx \max\left(\frac{q^2 \mathrm{AMIX}}{q^2 + \mathrm{BMIX}}, \mathrm{AMIN}\right) \tag{2.24}$$

is used, where AMIX, AMIN, BMIX are parameters supplied by the user.

A strategy to optimise these parameters is to look at the average of the eigenvalues of the dielectric function at the end of the calculation; if it is larger than one, BMIX must be decreased. It is also common practice to use a linear mixing approach (BMIX = 0). In this case, if we look at the average of the eigenvalues of a converged calculation, we can improve our estimate for AMIX by multiplying the present one with the obtained value. This will not always work for large metallic systems since the average of the eigenvalues will be larger than one in most of the cases and increasing AMIX too much will lead to charge sloshing. If the system is magnetic the problem is even more pronounced: two more parameters AMIX_MAG and BMIX_MAG are required. An initial guess for the magnetic moments of atoms must be provided to break the symmetry. Its value should be larger than the expected one since initial charge density updates can push it towards a low magnetisation local minimum for the electronic structure.

Postprocessing DFT Data

Once the Kohn-Sham equations are solved, the total energy of the system and the charge density (on a real-space grid) are immediate outputs of the calculation. Other quantities can be evaluated e.g. for comparison with experimental data. The density of states (DoS), for instance, is defined as:

$$g(\epsilon) = \sum_n \langle\psi_n|\psi_n\rangle \delta(\epsilon - \epsilon_n) \tag{2.25}$$

where ϵ_n is the eigenvalue relative to the eigenvector $|\psi_n\rangle$. Projection onto a complete orthonormal basis $\{|j\rangle\}$ leads to:

$$g(\epsilon) = \sum_j g_j(\epsilon) \ , \ g_j(\epsilon) = \sum_n \langle\psi_n|j\rangle\langle j|\psi_n\rangle \delta(\epsilon - \epsilon_n) \tag{2.26}$$

A suitable complete basis set is inserted, capable of describing some physical feature of the system. Projection on the real space grid gives the local

density of states (LDoS) $g(\epsilon, \mathbf{r})$, which gives information about the spatial distribution of the DoS. This quantity can be integrated in energy near the Fermi level in order to predict STM images. Another common complete basis set are the Hydrogen wavefunctions Φ_{nlm} centred at the atomic sites. This procedure allow a better understanding of the chemical bonding between atoms. This quantity is called the projected density of states (PDoS). As a side product of this calculation, atom resolved charges can be defined from the coefficients $\langle\psi_i|\Phi_{nlm}\rangle$. This is known as the Löwdin population analysis. A similar method for obtaining atomic resolved charge densities is the Mulliken analysis [102], based on a projection in real space of the Kohn-Sham orbitals. It is known to be less accurate then the Löwdin method because of the overlap between orbitals, and it is sensitive to the basis set used for the DFT calculation. These methods are wavefunction-based, and they are not expected to be robust since the Kohn-Sham orbitals are not the physical wavefunction of the system. The physical product of a DFT calculation is the electron density, and methods relying on it are much more accurate. For instance the Bader analysis algorithm defines volumes in real space by searching for zero flux surfaces in the charge density. The integral of the charge density within a Bader volume is a good approximation for the atomic resolved charges, and overlap between atoms is avoided [75].

2.3 The Classical Approach

Interatomic Potentials

An interatomic potential (IP) is a function of atomic coordinates, used to model the potential energy of an atomistic system. The dependence on a number of parameters, fitted to *ab initio* or experimental data, allows the reproduction of basic properties of the system such as bond lengths and bond angles, and the calculations of thermodynamic average properties. They allow the simulation of large sized systems, typically not accessible to *ab initio* methods. The functional form of the potential $V(\mathbf{r})$ is usually the sum of single atom energetic contributions. Each contribution is the sum of terms arising from two, three and in general many body interactions with a group of neighbours. These interactions have a local character, and it is common practice to define a cutoff radius after which the interactions are truncated. The two body term is usually a function of the bond length $r_{ij} \equiv |\mathbf{r}_i - \mathbf{r}_j|$. The three-body term is instead a function of the angle between the bonds:

$$\theta_{ijk} = \frac{\mathbf{r}_{ij} \cdot \mathbf{r}_{jk}}{r_{ij} r_{jk}} \tag{2.27}$$

This angular contribution is usually not relevant for metals because metallic bonding between atoms is not directional.

One of the simplest form for a two-body potential was proposed by Lennard-Jones [103]. It is the sum of a short-range repulsive term and an attractive one:

$$V_{ij} = -4\epsilon \left[\frac{C_n}{r_{ij}^n} - \frac{C_{2n}}{r_{ij}^{2n}} \right] \tag{2.28}$$

where ϵ is the distance from the minimum and C_n, C_{2n} parameters for the interaction. A popular version of this potential chooses $n = 6$, so that the dispersion term matches the long-range behaviour of van der Waals forces.

Embedded Atom Method (EAM)

The Embedded Atom Method (EAM) provides a computationally efficient simulation tool capable of describing general properties of metallic systems, especially for close-packed structures such as fcc crystals. This model, originally introduced by Daw and Baskes [4], is based on the addition of an electronic embedding energy term to the pair interaction contribution. The embedding term is defined as a function of a linear superposition of spherically averaged electron density contributions, an ansatz which is satisfied in a large number of cases and produces results comparable with more sophisticated approaches [104]. Within this approach, the evaluation of energy and forces is several orders of magnitude faster than comparable first-principles calculations and the computational cost scales linearly with the number of atoms (as opposite of the cubic scaling of DFT). EAM calculations are therefore able to span length and time scales not accessible to QM methods.

Within the EAM approach, the total energy of a system is defined as:

$$E_{\mathrm{tot}} = \frac{1}{2}\sum_{ij=1}^{N}\phi(r_{ij}) + \sum_{i=1}^{N}\mathcal{F}(\bar{\rho}_i) \tag{2.29}$$

where N is the number of atoms, $\phi(r_{ij})$ the pair interaction between two atoms, i and j, separated by a distance r_{ij}. $\mathcal{F}$ is the embedding energy of the i-th atoms and $\bar{\rho}_i$ the host electron density induced on it by all the surrounding atoms:

$$\bar{\rho}_i = \sum_{j\neq i}\rho(r_{ij}) \tag{2.30}$$

for atomic densities $\rho(r)$ postulated to be a linear combination of exponential functions of the interatomic distances. The so-obtained electron charge density is often in agreement with DFT results, as shown in Reference [104] for a Cu system.

The interatomic interactions are truncated for distances larger then a certain cutoff radius r_c. Different cutoff radii can be used for the pair interaction and electron density. Within the latter radius, EAM is a many-body potential. No angular contribution to the energy is included, as the metallic bond is usually not directional.

The modified embedded atoms model (MEAM) [105] takes into account angular interactions using a three-body term. As this is usually negligible in bulk metals, a sophisticated implementation (better choice of embedding function, larger number of fitting parameters) of EAM is usually more robust than a MEAM potential. Parameters for EAM potentials can be fitted only for a limited number of concurrently interacting atomic species. While atomic densities and embedding functions can be fitted separately for each atomic species, pair interactions contain the cross functions ϕ_{XY}. Parameters for this term can be fitted in order to reproduce e.g. equilibrium distances between atoms of different atomic species in a certain phase. A number of extra parameters can be obtained by applying transformations that would leave unaltered mono-species contributions, as shown in Equations (2.41). This is still not enough to guarantee flexibility in fitting parameters, and hence good transferability for the potential. Binary EAM potentials are known to be accurate and therefore capable of reproducing experimental results (e.g. Reference [6]). Recently, ternary EAM potentials have been produced to model more complex Ni-based alloys [106]. While they add a further layer of complexity to the EAM scheme, thus allowing the simulation of more realistic systems, there is still not general consensus on their reliability.

The EAM implementation for Ni-Al systems developed by Y. Mishin (cf. References [5; 107; 108]) is one of the most reliable EAM model for dislocation (cf. Section 4.2) modelling at the atomic scale. The potential developed in Reference [5] is fitted to properties of γ and γ', and accurately reproduces the generalised stacking fault energy curve, as shown in Section 3.6, crucial for describing the core structure Shockley Partial dislocations.

The other versions of this potential [107; 108] are fitted instead to the lattice parameter for the $B2$ NiAl phase, causing underestimation for the lattice parameter of γ'. This constitutes an example of the transferability issue for interatomic potentials. The Mishin 2004 potential is used here, following the choice of several other authors [6; 28; 109].

Electronic densities $\rho(r)$ for this potential are postulated to be of the form:

$$\rho(r) = \psi\left(\frac{r - r_c}{h}\right)\left[A_0 z^y \mathrm{e}^{-\gamma z}\left(1 + B_0 \mathrm{e}^{-\gamma z}\right) + C_0\right] \tag{2.31}$$

where $z = |r - r_0|$ is the distance between atoms and $\psi(x)$ is a cut-off function, depending on the cut-off radius r_c and on an additional smoothing parameter h. This function is defined as:

$$\psi(x) = \begin{cases} \frac{x^4}{1+x^4} & x < 0 \\ 0 & x \geq 0 \end{cases} \tag{2.32}$$

The interactions between atoms are therefore taken to be zero if the distance between them is greater than a the cut-off radius r_c. Equation (2.31) parametrises $\rho(r)$ with 8 parameters A_0, B_0, C_0, r_0, r_c, h, y and γ. One of them can be eliminated by normalising the electron density in the equilibrium FCC lattice. The pair interaction function is parametrised in a generalised Lennard-Jones form:

$$\phi(r) = \psi\left(\frac{r - r_c}{h}\right)\left[\frac{V_0}{b_1 - b_2}\left(\frac{b_2}{z^{b_1}} - \frac{b_1}{z^{b_2}}\right) + \delta\right] \tag{2.33}$$

where $z = r/r_1$ and b_1, b_2, r_1, V_0, δ are fitting parameters. The functions $\rho(r)$, $\phi(r)$ and their derivatives up to the second order go to zero smoothly at the cut-off distance because of the function form of $\psi(r)$. This is important to avoid discontinuity for the forces calculated using the potential.

The embedding energy is obtained by inverting the universal equation of state of an FCC crystal

$$E(\alpha) = E_0 \left[1 + \alpha x + \beta \alpha^3 x^3 \frac{2x+3}{(x+1)^2} \right] \mathrm{e}^{-\alpha x} \tag{2.34}$$

where $x = a/a_0 - 1$ and

$$\alpha = \left(-\frac{9\Omega_0 B}{E_0} \right)^{1/2} \tag{2.35}$$

In these equations E is the crystal energy per atom relative to a set of isolated atoms, E_0 the cohesive energy (minimum of E), a the lattice parameter, a_0 its equilibrium value, $\Omega_0 = a_0/4$ the equilibrium volume, B the bulk modulus and β an adjustable parameter. This procedure guarantees an exact fit to to the equilibrium bulk properties. The cubic term in Equation (2.35) allows the crystal energy to be varied under strong compressions.

The functions described in this Section depend on the chemical species, seven functions (3 pair interactions, 2 charge densities and 2 embedding functions) are therefore required to describe a binary system. All the functions apart from the cross-interaction function $\phi_{NiAl}(r)$ can be obtained by fitting the properties of individual elements and only the latter is fitted to properties of binary alloys. Extra fitting parameters are obtained by applying operations that keep the total energy of a single element invariant but change the energy of a binary system. Such transformations include:

$$\rho_B(r) \longmapsto s_B \rho_B(r) \tag{2.36}$$

$$\mathcal{F}_B(\bar{\rho}) \longmapsto \mathcal{F}_B(\bar{\rho}/s_B) \tag{2.37}$$

$$\mathcal{F}_A(\bar{\rho}) \longmapsto \mathcal{F}_A(\bar{\rho}) + g_A \bar{\rho} \tag{2.38}$$

$$\mathcal{F}_B(\bar{\rho}) \longmapsto \mathcal{F}_B(\bar{\rho}) + g_B \bar{\rho} \tag{2.39}$$

$$\phi_{AA}(r) \longmapsto \phi_{AA}(r) - 2g_A \rho_A(r) \tag{2.40}$$

$$\phi_{BB}(r) \longmapsto \phi_{BB}(r) - 2g_B \rho_B(r) \tag{2.41}$$

The transformation coefficients s_B, g_A g_B may be used as extra parameters when fitting the cross-interaction function. The binary system is overall described by the total of 36 parameters, including elastic constants, formation and migration energies of vacancies from experimental data and volume-energy relations for several structures from DFT calculations.

In Figure 2.1 the pair interactions terms are plotted (a,b), together with the electron density (c) and the embedding energies (d). The host electron density, x axis in panel (d), is the sum over the neighbours of the electron densities of panel (c), as from Equation (2.30). In all the pair interactions the global minimum corresponds to the distance between nearest neighbours in a fcc crystal, 2.49 Å, 2.52 Å and 2.86 Å for Ni, Ni_3Al and Al respectively.

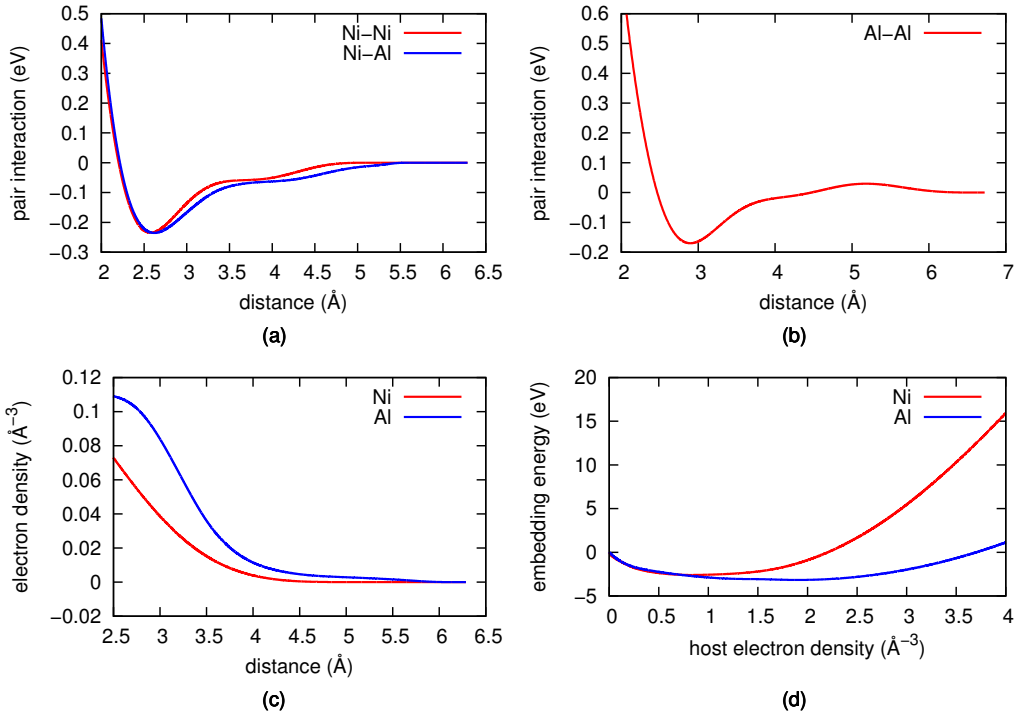

Figure 2.1: Pair interaction functions (a,b), electronic density (a) and embedding energy terms (d) as parametrised by Y. Mishin.

2.4 Molecular Dynamics

Molecular dynamics (MD) is a tool to simulate the time evolution of a set of atoms using the Newtonian equations of motion. Atoms are modelled as rigid balls localised in well determined positions, updated accordingly to the forces calculated with either an IP or a QM method. In the first case, the force is obtained as the gradient of the functional form of the potential, in the latter using the Hellmann-Feynman theorem (2.10). For simplicity, the simpler case of an IP is considered in the following brief review. See References [110; 111] for a more detailed description of the method.

Equations of Motion

Let us consider an isolated system of N atoms with masses $\{m_j\}$ interacting through a potential $V(\mathbf{r})$. The total energy of the system is a conserved quantity, and can be written as the sum of a kinetic and a potential term using the Hamiltonian:

$$H = T\{\mathbf{p}\} + V\{\mathbf{r}\} \tag{2.42}$$

where $\mathbf{r} = (\mathbf{r}_1, \mathbf{r}_2, \cdots, \mathbf{r}_N)$ and $\mathbf{p} = (\mathbf{p}_1, \mathbf{p}_2, \cdots, \mathbf{p}_N)$ are the positions and the momenta of the atoms. The kinetic term is given by

$$T = \sum_{i=1}^{N} \frac{\mathbf{p}_i^2}{2m_i} \tag{2.43}$$

whilst the potential one can have different functional forms, as discussed in Section 2.3. The time evolution is given by Newton's 3$^{\text{rd}}$ law

$$\mathbf{F}_i = m_i \ddot{\mathbf{r}}_i \tag{2.44}$$

where $\mathbf{F}_i = -\nabla_i V(\mathbf{r})$ is the force acting on the i-th atom and dots indicate derivatives with respect to time.

It is useful to recast Equation (2.44) into the equivalent form:

$$\begin{cases} \dot{\mathbf{x}}_i = & \frac{\mathbf{p}_i}{m} \\ \dot{\mathbf{p}}_i = & \mathbf{F}_i \end{cases} \tag{2.45}$$

The simplest algorithm to perform a MD simulation is based on approximating the derivatives in Equation (2.45) with difference quotients (equivalent to a first order Taylor expansion). The resulting equations of motion are of the form:

$$\begin{cases} \mathbf{r}(t+\Delta t) = & \mathbf{r}(t) + \frac{\mathbf{p}}{m}\Delta t \\ \mathbf{p}(t+\Delta t) = & \mathbf{p}(t) + \mathbf{F}\Delta t \end{cases} \tag{2.46}$$

This is referred to as the Euler method, and it is rarely used in practical MD simulations due to its limited accuracy. The truncation error is $\mathcal{O}(\Delta t)^2$, and the total error may grow with physical time (drift).

A much better molecular dynamics integrator is the Verlet scheme [112]. The equations of motion are obtaining by expanding the quantities $\mathbf{r}(t+\Delta t)$ and $\mathbf{r}(t-\Delta t)$ as third order Taylor series. By summation of the resulting expressions, odd terms elide and we are left with the simple equation:

$$\mathbf{r}(t+\Delta t) = 2\mathbf{r}(t) - 2\mathbf{r}(t-\Delta t) + F(\Delta t)^2 + \mathcal{O}(\Delta t)^2 \tag{2.47}$$

This is a position only scheme which requires the positions at time $t-\Delta t$ to be store in memory. Since the error is fourth order in Δt, this scheme is very accurate. It has also time-reversal symmetry, which makes it very stable also for relatively large time steps. The main disadvantage is that momenta are not integrated, as this may lead to numerical instability for the total energy of the system and prevents the definition of volumes in phase space.

A way of introducing back momenta within the integration scheme is the leap frog scheme. Half time-step momenta are defined as:

$$\mathbf{p}(t + \Delta t/2) = m\frac{\mathbf{r}(t + \Delta t) - \mathbf{r}(t)}{\Delta t} \tag{2.48}$$

The integrator for the positions assumes the form:

$$\mathbf{r}(t + \Delta t) = \mathbf{r}(t) + \frac{\mathbf{p}}{m}(t + \Delta t/2)\Delta t \tag{2.49}$$

This algorithm is as robust as the original Verlet algorithm. Despite momenta being present, conservation of total energy can still not be checked because positions and momenta are defined at different times. This final obstacle is overcome within the so-called velocity Verlet scheme, by defining:

$$\mathbf{p}(t) = \frac{1}{2}\big(\mathbf{p}(t + \Delta t/2) + \mathbf{p}(t - \Delta t/2)\big) \tag{2.50}$$

Within this algorithm, momenta are correct to $\mathcal{O}(\Delta t^2)$ and positions to $\mathcal{O}(\Delta t^3)$. This algorithm ensures the conservation of volumes in the phase space and of total energy during the dynamics for reasonable values of the time step of the simulation. The final form for the integrator of the equations of motion is:

$$\begin{cases} \mathbf{r}(t + \Delta t) = & \mathbf{r}(t) + \frac{\mathbf{p}(t)}{m}\Delta t + \frac{\mathbf{F}(t)}{2m}(\Delta t)^2 \\ \mathbf{p}(t + \Delta t) = & \mathbf{p}(t) + \frac{\mathbf{F}(t+\Delta t)+\mathbf{F}(t)}{2}\Delta t \end{cases} \tag{2.51}$$

The dependance of the updated momenta on $\mathbf{F}(t + \Delta t)$ is not a problem, as forces are functions of the atomic positions only. The requirement to store forces at different steps can be avoided by reintroducing the half time-steps as in Equation (2.48).

Thermostats

Standard MD making use of the Verlet algorithm preserves the total energy of the system, thus generating a microcanonical NVE ensemble. It is sometimes better to perform simulations within other ensembles for e.g. a better match with experimental conditions. It is particularly useful to generate the canonical ensemble NVT, where the simulation temperature is preserved. For many simulation setups with several thousands atoms the two ensemble are equivalent as the system acts as its own thermal bath, but for smaller structures or, in general, for systems that requires some more control during the simulation, thermostats are a useful tool for adding/removing heat.

Velocity rescaling is the most straightforward method for controlling temperature during a Molecular Dynamics simulation. Let us consider the equipartition theorem:

$$\left\langle \frac{m v_{I,\alpha}^2}{2} \right\rangle = \frac{1}{2} k_{\mathrm{B}} T \tag{2.52}$$

where $v_{I,\alpha}$ is the α component of the velocity of the I^{th} atom and $\langle \cdots \rangle$ indicates an ensemble average. The instantaneous temperature is defined as:

$$T(t) = \frac{1}{N_f k_{\mathrm{B}}} \sum_{I=1}^{N} m_I v_I^2 \tag{2.53}$$

where N_f is the number of degrees of freedom.

The simplest way of setting the simulation temperature is to rescale the velocity according to

$$v'_{I,\alpha} = v_{I,\alpha} \left(\frac{T}{T(t)} \right)^{1/2} \tag{2.54}$$

This technique has two main drawbacks. The discontinuity of velocities can have major effects on the trajectory. The kinetic energy will remain constant over time, with no fluctuations.

The canonical ensemble is therefore not reproduced, as kinetic energy fluctuations are predicted to be of the form:

$$\sigma_k^2 = \frac{3N}{2} N_f (k_b T)^2 \tag{2.55}$$

where N_f is the number of degrees of freedom of the system.

Within the Berendsen approach [113] a time scale for rescaling velocities is assigned, instead of modifying them at every simulation step. This mimic the action of a thermal baths weakly coupled to the system. Atomic velocities have continuous profiles, but the correct canonical fluctuations are still not captured. Another simple example for a thermostat is the one proposed by Andersen [114], based on the reassignment of the velocity of a random atom. This method can be shown to sample the canonical ensemble correctly. On the other hand, velocity reassignment leads to unreliable calculation of diffusion coefficients.

Within the Langevin approach [115], atoms are considered effectively immersed in a viscous fluid of smaller particles. This affects the atomic forces in two ways: a viscous drag Γ proportional to the velocity and a stochastic noise $\mathbf{A}(t)$ term due to collision with the smaller particles. The total force acting on the atom i is written as:

$$m_i \ddot{\mathbf{r}}_i = -\nabla_i U(\mathbf{r}) - m\Gamma \dot{\mathbf{r}}_i + \mathbf{A}_i(t) \tag{2.56}$$

This thermostat can be shown to be canonical and ergodic (the time spent by the system in a region of the phase space is proportional to its volume, so that time averages can be substituted with average on the phase space). Since all particles are coupled to the local bath, this thermostat removes heat localisation problems present e.g. in the Andersen model. The main drawbacks are due to random collisions with the small fictitious particles, as momentum transfer is destroyed.

The Nosé–Hoover thermostat

A rigorous formulation of a thermostat capable of simulating the canonical ensemble has been advised by Nose [82]. The approach consists of a modified Lagrangian method, in which an additional degree of freedom s and its conjugated momentum p_s are introduced. An effective mass Q is also defined, with the time evolution for this degree of freedom given by $= \dot{s} = p_s/Q$. The modified Lagrangian is then postulated to be of the form:

$$\mathcal{L} = \sum_{i=1}^{N} \frac{m_i s^2 \mathbf{v}_i^2}{2} - V(\mathbf{r}) + \frac{Q\dot{s}^2}{2} - \frac{C}{\beta} \ln s \tag{2.57}$$

where C is a constant and $\beta = (k_B T)^{-1}$. The conjugate momenta for this Lagrangian have the form $\mathbf{p}_i = m_i s^2 \mathbf{r}_i$. The microcanonical partition function $\Omega(E, V, N)$ is evaluated as

$$\Omega(E, V, N) = \frac{1}{N!} \int d\mathbf{r} d\mathbf{p} ds dp_s \; \delta(H - E) \tag{2.58}$$

By substituting $\mathbf{p}' = \mathbf{p}/s$ and using basic properties of the delta function, integration is performed for the (s, p_s) variables. The following relation is so obtained:

$$\Omega(E, V, N) \propto \frac{1}{N!} \int d\mathbf{r} d\mathbf{p} \; \mathrm{e}^{-\beta[K(\mathbf{p}) + U(\mathbf{r})]} = Z(T, V, N) \tag{2.59}$$

where $K(\mathbf{p})$ and $U(\mathbf{r})$ are the kinetic and the potential contribution to the system Hamiltonian respectively, and $Z(T, V, N)$ is the canonical partition function. The exponential in (2.59) comes from the specific choice of a logarithmic dependence on s in the Lagrangian (2.57). This result implies that a microcanonical simulation for the extended system generates a canonical ensemble for the original one. The mass Q is a parameter of the simulation and must be specified. It determines the exchange rate of energy between the atomistic system and the thermal bath.

The approach as described above is correct from a formal point of view, but not convenient to use for practical purposes as the momenta are rescaled by s, which is not constant. This implies that also the simulation time step is variable during dynamics. This problem is alleviated in Hoover's approach [83], in which the conjugate moment p_s is replaced with a friction term ξ, which can be shown be a constant using the the equipartition theorem. The modified equations of motion are usually integrated using the velocity Verlet algorithm. Even though this method rigorously generates the canonical ensemble, it is known to have problems related to ergodicity. A technique used to enhance temperature equilibration is based on Nose Hoover chains [116], in which multiple heat baths (s variables) are employed. Another recently developed technique is based on the coupling to a stochastic heat bath, in the Nosé-Hoover-Langevin approach [117].

Barostats

Another important ensemble is the isotherms-isobaric NPT, which is generated by adding a barostat to the existing thermostat in order to control both simulation parameters. The conserved quantity is the Gibbs free energy $G = H - TS$, where S is the entropy and H the enthalpy of the system. Simulations making use of a barostat but not a thermostat are within the NPH ensemble.

The Berendsen model [113] is based on rescaling all the length in the simulation box (lattice and atomic positions) in order to set a certain pressure. The rescaling factor is

$$\mu = \left[1 - \frac{\beta \Delta t}{\tau_p}(P_0 - P(t))\right]^{1/3} \tag{2.60}$$

where P_0 is the desired pressure, β the isothermal compressibility of the system, Δt the time-step for integrating the equations of motion and τ_p the coupling time constant. The instantaneous pressure $P(t)$ is evaluated as the

average of the diagonal components of the virial stress tensor:

$$\sigma_{ij} = \frac{1}{2V} \sum_{n,m=1}^{N} \left[x_i^{(n)} - x_i^{(m)} \right] f_j^{(nm)} \tag{2.61}$$

where $x_i^{(n)}$ the coordinate i of the atom n and $f_i^{(nm)}$ the force exerted by atom n on atom m along the direction i. The Andersen model [114] is instead based on an extended Hamiltonian for controlling pressure, written as

$$H = H_0 + E_{\text{kin}} + E_{\text{pot}} \tag{2.62}$$

where H_0 is the Hamiltonian for the atoms and the kinetic and potential energies for the piston are

$$E_{\text{kin}} = \frac{Q}{2}\dot{V}^2 \ , \ E_{\text{pot}} = PV \tag{2.63}$$

where Q is the mass of the piston. Positions and velocities are rewritten in reduced units as $\mathbf{s} = \mathbf{r}V^{-1/3}$ and $\dot{\mathbf{s}} = \mathbf{v}V^{-1/3}$. The equations of motion read:

$$\ddot{\mathbf{s}} = \frac{\mathbf{f}}{m}V^{-1/3} - \frac{2}{3}\frac{\dot{V}}{V}\dot{\mathbf{s}} \ , \ \ddot{V} = \frac{1}{Q}(P(t) - P_0) \tag{2.64}$$

where $\mathbf{f}$ are the forces acting on the atoms. A generalisation of this approach, known as the Parrinello-Rahman barostat, has been proposed in Reference [118]. The degrees of freedom of the cell have been introduced in an extended Lagrangian, in a similar fashion to the Nose-Hoover thermostat. This procedure, coupled with the aforementioned thermostat, generates the NPT ensemble. Another advantage with respect to the Andersen method is that the scheme is not limited to cubic cells, and it gives also control over the off-diagonal component of the stress tensor (shear). Its disadvantages include large fluctuations for small simulations cell, and the dependence on the effective mass of the piston, which can influence the dynamics.

2.5 Geometry Optimisation

An optimised structure is defined as a system for which the positions of the atoms minimise the potential energy to which the system is subjected. A typical potential energy surface presents several minima. The one corresponding to the lowest goal energy is the global minimum of the system, the others are called local minima. All these configurations can be degenerate. The optimised configuration is usually obtained (assuming a certain regularity in the potential energy landscape), in an iterative fashion. Many methods have been developed over time to solve this problem, improving the accuracy and the convergence of the algorithm. They can be divided in two categories: direct minimisation and damped molecular dynamics methods. Within the first method, the total energy function is minimised directly, within the second the equation of motions are solved so that the system will reach its minimum energy configuration. It is common to add a damping term to the forces to accelerate this process. The global minimum is not always reached by geometry optimisation, as the dependence on the initial conditions is significant.

Direct Minimisation

The steepest descent method is the simplest geometry optimisation algorithm. The gradient of the potential $V(\mathbf{R})$ is evaluated, and the atomic positions vector $\mathbf{R}$ is updated along its direction:

$$\mathbf{R}_{n+1} = \mathbf{R}_n - \gamma_n \nabla V(\mathbf{R}) \tag{2.65}$$

where n is the iterative index of the algorithm. The step size γ_n is in general different at every iterations. It can be obtained minimising the function $h(\gamma) = V(\mathbf{R}_n + \gamma_n \mathbf{p}_n)$ where $\mathbf{p}_n$ is the descent direction at iteration n. This procedure is called the line search algorithm, and can be performed by exact

minimisation of the function $h(\gamma)$, i.e. by solving $h'(\gamma) = 0$ as implemented within the conjugate gradient method, or loosely, by simply requiring a decrease of $h(\gamma)$. This is called the inexact line search. A robust implementation of this method is based on the Wolfe conditions [119] for the step length γ:

$$\begin{aligned} V(\mathbf{R} + \gamma\mathbf{p}) &\leq V(\mathbf{R}) + c_1\gamma\mathbf{p} \cdot \nabla V(\mathbf{R}) \\ \mathbf{p} \cdot \nabla V(\mathbf{R} + \gamma\mathbf{p}) &\geq c_2\mathbf{p} \cdot \nabla V(\mathbf{R}) \end{aligned} \tag{2.66}$$

with $0 < c_1 < c_2 < 1$. The first inequality is also known as the Armijo rule [120] and ensures a sufficient decrease of the function $V(\mathbf{R})$. The second rule, known as the curvature condition, ensures that the slope of the curve is also sufficiently decreased.

The conjugate gradient method is a generalisation of the former algorithm, in which increments are augmented in such a way that they keep track of the incremental direction from the previous iterations. The potential $V(\mathbf{R})$ is expanded as a second order Taylor series around a point $\mathbf{R}_0$:

$$V(\mathbf{R}) \approx V_0 + \mathbf{b} \cdot R + \frac{1}{2}\mathbf{R} \cdot A\mathbf{R} \tag{2.67}$$

where $V_0 = V(\mathbf{R}_0)$, $\mathbf{b} = -\nabla V(\mathbf{R}_0)$ and $A = HV(\mathbf{R}_0)$ where H is the Hessian matrix

$$H_{ij} = \frac{\partial^2}{\partial R_i \partial R_j}. \tag{2.68}$$

Suppose the first iteration produced a displacement $\mathbf{u}$, perpendicular to the gradient $\nabla V(\mathbf{R})$. The correspondent update of the latter is $\delta(\nabla V) = A\mathbf{u}$. The next iteration produces a displacement $\mathbf{v}$, orthogonal to the incremented gradient, and therefore orthogonal to $\mathbf{u}$ with respect to the scalar product:

$$\langle \mathbf{u}, \mathbf{v} \rangle_A = \mathbf{u} \cdot A\mathbf{v}. \tag{2.69}$$

The main advantage of this method is rapid convergence, usually not achieved with the gradient descent algorithm when the potential valley is flat.

The Newton method is also based on a second order Taylor expansion. An increment $\mathbf{u}$ is consider, such that it minimises the potential energy

$$0 = \nabla_{\mathbf{u}} V(\mathbf{R} + \mathbf{u}) = \nabla V(\mathbf{R}) + H\mathbf{u} \tag{2.70}$$

The iteration of the scheme is implemented according to the formula

$$\mathbf{R}_{n+1} = \mathbf{R}_n - \gamma[\mathbf{H}V(\mathbf{R}_n)]^{-1}\nabla V(\mathbf{x}_n) \tag{2.71}$$

where γ satisfies the Wolfe conditions (2.66). Calculation of the inverse of the Hessian matrix can be computationally expensive for a large number of degrees of freedom. Schemes using an approximation for it are called quasi-Newton methods. A popular scheme belonging to this class is the BFGS method, based on the iterative update:

$$H_{n+1} = H_n - \frac{H_n\mathbf{s}_n \otimes H_n\mathbf{s}_n}{\mathbf{s}_n \cdot H_n\mathbf{s}_n} + \frac{\mathbf{y}_n \otimes \mathbf{y}_n}{\mathbf{y}_n \cdot \mathbf{s}_n} \tag{2.72}$$

where H_n is the approximation for the Hessian matrix at the n^{th} iteration. The vectors $\mathbf{s}_k$ and $\mathbf{y}_k$ denotes the difference in the variables $\mathbf{R}$ and $\nabla V(\mathbf{R})$ at subsequent iterations. H_0 is usually set to the identity matrix, so that the at the first step Equation (2.71) simplifies to a steepest descent scheme.

Damped Molecular Dynamics

Another possibility for optimising atomic structures is to simulate the dynamics of the system, including a damping term to make it descent towards the minimum. The total force on the i-th particle is thus:

$$\mathbf{F}_i = -\nabla_i V - \mu\mathbf{v}_i \tag{2.73}$$

where μ is a constant and $\mathbf{v}_i$ the velocity of the i-th particle. Various techniques have been proposed to speed up the convergence.

The quick-min algorithm is based on modifying the velocities according to:

$$\mathbf{v}_i^{\text{new}} = \begin{cases} \alpha\mathbf{F}_i + \frac{(\mathbf{v}_i \cdot \mathbf{F}_i)\mathbf{F}_i}{|\mathbf{F}_i|}, & \text{if } \mathbf{v}_i \cdot \mathbf{F}_i > 0 \\ \alpha\mathbf{F}_i, & \text{otherwise} \end{cases} \tag{2.74}$$

where α is a constant. Velocities are therefore parallel to the forces, and the equilibration of the system is faster. The Fast Inertia Relaxation Engine (FIRE) [121] is a more efficient algorithm based on the same idea. Velocities are modified according to Equation:

$$\mathbf{v}_i^{\text{new}} = \begin{cases} (1-\alpha)\mathbf{v}_i + \alpha\frac{|\mathbf{v}_i|}{|\mathbf{F}_i|}\mathbf{F}_i, & \text{if } \mathbf{v}_i \cdot \mathbf{F}_i > 0 \\ 0, & \text{otherwise} \end{cases} \tag{2.75}$$

and an adaptive time step for integrating Newtonian equation is employed: if the velocity is parallel to the force, the time step is increased to allow the system to move faster towards the minimum, otherwise the time step is reduced to search more accurately for the steepest energy slope.

2.6 Transitions State Search

A common problem while dealing with atomistic simulation is to identify the rearrangement path of group of atoms from one local configuration to another. The calculation of the energy barriers between these minima may help explaining experimental data, or provide input to mesoscale method such as Kinetic Monte Carlo. Intermediate states are unstable by definition, and a fictitious interaction is usually added to their Hamiltonian to solve a minimisation problem and find the Minimum Energy Path (MEP). Within these chain-of-states methods, this term is the elastic interaction between one atom and its own images in the other system replica. The most popular technique from this family is the Nudged Elastic Band (NEB) method.

Within this method the minimisation of an elastic band is carried out where the perpendicular component of the spring force and the parallel component of the true force are projected out. The force on the i-th image is:

$$\mathbf{F}_i = -\nabla V(\mathbf{r}_i)\big|_\perp + (\mathbf{F}_i^{\text{spring}} \cdot \tau_i)\tau_i \tag{2.76}$$

where $\tau_i =$ is the unit vector tangent to the path and

$$\nabla V(\mathbf{r}_i)\big|_\perp \equiv \nabla V(\mathbf{r}_i) - \big(\nabla V(\mathbf{r}_i) \cdot \tau_i\big)\tau_i \tag{2.77}$$

the perpendicular component of the true force. The spring force does not interfere with structure optimisation in the coordinates perpendicular to the path, and the relaxed configurations lie on the MEP. The climbing image method allows for a better estimate of energy barriers. The elastic force is inverted for the least stable configuration, allowing the image to increase its total energy, thus reaching the saddle point. In Figure 2.2 the MEP for the diffusion of a Ni vacancy in the γ phase is shown as an example .

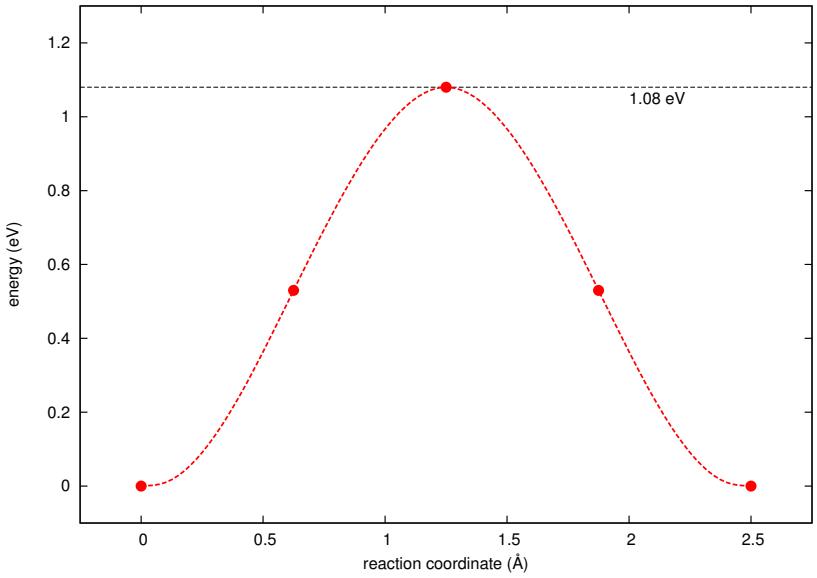

Figure 2.2: Diffusion barrier for a Ni vacancy in the γ phase.

2.7 The Multiscale Approach

Hierarchical Approach

Methods based on Quantum Mechanics are successful in describing the properties of materials. The typical size of simulated systems has been increasing over the years due to the improvements in speed and capacity of available computers, so that it is common nowadays to perform *ab initio* simulation for systems of interest for biology, such as large molecules, or for material science. Some quantities can still not be accessed through first-principle investigation due to system size and/or timescale of the process being orders of magnitude beyond what DFT can afford to simulate. Recently , it has become common to produce models that can be calibrated from *ab initio* data. One simple example is the EAM potential used in this work, which has been fitted to a number of parameters from DFT calculations. This procedure differs from the traditional approaches in which the model parameters are determined from empirical data, and offers the possibility of systematically constructing detailed, realistic models of material behaviour at longer scales. Parameters obtained using these potentials can be used to inform larger scale techniques, for instance the discrete dislocation dynamics method (DDD), a mesoscale approach aimed at the simulation of the collective behaviour of a large ensemble of dislocations [122; 123]. A prominent example of an atomistically informed DDD implementation is described in Reference [124]. In this work, the dislocation dissociation into SPs is accounted for by allowing splitting of highly connected dislocation nodes and by including the intrinsic stacking fault energy of a Cu crystal in the evaluation of an effective force acting on the dislocation, which is added to the traditional stress-derived force given by the Peach-Köhler formula $\mathbf{F} = \sigma\mathbf{b}$. The ISF energy is obtained from structural optimisation of a relevant atomistic structure using an EAM potential. Other parameters obtained using this potential are the

drag coefficients B_g, B_c for both glide and climb, used to implement the kinetic law of the $\mathbf{f} = B\mathbf{v}$ type, where $\mathbf{f}$ is the force acting on a dislocation segment and $\mathbf{v}$ the velocity. Another useful parameter, obtained by geometry optimisation of the atomistic system, is the dislocation core energy, i.e. the energetic contribution that can not by described by continuum elasticity. This allows for local corrections to the forces acting on each segment. The explicit implementation of SPs allow for the definition of cross-slip rules consistent with fcc geometries, assumed to be either of Friedel-Escaig or of the Fleischer type [29]. These phenomena occur within the DDD algorithm, without further parametrisation. The resulting technique is capable of describing typical dislocation junctions in fcc crystals, such as Lomer-Cottrell locks.

More generally, the dislocation interaction with obstacles is desirable in order to model its motion from a mesoscale perspective [125]. This can be hardly achieved in the case of chemical impurities by means of interatomic potential, and atomistic data should be calculated using first-principle techniques. In References [70; 71] the dislocation interaction energy with a selection of impurity atoms is calculated in molybdenum and aluminium respectively by means of DFT. The lattice Green function boundary condition method is used to decrease the size of the system required to converge the long range dislocation elastic field. This energetic profile is used to fit a model describing dislocation glide under an applied stress, identifying the possible pinning points as a function of the density of impurity atoms.

Another notable example of hierarchical multiscale modelling is presented in References [55; 56], in which the effect of chemical impurities (Re, W, Ta, Mo) on vacancy diffusion in Ni alloys is investigated. The solute-vacancy binding energies and the diffusion barrier are calculated using a DFT-based approach, relying on the climb-image NEB method. The energetics are then used to parametrise a kinetic Monte Carlo model, capable of evaluating the diffusion coefficient as a function of the chemistry of the alloy. Since disloca-

tion climb is mediated by vacancies, measuring these diffusion coefficient can allow for the definition of dislocation climb velocity, incorporating chemical complexity not achievable using interatomic potentials.

The Peierls-Nabarro model predicts the equilibrium dislocation structure by balancing a repulsive elastic stress among infinitesimal dislocations and an attractive restoring stress [126; 127]. The latter can be parametrised using the generalised stacking fault energy curve, evaluated using atomistic simulations. The usage of first principle calculations for this purpose can add chemical complexity to the model, capturing the role of chemical impurities. Despite its simplifying assumptions, this continuum model is capable of predicting both hydrogen and oxygen effect on crack tip plasticity in Al, as shown in Reference [74] by comparison with QM-accurate simulations.

A connection map showing the hierarchal modelling scheme is schematised in Figure 2.3. For a more general review of hierarchical multiscale methods see Reference [128]. Despite its successes, the hierarchical approach has some limitations, being constrained to those cases where the high level parameters are completely specified from the more detailed calculations. This is certainly not true when the system trajectory involves bond breaking or formation or other strong chemical interactions (e.g. charge transfer) which is outside the transferability range of any fixed classical model. In these cases, QM accuracy is required on the system subregion where these processes occur. On the other hand, such a calculation must take into account the long-range elastic coupling with the rest of the system. Systems in which the atomistic process are strongly influenced by these interactions are named 'strongly coupled multiscale systems', and the chemical mechanisms are named 'chemo-mechanical' processes. Over the last twenty years there has been much effort to develop schemes for addressing these kind of problems, and recently (2013) the Nobel prize has been awarded to M. Karplus, Michael Levitt and Arieh Warshel for "Development of Multiscale Models for Complex Chemical System".

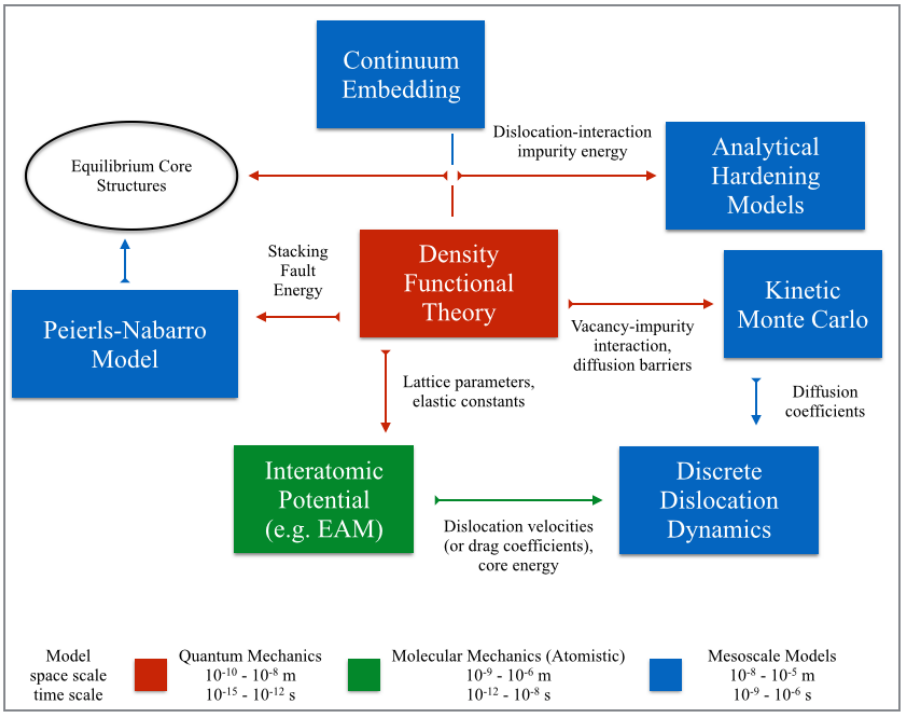

Figure 2.3: Multiscale hierarchical scheme for dislocation modelling.

In this work, the concurrent bidirectional coupling between Quantum Mechanics (QM) and Molecular Mechanics (MM) will be addressed. This QM/MM scheme is aimed at the chemically accurate simulations of dislocation cores in Nickel-based alloys, accounting for chemical complexity and transferability to MM atomistic modelling. Another advantage is the possibility to validate empirical interatomic potentials against this more accurate (and therefore more computationally expensive) technology. One major advantage of this method with respect to other QM-accurate setups for dislocation modelling (e.g. lattice Green function flexible boundary conditions [66] or the QM-CADD approach [72]) is that temperature effect can be explicitly modelled. This feature is particularly relevant to Ni superalloys, as they are typically used for high temperature application (e.g. engine turbine blades).

Identification of the QM region

The starting point of a QM/MM simulation consist of deciding which atoms can be treated with the MM method and which ones require the QM augmentation. The QM zone is usually centred at a crystal defect (e.g. a dislocation or a vacancy). In this work, the extension of this region is checked by carefully comparing the MM forces with the QM ones during a dynamical simulation, as illustrated in Chapter 5, or by analysing the convergence of electronic properties (magnetic moment, density of states) to bulk values while moving further from a defect. The latter method is applied when a set of MM forces is not available (e.g. in the case of a chemical impurity). The defect can move from its original site as the dynamics of the systems is simulated, and the QM region must be consistently updated. Within many embedding schemes, the QM zone is fixed [73]. This involves the usage of a large QM region so that the defect of interest will not move outside, making these schemes computationally inefficient. Frequently updating the QM region instead, allows a minimal QM region to be used, which results in a more efficient calculation. On the other hand, frequent updates of the QM region (which modifies the number of atoms, and their distribution in space) can also cause computational inefficiency. Ideally, the charge density from a converged calculation should be reused as initial guess whenever is possible. Note that schemes making use of QM region updating do not conserves the total energy of the system, as the Hamiltonian is time-dependent.

One possible robust implementation of the selection algorithm is based on hysteresis [73]. The criteria to be fulfilled for an atom to became selected as QM particle are more strict than the ones to became unselected. This is usually employed using Euclidean distances, in particular by defining an internal (radius r_-) and an external (radius r_+) circle centred on the QM core. An atom has to be enclosed within the internal circle to became QM-selected, but it changes back to its former MM status only when the distance from the QM-core is larger then r_+. This scheme is shown in Figure 2.4.

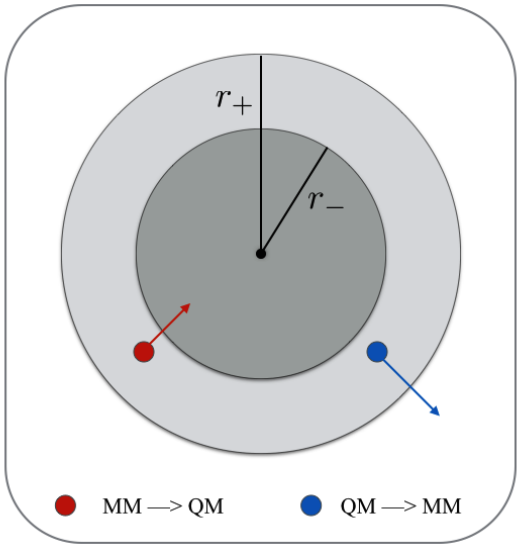

Figure 2.4: Hysteretic selection of the QM region. The red atoms is entering the inner circle, changing its state from MM to QM. The blue atoms instead is moving outside the outer circle and becoming a MM atom.

Force and Energy Mixing

Once the QM and MM regions have been identified calculations are performed for each system and the results merged in order to integrate the dynamics of the system. A certain continuity is required between the QM and the MM methods, so that spurious interaction will not affect the dynamics of the system. The equilibrium lattice constant of the MM model can easily be matched to the QM prediction by adjusting the length scale of the potential, as described in Reference [129]. If this requirement is not met, the QM region is subjected to a hydrostatic stress field. Since the MM part provides elastic embedding to the QM region, matching of the elastic constants is also important in order to capture the correct deformation mechanism of the system. The matching of phonon frequencies is also important [73], as it prevents reflection of waves at the QM/MM interface.

QM/MM Mixing methods fall into two categories: energy and force mixing. Within energy-mixing coupling schemes, the QM region is passivated but not buffered. Within the ONIOM method [77], one of the first energy-mixing schemes developed, the total energy of a system is defined as

$$E_{tot} = E_{\mathrm{MM}}^{\mathrm{sys}} + E_{\mathrm{QM}}^{\mathrm{clust}} - E_{\mathrm{MM}}^{\mathrm{clust}} \tag{2.78}$$

where $E_{\mathrm{MM}}^{\mathrm{sys}}$ is the energy of the whole system calculated with the classical potential, and $E_{\mathrm{QM}}^{\mathrm{clust}}, E_{\mathrm{MM}}^{\mathrm{clust}}$ the energy of the passivated cluster evaluated with respectively the QM and the MM method. The correctness of this scheme is based on a delicate cancellation of errors for the passivated surface states between the two methods. More refined version of this method makes use of a buffer region in order to improve this delicate matching [130; 131].

The Force-mixing schemes rely on forces calculated on subset of the system (clusters). These clusters are usually comprising of the QM region and of an external 'buffer', required for decoupling QM core atoms from spurious surface states. Its width depends on both the material and the chemical complexity of the QM region. The QM bonding is non-local and the convergence of the cluster-QM forces to the bulk target values is related to the decay in real space of the density matrix, which can be shown to be exponential for insulators and metals at finite temperatures [132]. For covalent materials, slow convergence with respect to the size of the buffer region is caused by dangling bonds at the surface. This problem is usually addressed by passivating these bonds using hydrogen atoms. The usage of such an algorithm is not required for metallic systems, due to screening and to the lack of directional bonding. However, metallic surfaces have a larger magnetic moment with respect to bulk. This may cause long range spin rearrangement and slow down the convergence of quantum forces. In this work the convergence of QM forces is studied for a number a Ni-based system, including chemical impurities (Re,W). A comparison is then made with α-Fe, a more challenging material for QM/MM schemes because of its a large magnetic moment.

The 'Learn on the Fly' Scheme

The 'learn on the fly' (LOTF) scheme [7; 133] belongs to the force-mixing methods category. It is based on the fitting of a new energy function for the system, capable of reproducing the QM and MM forces previously calculated. The dynamics is propagated using this unique 'corrected' Hamiltonian, thus conserving momentum, in contrast to the merged QM and MM forces. If the deviation between the QM and MM method is not large, the energy functional does not need to be refitted at every time step of the MD simulations, and expensive QM calculation can be avoided by making use of a predictor/corrector scheme [73]. As for standard force-mixing QM/MM methods, the total energy of the system is not conserved, due to the fact that the Hamiltonian is time-dependent because of the refitting procedure.

When this scheme was first introduced [133], the interatomic potential itself was refitted. It has later been recognised that, as IPs can have a rather complicated functional form, it is less costly to add a correction term to the unmodified classical Hamiltonian. This term is chosen to be a two body term

$$V_c = \sum_{i<j} V_{\alpha_{ij}}(r_{ij}) \tag{2.79}$$

where the indices i, j are summed over a region comprising of the QM zone and of a neighbouring section of the MM one. The parameters α_{ij} are fitted in such a way that

$$\frac{\partial V_c}{\partial x_i} \longrightarrow F_i^{\mathrm{QM}} - F_i^{\mathrm{MM}} \tag{2.80}$$

It can be demonstrated [73] that the potential V_c can be taken to be linear without significant accuracy lost. As in the case of others force-mixing schemes, a buffer region is required for the QM calculation, thick enough to decouple the QM atoms from spurious surface effects. Note that the forces calculated on this buffer region are not physical and are therefore discarded. This scheme is summarised in Figure 2.5.

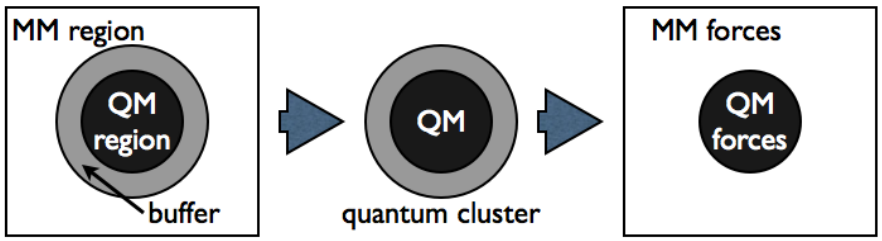

Figure 2.5: Schematic description of the LOTF scheme.

The following steps summarise the LOTF method.

1. **Initialisation** The active fit region is defined and the potential (2.79) is initialised by computing QM and MM forces.

2. **Extrapolation** The new Hamiltonian is used with fixed parameters to propagate the dynamics for N_{interp} steps.

3. **Optimisation** The QM selection is updated, the forces computed and the adjustable potential re-optimised.

4. **Interpolation** The system is returned to its before-extrapolation state and the dynamics re-integrated, interpolating the parameters between the old and new values. Return to 2

The advantage of using this predictor/corrector scheme is clear from Figure 2.6, in which the forces acting on the QM atoms at a dislocation core in γ are compared to the ones obtained from a much slower simulation, in which the QM forces are computed at every timestep of the MD simulation (2 fs). The force error with respect to the latter dataset increases linearly at the 'predictor' stage, in which the potential term V_c is a constant. At the 'corrector' stage, corresponding to the actual LOTF QM/MM simulation, the error is much lower, and its maximum is encountered at the timestep corresponding to half of the period between QM calculations. Two datasets

are compared, corresponding to two different lengths of this period (10 and 20 fs). The force errors calculated at the 'predictor' stage (left panels) are to be disregarded, as they do not pertain to the actual QM/MM simulations. The ideal period between QM calculations has to be chosen in such a way that the errors obtained at the 'corrector' stage are comparable or smaller to the force error due to the finite cluster approximation (cf. Section 5.3), which corresponds to the overall accuracy of the QM/MM simulation. In this work, this threshold is set to 0.1 eV/Å, good compromise between accuracy and computational cost of the QM calculations. Further testing revealed that the maximum period that would correspond to maximum 'corrector' force errors below this value is 14 ps (7 timesteps). This is consistent with the period of 10 fs obtained for a Si system [73].

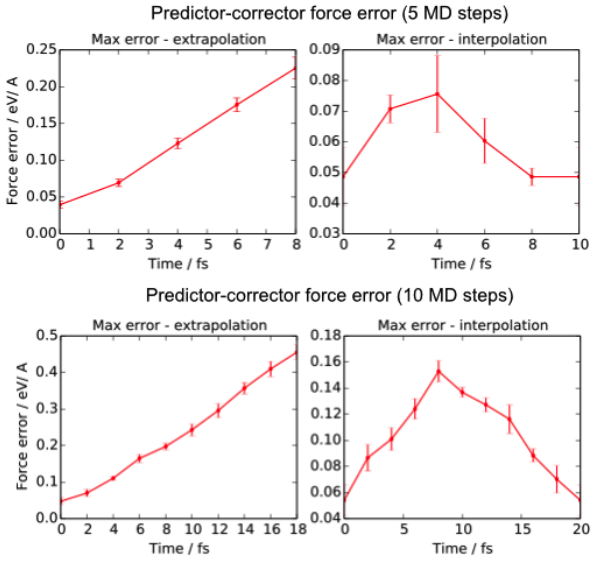

Figure 2.6: Predictor-corrector force error for atoms at a screw dislocation in γ-Ni. Datasets for 5 and 10 interpolation steps.

2.8 Summary

In this Chapter the main methods for describing atomistic systems have been introduced. Electronic structure based methods are accurate and transferable, but computationally expensive. Interatomic potentials offer a tool for describing large systems for longer simulation times, and can be optimised through a set of fitting parameter so that they reproduce either experimental or *ab initio* data. Transferability to phases different from the one they have been fitted for is not granted, and only a certain number of different atomic species can be simulated. Concurrently the most common techniques used for simulating the dynamics of atomistic system have also been described. Geometry optimisation was introduced as a tool for looking for local minima in the potential energy, and the NEB method as a way for measuring the barriers between them. Finally, methods for combining QM and MM approaches were described, focussing on the 'Learn on the Fly' (LOTF) scheme, used in this work.

CHAPTER 3

Properties of Nickel Alloys

3.1 Introduction

A selection of calculations for structural and electronic properties of Ni alloys is presented in this Chapter, performed with the aim of providing a general understanding of key properties of this class of materials by means of first-principle methods. The second main objective of the Chapter is to verify the capability of the interatomic potential developed by Y. Mishin [5] in reproducing *ab initio* results for systems of increasing complexity.

As a starting point, structural and elastic properties are evaluated for elementary cells of γ and γ' (Sec. 3.2), and the energetic cost for creating a coherent interface is discussed. In Section 3.3 the effects of temperature in bulk systems are studied: the thermal expansion coefficient is evaluated by means of MD simulations in the in the NPH ensemble, and the accuracy of EAM forces tested against DFT reference data. The energetics of vacancies and Al impurities in the γ phase is studied in Section 3.4, and a disagreement between EAM and DFT is found in the second case. An *ab initio* study of Re and W impurities in γ and in γ' is then reported, showing a good agreement with experimental and theoretical evidence.

Dislocations in fcc materials dissociate into Shockley partials, separated by a stacking fault, characterised by atoms presenting hexagonal close packed (hcp) symmetry. With the aim of investigating the transferability of the EAM to relevant structures, the elastic properties of this phase, not included in the fitting set of the potential, are investigated in Section 3.5. A discrepancy with respect to *ab initio* data is observed, arising from the functional form of the pair-interaction potential term. An analysis of the generalised stacking fault (GSF) energy curve is offered in Section 3.6. A detailed study is presented for both the γ and the γ' phase, and the effect of chemical impurities and their distribution in the matrix is discussed. This is particularly important as it provides insight on the energetics for slip deformation in the γ phase.

Electronic structure DFT calculations are performed adopting a basis set of plane waves, as implemented within the VASP package [10]. The PBE/GGA approximation is adopted for the exchange and correlation energy [92], and BZ sampling is carried out using MP grids [99], using different meshes for systems of different size. Convergence of the total energy if the system within the threshold of 5 meV is achieved for elementary 4-atom cubic cells using a $13 \times 13 \times 13$ grid centred on the Γ point. A 300 eV cutoff for the kinetic energy is used whenever cell optimisation is not required. Its value is otherwise increased to 400 eV in order to reduce the contribution of the Pulay term [134] to the diagonal components of the stress tensor. The PAW approach [135] is used for smoothing rapidly oscillating wavefunctions pertaining to core electrons. Gaussian electronic smearing based on the method proposed by Methfessel and Paxton [100] is used to improve the convergence of the self-consistent calculations. A broadening of 0.1 eV is deemed sufficient to significantly reduce charge sloshing at the Fermi level, and it is small enough not to affect the electronic structure for the considered systems. The residual minimisation method [11] is used for electronic relaxation, and the projection operators are evaluated in real-space in order to accelerate the calculations for large systems.

3.2 Bulk Properties

In this Section the bulk properties of pure phases of the alloy are investigated. The resulting data for γ and γ' show an excellent agreement between the QM and MM methods. This is an expected result, as these data are included in the fitting set for the classical potential. The coherent interphase boundary is then studied, finding again good agreement between the two methods. Finally, basic electronic properties are evaluated using the QM model.

Structural Properties of γ and γ' Crystals

The structural properties for γ and γ' crystals are evaluated using 4-atom elementary cells, with a simple cubic Bravais lattice. This corresponds to an fcc structure if all the atoms have the same chemical species, and to $L1_2$ if one of the them is different. The equilibrium volumes are determined by performing a set of 11 calculations for each phase ($\pm 5\%$ from the experimental values for the lattice parameters). The total energy is evaluated, and the results are fitted to the Murnaghan equation of state [136]

$$E(V) = E_0 + BV_0\left[\frac{1}{B'(B'-1)}\left(\frac{V}{V_0}\right)^{1-B'} + \frac{V}{B'V_0} - \frac{1}{B'-1}\right] \tag{3.1}$$

where B is the bulk modulus, B' its derivative with respect to pressure, V_0 the equilibrium volume and E_0 the cohesive energy of the bulk structure. The latter is evaluated as the energy difference between the bulk system and an isolated atom, modelled using a cubic simulation box. The DFT atomic ground state is obtained by fixing the magnetic moment to the expected value by constraining the occupancy of the electronic bands. The atom is separated from its periodic replicas by 15 Å of vacuum, and the BZ is sampled using only its central point Γ. Results are reported in Table 3.1, together with known experimental values [95; 137], included in the fitting set of the IP. Good agreement is found between QM and MM data.

The formation energies evaluated using DFT are overestimated by about 0.3 eV/Å, consistently with reported values for this calculation [138].

	γ			γ'		
(a)	DFT	EAM	EXP	DFT	EAM	EXP
a (Å)	3.52	3.52	3.52	3.57	3.57	3.57
E_c (eV)	4.73	4.44	4.44	4.88	4.63	4.62
B (GPa)	192	181	181	178	176	176
B'	4.7	4.4	-	4.7	5.7	-
(a)	DFT	EAM	EXP	DFT	EAM	EXP
C_{11} (GPa)	268	237	241	236	236	230
C_{12} (GPa)	161	151	151	147	154	149
C_{44} (GPa)	127	125	127	126	127	132

Table 3.1: Comparison between DFT, EAM and experimental data for the bulk properties of γ and γ': (a) equilibrium parameters obtained from a Murnaghan fit to the $E(V)$ curve and (b) elastic constants from a linear fit of the stress/strain curve.

Elastic constants C_{ij} relate the applied strain ϵ_i to the resulting stress $\sigma_i = C_{ij}\epsilon_j$. There are only three independent constants for cubic systems, and the stress/strain equations assume the simple form:

$$\sigma_{xx} = C_{11}\epsilon_{xx} + 2C_{12}\epsilon_{xy} \quad ; \quad \sigma_{yz} = C_{44}\epsilon_{yz} \tag{3.2}$$

The stress tensor is calculated as the derivative of the total energy with respect to strain, normalised to the volume of the cell, and the elastic constants are obtained by a linear fitting of the stress/strain curve. Five configurations are used, with strain values of $\pm 2\%, \pm 1\%, 0$. The strain components ϵ_{xx} and ϵ_{zy} are applied simultaneously to the unitary cell, as they contribute to independent components of the stress tensor. The kinetic cutoff energy for DFT calculations is increased to 400 eV, as accurate diagonal elements of the virial are required. The results are presented in Table 3.1, and show good agreement between QM and MM methods. This is an expected result, as the potential is fitted to the experimental data summarised in Table 3.1.

Coherent Interphase Boundary

The interfacial energy in Nickel superalloys can be minimised by allowing the crystallographic planes of the cubic matrix and precipitate to remain continuous. As the volume of the precipitate increases, the morphology changes from spherical to cuboidal structures [2]. The local environment at the interface depends on the lattice mismatch between the phases, defined as

$$\delta = 2\frac{a_{\gamma'} - a_{\gamma}}{a_{\gamma'} + a_{\gamma}} \tag{3.3}$$

where a_X is the lattice parameter for the X phase. It can have positive or negative sign, depending on the composition and on the operating temperature of the alloy. In either case, a network of misfit (edge) dislocations is formed at the γ/γ' interface, so that the interfacial strain is minimised [1]. In this Section, the interface is modelled in the region far from the dislocation cores, where the interphase boundary is coherent. This allows the usage of small model structures (less than 100 atoms) so that calculations can be accomplished using *ab initio* methods. The comparison with EAM data constitutes a further test of the reliability of the latter.

A periodic model system is built by creating supercells for γ and γ' of N atoms each using the same lattice parameter, and putting them side by side in order to simulate a coherent interface. The interfacial energy per unit area α is defined for this periodic structure as

$$\alpha = \frac{E_{\text{tot}} - E_{\gamma} - E_{\gamma'}}{2A} \tag{3.4}$$

where E_{tot} is the total energy of the system ($2N$ atoms), E_{γ} and $E_{\gamma'}$ the energies for bulk references (N atoms each) and A the area of the interface. The factor of two accounts for the fact that two interfaces are created because of the periodic boundary conditions. Both atomic positions and simulation boxes are then optimised using the conjugate gradient algorithm with an

energy threshold of 10^{-3} eV. The relaxed structure has a lattice parameter which is an average, weighted by the elastic constants for the two phases, between the single-phase equilibrium values. This leads to tensile strain in γ and compressive strain in γ'. The corresponding contribution to the total energy of the system is proportional to the size of the cell [139]. In order to decouple the local energetic contribution from the elastic one, several simulations for system of different length along the normal to the interphase boundary (IPB) are performed. The energy cost for creating an interface is evaluated via Equation (3.4), and a linear fit is used for extrapolating the value to $N = 0$, where the elastic contribution vanishes. This approach gives accurate results in the case of simple (100) interfaces. Whenever larger systems are required, linear fitting of DFT data is no longer accurate and other approaches are used. In Reference [27], interfacial energies are calculated using strained bulk references, as the simulation box is optimised only along the normal to the IPB.

Practical calculations are performed using $1 \times 1 \times 2n$ supercells of the primitive cubic crystal, for $n = 1, 2, 4, 8$. Results for $n = 1$ are discarded as the two IPB are too close, and their interaction energy will give rise to a spurious energy term. The Brillouin zone is sampled using a $16 \times 16 \times \frac{16}{2n}$ for QM calculations. The obtained results of 46 and 42 mj/m^2 for QM and MM calculations respectively show a good agreement between the simulation techniques, despite a discrepancy in describing the elastic energy term due to different values for C_{11}, as reported in Table 3.1. The agreement with respect to the values reported in literature [27] is good. It should be noted that the EAM potential fails to describe the energy ordering of interfaces [5]. This discrepancy with respect to DFT and experimental data does not affect this work, as only (100) interphase boundaries are considered.

Electronic Properties of γ and γ' Crystals

Electronic properties for the bulk models of the γ and the γ' phases are investigated by means of DFT, restarting from converged charge densities and switching the partial occupation scheme to the tetrahedron method with Blöchl corrections, known to produce accurate DoS [98]. The values for magnetic moments of Ni atoms, calculated using the Bader charge analysis, are reported in Table 3.2. Aluminium is not magnetic in either phase.

	γ	γ'
m (μ_B)	0.63	0.25

Table 3.2: Magnetic moments for Ni atoms in the γ and in the γ' phase.

The projected density of states for Ni (d states) and Al (p states) are reported in Figure 3.1, shifted so that the Fermi level is at 0. In panel (a) state depopulation is observed at 0 eV (spin down) and at -0.5 eV (spin up). This causes the magnetisation difference between the phases. The interaction between Ni and Al is negligible in the range -1.5–0 eV. The electronic structure of Al presents major differences between the phases below -1.5 eV. As can be observed in Figure 3.1(b), the flat DoS typical of fcc Al is replaced by localised peaks. Hybridisation between d_{z^2} states of Ni and p_z states in Al is observed at -3 eV.

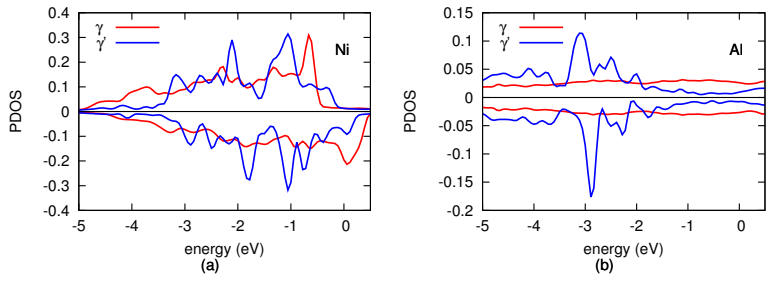

Figure 3.1: Projected density of states for bulk γ and γ' structures for (a) Ni atoms and (b) Al atoms.

3.3 Temperature Effects

In the previous Section the capability of the EAM potential in reproducing experimental and *ab initio* data is analysed for structural zero-temperature properties for bulk models of the γ and γ' phases. Before moving to more complex systems including crystallographic defects, the accuracy of the EAM potential in reproducing ionic temperature effects in bulk system is studied in this Section. As a first step, the thermal expansion coefficient is evaluated. Large supercells are required to suppress the fluctuations typical of MD simulations in an isobaric ensemble, and only EAM calculations are performed. Results show an underestimation of thermal expansion with respect to experimental data. The accuracy of the forces predicted by EAM during a MD simulation in the canonical ensemble is then tested versus DFT data.

Thermal Expansion

Thermal expansion produces effects that cannot be neglected for realistic atomistic simulations of the alloy at operating conditions. It is well established that the sign of the lattice mismatch (3.3) between γ and γ' depends on temperature. The linear thermal expansion coefficient is larger for the fcc matrix than for the precipitate phase, and therefore the lattice misfit become negative for high operating temperatures. The presence of impurities such as rhenium, that segregate only in the γ phase, increases the low temperature lattice parameter for the γ phase and decreases its thermal expansion coefficient. This can form alloys that exhibit a negative lattice misfit at low temperatures (e.g. EMSX-4). It has been shown that also for these alloys thermal expansion effects would decrease the lattice misfit [140].

In this Section the linear expansion coefficient for pure phases of the alloy is evaluated by means of MD simulations within the isoenthalpic-isobaric NPH ensemble. The linear expansion coefficient is evaluated by direct comparison between interatomic distances for thermalised structures.

The thermal strain is defined as

$$\varepsilon(T) = \frac{\ell(T) - \ell_0}{\ell_0} \tag{3.5}$$

where ℓ is a generic interatomic distance and ℓ_0 its value for $T = T_0$. In this study, we have selected $T_0 = 0$ and limited ourselves to measuring the variation of distances between nearest neighbours (n.n.) atoms. The MD simulations make use of the combination of Nosé-Hoover [82; 83] and Parrinello-Rahman [118] dynamics proposed by Melchionna [141; 142]. Model systems are $8 \times 8 \times 8$ supercells of the bulk systems used in Section 3.2, so that correlation effects, known to produce major fluctuations of bulk properties at high temperature, are minimised. The initial velocities are set accordingly to a Maxwell-Boltzmann distribution associated with an initial value of twice the target simulation temperature. This would guarantee the system to thermalise to the correct kinetic energy, due to the equipartition theorem. The equations of motion are integrated every 2 fs, and the characteristic barostat timescale is set to 75 ps. The system is thermalised for 5 ps before data collection. Production calculations involve 50 ps of dynamics for each system. The distance between neighbouring atoms is measured every 0.5 ps in order to minimise the correlation between snapshots.

The calculated values for the thermal strain are shown in Figure 3.2. Similar results are obtained for the two phases, and the strain/temperature relation deviates from the linear regime for temperatures higher than 400 K. There is good agreement with Reference [5], in which atomic motion is simulated via a Monte Carlo technique, and only small discrepancies arise at high temperature, probably due to the different size of the simulation cells. Reasonable agreement with experimental results is found. The EAM potential underestimates the expansion, as thermal effects are introduced only within the the local harmonic approximation during the fitting process. The thermal strain (3.5) can be written as $\varepsilon(T) = \alpha T$, where α is the coefficient of linear expansion, calculated from a linear fit of the data. The obtained values

are $5.9 \pm 0.2 \times 10^{-6}\mathrm{K}^{-1}$ for the γ phase and $5.6 \pm 0.1 \times 10^{-6}\mathrm{K}^{-1}$ for γ'. These numbers are smaller than the experimental values of about 13.1 for γ and $12.3 \times 10^{-6}\mathrm{K}^{-1}$ for γ' [143; 144] and with respect to the values of 13.1 and 12.3 $10^{-6}\mathrm{K}^{-1}$ reported as the result of *ab initio* simulation [145] under the quasi-harmonic approximation. Another flavour of EAM underestimate the expansion [146], while Sutton-Chen potentials give a larger estimate [147].

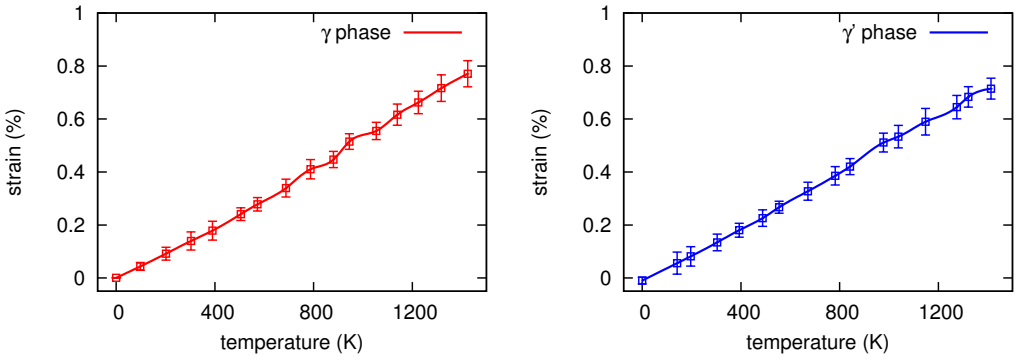

Figure 3.2: Thermal expansion curve for γ and γ' calculated from MD simulations within the NPH ensemble.

Temperature Dependent MM Force Error

In the previous section a disagreement between DFT and EAM in describing thermal expansion of the system is found. This property is obtained through averages over long MD simulation, and does not contain information about the local accuracy of the IP. The aim of this Section is to test the ability of the MM potential to reproduce the QM forces for systems thermalised at different simulation temperatures. This is needed to correctly predict thermodynamic observables [148], and can also improve the multiscale embedding by reducing force fluctuations on the atoms at the boundary between the QM and the MM regions (this is also addressed by using a hysteretic QM selection scheme, depicted in Figure 2.4). Bulk structures are modelled, using $3 \times 3 \times 3$ 108-atom supercell for both phases. Classical MD simulations are

carried out in the NVT ensemble, using volumes consistent with thermal expansion (as predicted by the EAM potential). The model systems are initially equilibrated for 5 ps, using a 2 fs time step. This is followed by a 10 ps production stage during which configuration snapshots are collected at 1 ps intervals. The DFT forces are calculated on these structures and compared with the IP results. This analysis is repeated for four different temperature values (300K, 600 K, 900 K, 1200 K) for both γ and γ'. The average errors are reported in Table 3.3.

T(K)	300	600	900	1200
ΔF_γ (eV/Å)	0.07 ± 0.02	0.10 ± 0.02	0.12 ± 0.03	0.13 ± 0.04
$\Delta F_{\gamma'}$ (eV/Å)	0.10 ± 0.02	0.14 ± 0.04	0.16 ± 0.04	0.18 ± 0.05

Table 3.3: Average force error of the EAM potential computed as deviation from the reference DFT calculations.

The corresponding distribution plots of the deviation between the forces produced by QM and MM methods are displayed in Figure 3.3. These results suggest that for perfect bulk systems the IP is remarkably accurate, with more than 70% of the absolute errors contained below the 0.1 eV/Å threshold for room temperature simulations in the γ phase. This average error however increases for higher temperatures, and approximately doubles by T=1200 K (Figure 3.3 and Table 3.3).

The distribution plot of the relative error is displayed in Figure 3.3. Only small differences can be appreciated between the plotted curves at different temperatures. This indicates that the force deviation is approximately proportional to the magnitude of the forces. The EAM potential is therefore sufficiently accurate for simulating the dynamics of bulk systems even at relatively high temperatures. The test is not performed for temperatures above the melting point, as the goal of the project is the simulation of the alloy subjected to typical operating settings of turbine blades. Qualitatively similar results are obtained for the γ' phase, for which the IP proves to be less accurate. Only about 40% of the forces are accurate within 25% of the

reference *ab initio* values. This is probably due to the greater chemical complexity of the material, and it is consistent with the observation that the task of fitting accurate interatomic potentials for systems including several atomic species is notoriously challenging [149].

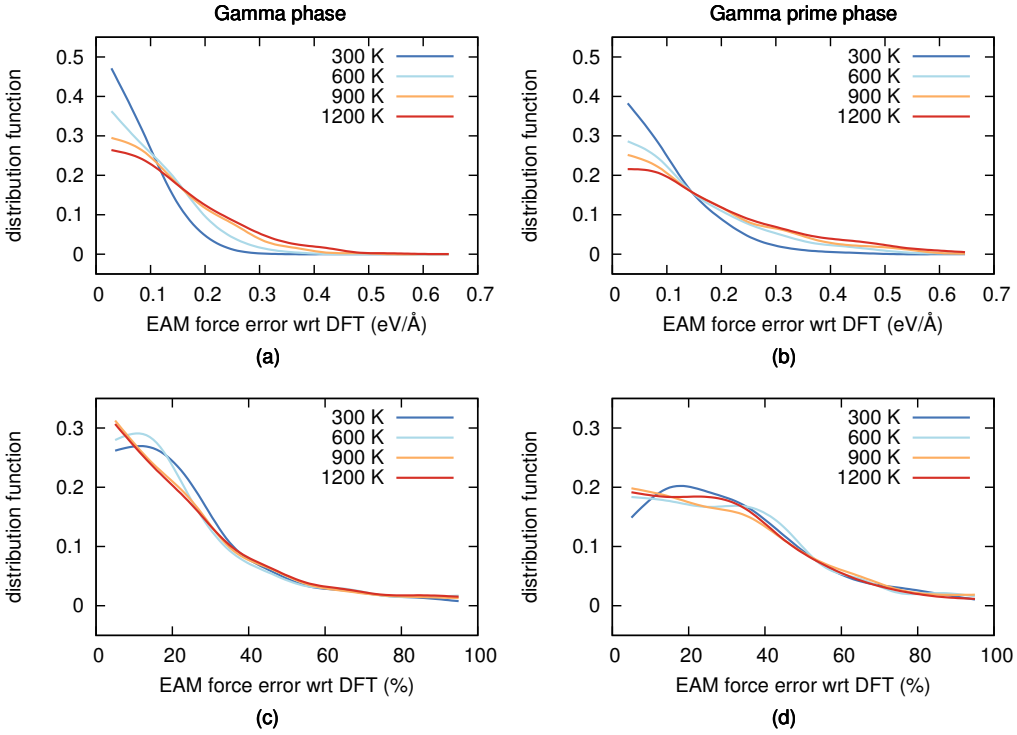

Figure 3.3: Distribution functions of the deviation of forces calculated using the EAM potential with respect to DFT references. Absolute deviations in panels (a,b) and percentage in panels (c,d) for MD simulations at different temperatures for (a,c) the γ and (b,d) the γ' phase.

3.4 Point Defects

In this Section the energetics of point defects are analysed using *ab initio* calculations and, whenever applicable, the EAM potential. Accuracy is particularly needed for vacancies in the γ phase, as they are a crucial ingredient for dislocation climb. Isolated impurity atoms are investigated, and the substitutional formation energy evaluated for the two phases of the alloy. This is useful for determining the partitioning of the chemical additives.

Vacancies

Vacancies are usually created at interphase boundaries. Their concentration depends exponentially on the formation energy E_f, which can be estimated from atomistic calculations as the difference between the energy of a bulk with a vacant site and the energy of a perfect crystal, renormalised to the correct number of atoms. Its experimental value, along with the migration energy barrier of a vacancy E_m, is included in the fitting set of the IP. It is important to check the consistency of these data with predictions from DFT calculations. Converged results are obtained using a $3 \times 3 \times 3$ supercell of the γ phase. One atom is removed to model a vacancy, and the structure is optimised within a 1 meV energy tolerance using a conjugate gradient algorithm and $4 \times 4 \times 4$ MP grid for QM calculations. The migration barrier is calculated using the NEB method, optimising 3 intermediate images by the RMM-DIIS and the FIRE algorithm for QM and MM calculations respectively. Results are reported in Table 3.4, and show good agreement between EAM and DFT, as the IP overestimates the reference values by 10%.

	DFT	EAM
E_f^v(eV)	1.45	1.57
E_m^v(eV)	1.08	1.19

Table 3.4: Formation and migration energy for a vacancy in the γ phase.

Chemical Impurities

Chemical impurities are known to improve the properties of Nickel alloys, and constitute a significant part of commercial materials. I focus here on elements that are commonly found in Ni-based alloys such as rhenium and tungsten. Aluminium atoms are also included in this study, as they are usually found in the region of the γ phase neighbouring γ'. The EAM potential does not have parameters for chemical species other than Ni and Al, so that most of the analysis presented in this Section is from *ab initio* calculations only.

As a starting point, let us characterise the bulk structures of Al, Re and W in order to verify the agreement between DFT calculations and experimental data. The most stable crystals for Re and W are hcp and bcc respectively. Aluminium atoms form a fcc phase. Spin-polarised DFT calculations show that these structures are not magnetic. The equilibrium lattice parameters are reported in Table 3.5, together with the cohesive energies, and compared to experimental data reported in Reference [95].

	Re		W		Al		
	DFT	EXP	DFT	EXP	DFT	EAM	EXP
a (Å)	2.77	2.76	3.17	3.16	4.04	4.05	4.05
E_c (eV)	7.72	8.03	8.99	8.03	3.56	3.39	3.39

Table 3.5: Equilibrium lattice parameters and cohesive energies for rhenium, tungsten and Aluminium. Comparison between DFT and experimental data.

The agreement between DFT and experiments is satisfactory. The lattice parameters are slightly overestimated, typical issue of GGA potentials, and the cohesive energies are within 5% experimental results. Data for Al are reported in Table 3.5, together with the results from the classical potential. The agreement between the IP and experimental data is also satisfactory. Production calculations consist of $3 \times 3 \times 3$ supercells for either the γ or the γ' phase. An impurity atom substitutes a Ni (or Al) site, and the atomic positions are optimised with an energy threshold of 1 meV.

The substitutional formation energy of atom X is defined as

$$\epsilon_{\text{sub}}(\text{X}) = \text{E}_{\text{tot}} + \mu_0 - \text{E}_{\text{ref}} - \mu(\text{X}) \tag{3.6}$$

where E_{tot} is the total energy of the system including the impurity atom, E_{ref} its value prior to substitution and μ_0 and μ(X) the chemical potentials, chosen to be equal to the per-atom energy of a crystal in its most favourable configuration. With this convention ϵ_{sub}(X) is the sum of two terms. The first one is the difference between the cohesive energy of the impurity atom in the γ (γ') matrix and its value in the ground state geometry, and the second is the cohesive energy change for atoms of the hosting matrix. Other choices for the chemical potentials are possible. For example in Reference [150] they are evaluated as the per-atom energies of fcc crystals.

The substitutional formation energy for an Al atom is the γ matrix is evaluated by means of both DFT and EAM calculations. A disagreement is found between the two methods, as reported in Table 3.6, due to the fact that the largest contribution to the local energy of the Al atom arises from the interaction with the n.n. Ni atoms. This interaction is fitted to reproduce the energetics of the γ' phase, causing overbinding for the Al impurity atom. This have only a minor impact on zero temperature properties, such as the generalised stacking fault energy curve presented in Section 3.6 (see e.g. Figure 3.13), but introduces inaccurate forces during a MD simulations, as pointed out in Section 5.3.

	DFT	EAM
ϵ_{sub}(Al)	-1.54	-1.73

Table 3.6: Substitutional formation energy for an Al atom in the γ matrix. Comparison between DFT and EAM data.

Heavy atoms such as rhenium and tungsten are known to segregate in the γ phase [41], as clear from their substitutional formation energies reported in Table 3.7, predicted to be small in the γ phase and much larger in γ'. In the

latter, the Al sub-lattice is more favourable with respect to the Ni one. This is in line with *ab initio* findings from literature: e.g. in Reference [150], where calculations are performed using a LDA approximation, the substitutional formation energies are larger by about 0.5 eV. The partition of rhenium to the γ phase in also verified in Reference [151] by DFT calculations on a coherent 144-atom model of the γ/γ' interface. The formation energies here evaluated for the tungsten impurity are lower with respect to the rhenium atom, making this atomic specie more likely to be found in the γ' phase, as experimentally verified in Reference [152]. Tungsten has consequently a least evident impact on the plasticity in the γ channels with respect to rhenium.

	γ (Ni)	γ' (Al)	γ' (Ni)
ϵ_{sub}(Re)	0.36	1.04	1.23
ϵ_{sub}(W)	-0.03	0.67	1.11

Table 3.7: Substitutional formation energy for Re and W chemical impurities in the γ and in the γ' phase.

3.5 Elastic Properties of Nickel hcp

Dislocations in fcc crystals are dissociated into Shockley partials separated by region in which the stacking of atomic planes corresponds to a hcp structure. The classical EAM potential developed in Reference [5] is fitted to the energy difference between the fcc and the hcp phase, but not on the elastic constants of the latter. Most of the fault energy curves calculated with this potential are accurate, as demonstrated in Section 3.6 by a comparison with DFT data, but this is not enough to guarantee the correct description of the extended dislocation core region whenever the system is far from equilibrium, as in the case for high temperature MD simulations. In this Section, this issue is addressed by analysing the response of the hcp phase under compression and extension and by comparing it to *ab initio* data.

The system is chosen in such way that the x, y and z directions are parallel to the $[1\bar{1}0]$, $[11\bar{2}]$ and [111] crystal directions respectively. With this choice of axes, elementary cells for fcc and hcp contain 6 and 4 atoms respectively. These structures are periodically reproduced along z, to create two stoichiometric 12-atoms systems. The simulation cells are then compressed and extended (up to $\pm 10\%$, with 1% increments) and the energy difference with respect to the equilibrium structure is evaluated. Results are presented in Figure 3.4 (a,b). The elastic response of the γ phase is accurately reproduced by the IP, as already indicated in Table 3.1. For the hcp phase instead the elastic response is underestimated by the MM potential.

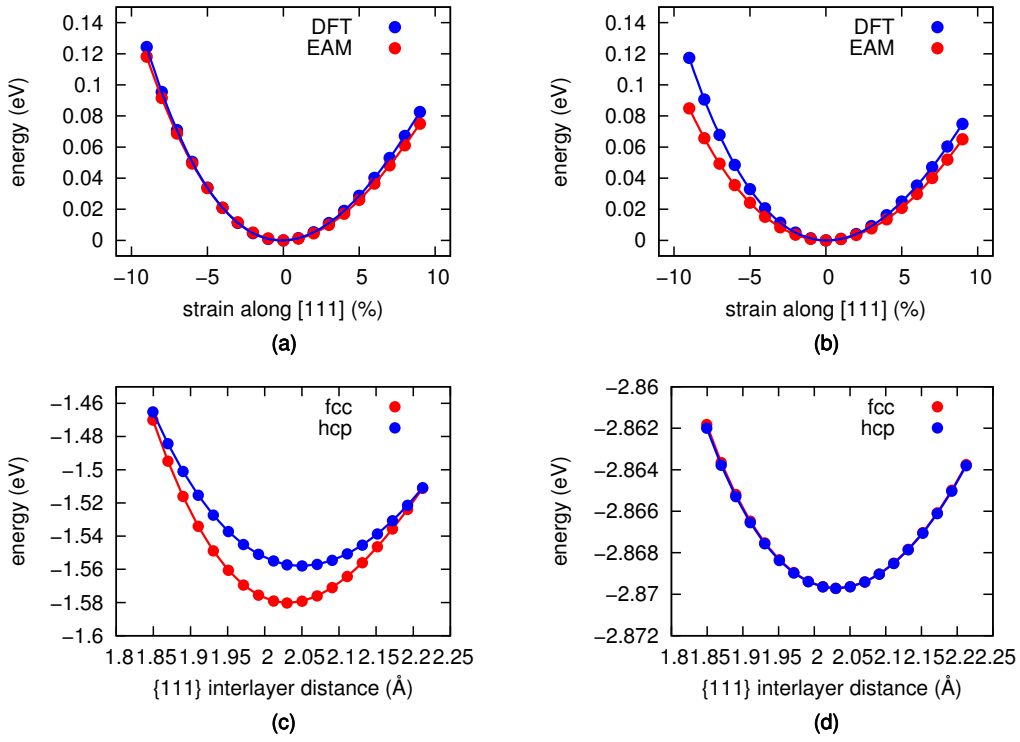

Figure 3.4: Comparison between EAM and DFT data for the elastic response under compression/expansion along the [111] direction for fcc (a) and hcp-Ni (b). Contribution to the total EAM energy from pair interaction (c) and from charge density embedding (d) for fcc and hcp Nickel.

This issue can be investigated by decomposing the total EAM energy of the two systems into contributions, form the pair density and the charge density embedding terms (see Section 2.3 for the definitions of these quantities). Results are presented in Figure 3.4 (c,d). The energetic contribution arising from the charge density embedding function is the same for both phases. This is due to the exponential form for the charge density, which results in small energetic contributions from next nearest neighbours (n.n.n.) atoms. On the other hand, the pair interaction energy is significantly different for the two structures. The underestimation of the elastic moduli is uniquely due to the this potential term.

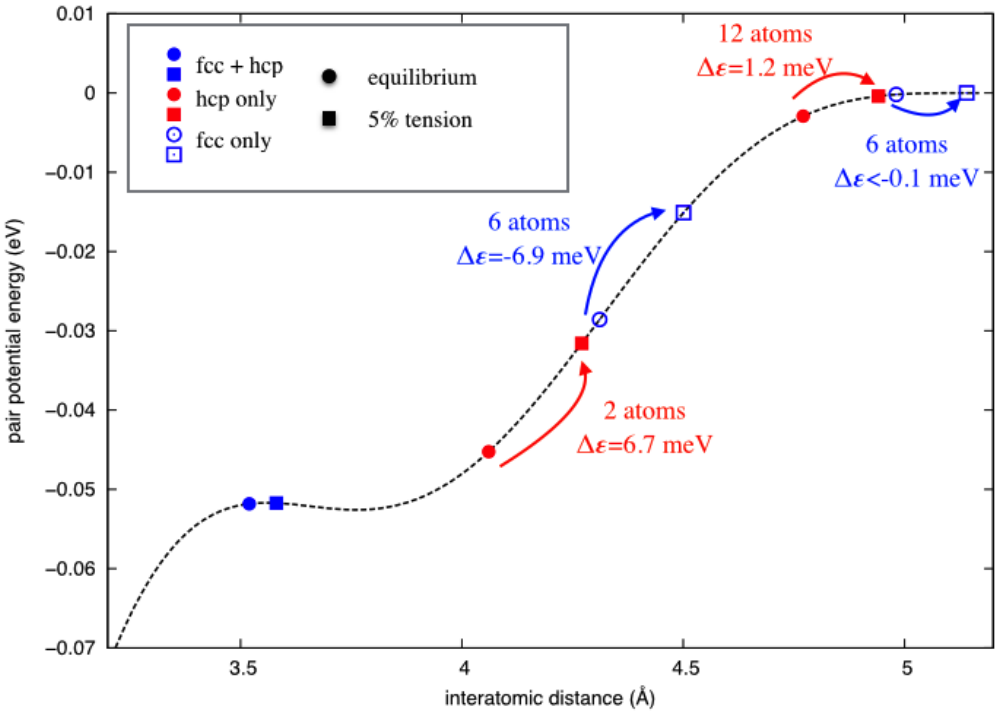

Figure 3.5: Pair interaction energy term for fcc and hcp structures with 5 % tensile strain along the [111] direction. Energy differences with respect to the perfect bulk are indicated for both structures.

This is further investigated by plotting the functional form of the pair interaction (2.33) and by superimposing the distances between neighbouring shells for both structures. The cases of tension and compression are displayed in Figure 3.5 and 3.6 respectively. A strain of 5% is applied, since at this value the deviation of EAM with respect to DFT is already appreciable. Distance/energy data points for equilibrium configurations are indicated with circles. An arrow clarifies the sign of the strain, and data points for deformed configurations are indicated with squares. Filled blue points indicate common shells for fcc and hcp crystals. Filled red ones are used for shells present only in hcp crystals, and empty blue ones are for fcc-only sites.

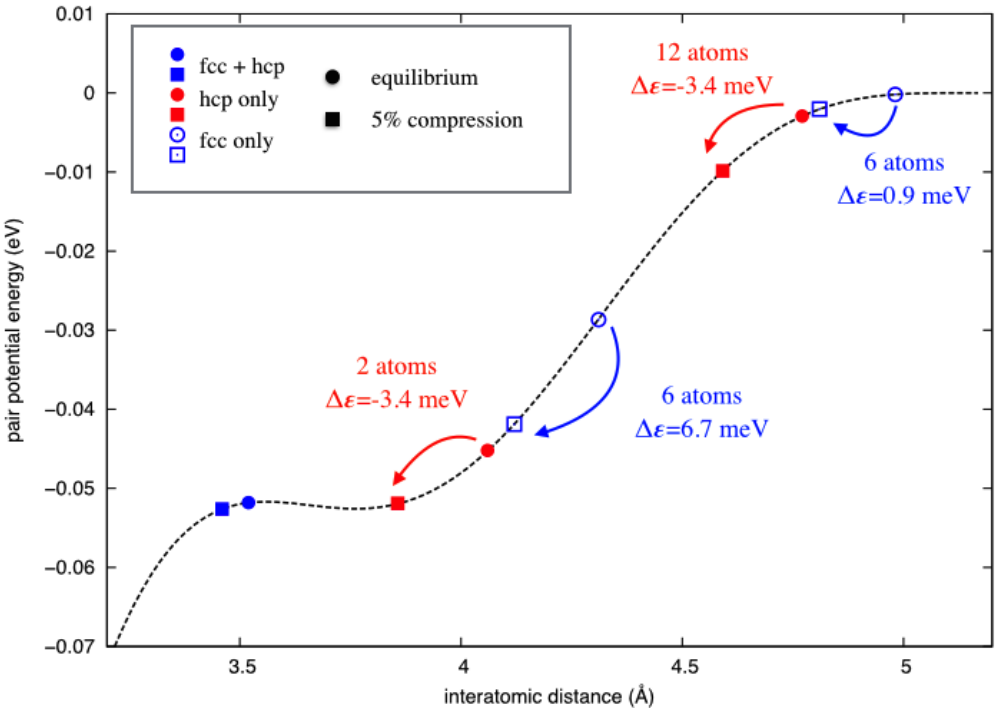

Figure 3.6: Pair interaction energy term for fcc and hcp structures with 5 % compressive strain along the [111] direction. Energy differences with respect to the perfect bulk are indicated for both structures.

From these images it is easy to understand the reason for the underestimation of the elastic response for the hcp structure. As can be seen in Figure 3.5, the hcp structure is missing the 6-atom shell that is giving the major contribution to the energy loss due to tension (6×6.9 eV). Only two atoms in the hcp structure have a similar behaviour, and the other four, being further away because of the different stacking, have only minor effects. A similar effect is observed for the compression regime. The absence of the 6-atom fcc shell, which in this case would contribute to the energy gain (6×6.9 eV), is compensated by the presence of a 12-atom shell, gaining 12×3.4 eV. The definite energy gain of hcp with respect to fcc is given by the 2-atom shell.

I have thus shown a practical example of non-tranferibility of an interatomic potential: the pair interaction energy term is suitable only for describing atoms pertaining to shells for the structure the potential is fitted to. This mismatch can be the cause of inaccurate dynamical simulation for extended dislocation cores, which can be corrected by the usage of QM/MM simulation as discussed in Section 5.6.

3.6 Generalised Stacking Fault Energy Curve

Consider a general (lmn) plane in a crystal. Let us cut the crystal above it, and shift the upper part by a translation vector $\mathbf{t}$ orthogonal to the $[lmn]$ direction. A system with a surplus energy per unit area $\gamma(\mathbf{t})$ is created. As the vector spans the unit cell, an energy surface is generated. It takes the name of generalised stacking fault (GSF) surface. The procedure can be extended by translating along multiple planes. A simple example of a translation vector along the $[\bar{1}2\bar{1}]$ direction for the (111) family of planes in a fcc crystal is shown in Figure 3.7

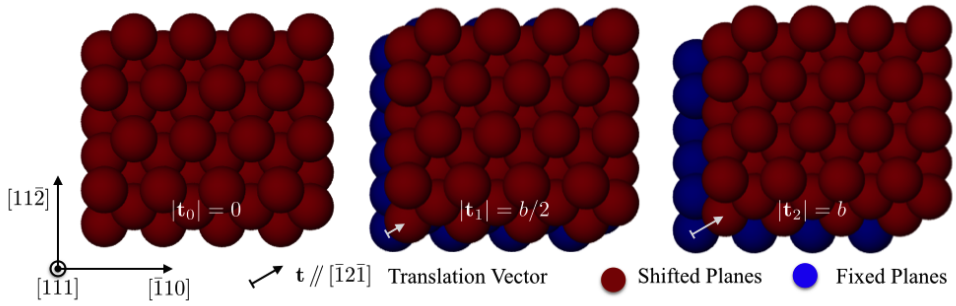

Figure 3.7: Translation vector along the $[\bar{1}2\bar{1}]$ direction for the (111) family of planes in a fcc crystal. b is the n.n. distance.

The GSF energy curve is crucial for understanding the properties of solids under deformation. It is directly used in the Peierls-Nabarro (PN) continuum model [126; 127], which is aiming at the description of a finite dislocation core, opposed to the singularity associated with the Volterra model [153]. Restoring stresses, evaluated as the gradient of the GSF energy, enhance this model, giving it a multiscale flavour. In the context of atomistic simulations, the study of the GSF surface provides insight on deformation processes. The least unfavourable maximum of the curve, known as the unstable stacking fault (USF) energy, gives the energetic cost for nucleating a dislocation, and it

is usually compared with the surface energies in order to define the ductility of a solid [154]. Another accessible quantity is the twinnability, which describes the likelihood of a material to undergo deformation twinning (as opposed to slip) under external loading [155] This is a typical phenomenon in nanowires and in nano crystalline materials [156]. Within the context of QM/MM simulations of dislocations in nickel, a close match between the calculated GSF energy surface using the MM and the QM method is important, as the distance between Shockley Partials (SP) is inversely proportional to the intrinsic stacking fault (ISF) energy (one of the minima of the GSF surface) [29]. A significant mismatch between the two values can create instability at the boundaries of the QM region. In this Section, I will analyse the GSF energy profile in γ and in γ', comparing EAM and *ab initio* data and discussing the role of chemical impurities.

Intrinsic and Extrinsic stacking Fault

Using the standard labelling A, B, C for {111} layers, the regular stacking sequence in fcc crystals is ABCABCABC. An intrinsic stacking fault (ISF) is defined as the defect created by removing one layer. It corresponds to a shift of $\mathbf{b}_p = \frac{a}{6}[11\bar{2}]$, where a is the lattice parameter of the elementary cell, and the produced stacking is ABCA|CABCA, where the vertical bar denotes the defect. The local symmetry of the atoms neighbouring the fault is the same as in hcp crystals (ABAB), and the periodicity of the crystal is disrupted. The translation $\mathbf{b}_p$ is the Burgers vector of a SP dislocation.

An extrinsic stacking fault (ESF) is similarly defined as the defect created by adding a {111} layer to a fcc crystal, or equivalently by applying a translation $\mathbf{b}_p$ to two consecutive planes. The resulting stacking ABCA|C|BCA corresponds to a double hexagonal close packed structure, and the original periodicity of the fcc crystal along {111} is disrupted. An equivalent translation of a third layer will restore it, creating a twin boundary ABCACBABC, in which the second A layer is the mirror plane.

Models for both ISF and ESF are shown in Figure 3.8.

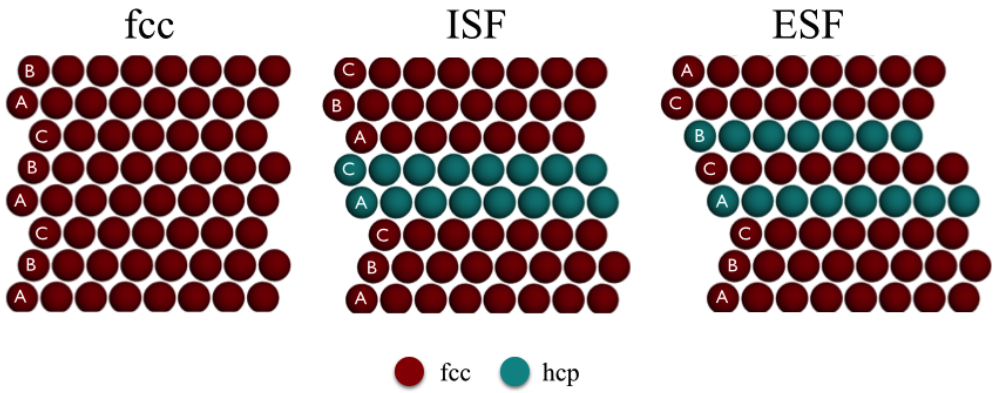

Figure 3.8: Models for fcc crystals including an ISF or an ESF.

Translation vectors $-\mathbf{b}_p$ or $2\mathbf{b}_p$ create a defect known as a run-on stacking fault ($ABCA|ABCAB$), which is energetically unfavourable due to two A layers neighbouring each other. Shifting along the close packed direction $[\bar{1}10]$ does not produce minima for the GSF energy profile, and only its projection onto the $[11\bar{2}]$ direction is studied. In order to perform this, a model system is constructed with the z direction perpendicular to the [111] crystal direction. A tetragonal lattice is used, with x and y perpendicular to $[\bar{1}10]$ and $[11\bar{2}]$ respectively. The system is replicated 6 times along z, creating a supercell with 18 (111) layers. Since the translation of the upper half of the structure will disrupt periodicity along z creating a run-on SF in addition to the ISF, a 15 Å thick vacuum region is introduced along z. The length of the slab is about 32 Å, sufficient to minimise the coupling between the external surfaces and the central atoms, where the SF is generated. A schematic view of the system is offered in Figure 3.9.

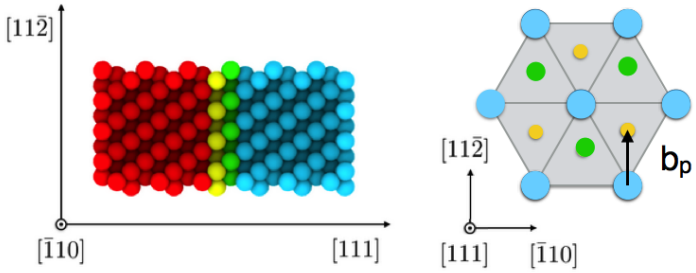

Figure 3.9: Top (schematic) and side view of the model system used for calculating the GSF energy surface in the γ phase. The translation vector $\mathbf{b}_p$, corresponding to an ISF, is indicated.

The ISF surface is generated by translating the atoms in the upper half of the slab (coloured green and blue in Figure 3.9) along the [11$\bar{2}$] direction. The shift is applied in a series of steps of length 0.24 Å, one sixth of the $\mathbf{b}_p$, so that an ISF is obtained after six steps and the run-on SF after twelve. The ESF is similarly generated, starting from the ISF structure. The atomic positions are fixed for both layers neighbouring the ISF (coloured yellow and the green in Figure 3.9), while the upper (blue) part is translated. Each configuration is relaxed with the FIRE algorithm with a force tolerance of 0.05 eV/Å, constraining atomic positions to change only along z. The parameters for DFT calculations are the same specified in Section 3.1, using a $16 \times 8 \times 1$ MP mesh for BZ sampling. The resulting portions of GSF energy curve are displayed in Figure 3.10, and the values of the extrema reported in Table 3.8.

The agreement between DFT calculations and the IP is very good for the curves between fcc stacking and ISF, and between ISF and ESF, meaning that the EAM is able to describe equilibrium configuration with great accuracy. This is an expected result, as the IP has been fitted to the energy difference between fcc-Ni and hcp-Ni, which would give the ISF energy.

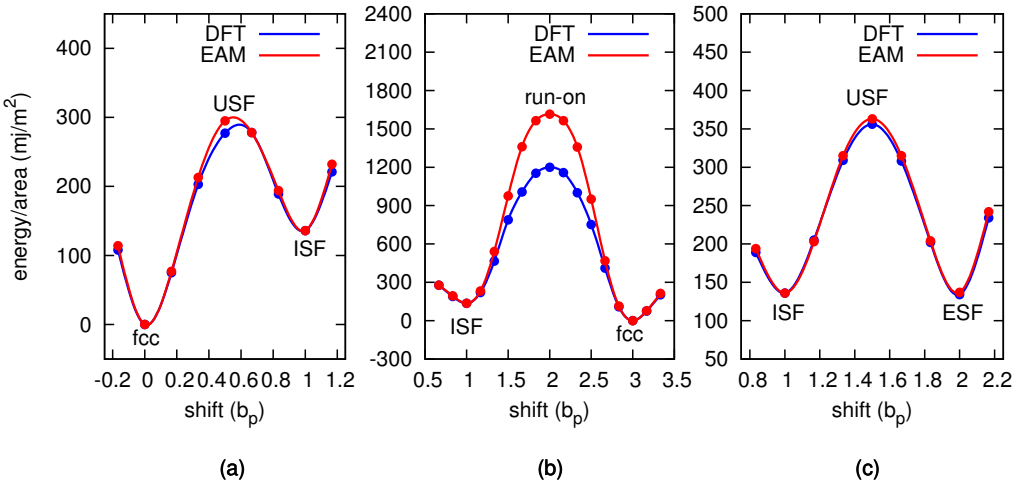

Figure 3.10: Portions of the GSF energy curve for the γ phase. The path from perfect fcc stacking to ISF is shown in (a). From this configuration, the curve proceeds towards a run-on in SF (b) and to an ESF in (c).

On the other hand, the GSF energy profile leading to a run-on stacking fault is overestimated with respect to DFT. This is not to be considered a major flaw of the potential, as this configuration is very unfavourable and it is never encountered during practical MD simulations. It is instead a warning, indicating that the potential is prone to failure when atomic configurations are far from equilibrium, and that EAM forces must be carefully checked against DFT reference calculations. The obtained result of about 140 mj/m^2 for ISF and ESF energies are in good agreement with literature [157].

	ϵ_{ISF}(mj/m^2)	ϵ_{USF}(mj/m^2)	ϵ_{run}(mj/m^2)	ϵ_{ESF}(mj/m^2)
DFT	136	278	1200	134
EAM	136	295	1615	137

Table 3.8: Comparison between DFT and EAM for the extrema of the GSF energy curve in the γ phase.

GSF Energy Surface in the γ' Phase

The GSF energy surface in γ' presents similarities with respect to the previous case, and is more complex because of the presence of a second atomic species. There are two different geometries that would correspond to an ISF in γ. In the first case, known as a complex stacking fault (CSF), all Al atoms along the fault are nearest neighbours. In the second case the distances between nearest neighbours atoms of different species are preserved. This configuration is called superlattice intrinsic stacking fault (SISF). The translation vectors for these two configurations are respectively $\mathbf{b}_p$ and $-2\mathbf{b}_p$.

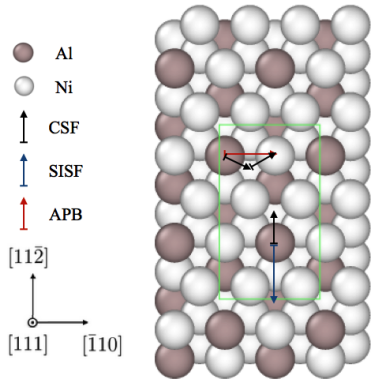

Figure 3.11: Translation vector corresponding to CSF (black), SISF (blue) and APB (red) on a $\{111\}$ γ' plane. The unitary cell is indicated in green.

Another point of interest of the GSF energy profile is the antiphase boundary (APB). Within this geometry, the stacking sequence of fcc crystals is preserved, but Al atoms are nearest neighbours on the plane along the fault. The associated translation vector is $\mathbf{b} = \frac{a}{2}[110]$, but the minimum energy path is not along the [110] crystal direction. The vector $\mathbf{b}$ can be written as the sum of two translation vectors corresponding to CSF geometries, e.g. $\mathbf{b}_p^{(1)} = \frac{a}{6}[211]$ and $\mathbf{b}_p^{(2)} = \frac{a}{6}[12\bar{1}]$, and the MEP follows their directions. This explains the structure of $\langle 112\rangle\{111\}$ superdislocation cores in γ', dissociated into two $\frac{a}{2}\langle 110\rangle\{111\}$ dislocations, separated by an APB.

Similarly to the γ phase, these dislocations are dissociated into SPs, separated by a CSF. The translation vectors for CSF, SISF and APB are indicated in Figure 3.11, respectively with black, blue and red arrows. The GSF curve can be evaluated using the same procedure described above, using both DFT and EAM. A denser grid of translations (one tenth of $\mathbf{b}_p$ each) is used to observe with improved resolution the extrema of the energy profile. The calculated values are reported in Table 3.9, and the path leading to an APB passing through CSFs is displayed is Figure 3.12, together with the equivalent curve for the γ phase (dashed line).

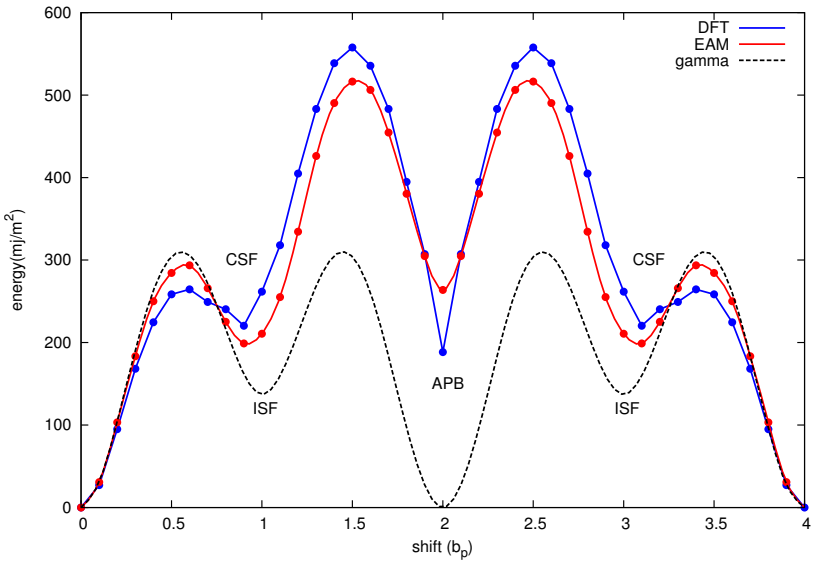

Figure 3.12: GSF energy surfaces for the γ' phase relative to translations for a single plane from DFT and EAM calculations. The equivalent curve for γ is plotted for comparison (dashed line).

The first USF energy γ_{us1} is very similar to the equivalent one in γ, but the CSF energy is higher than the ISF because the Al atoms along the fault are nearest neighbours. A good match between DFT and EAM is observed for this portion of the GSF energy curve. The unstable stacking fault energy γ_{us2}, related to the APB, is much larger with respect to the previous case.

This large barrier prevents single γ-channel dislocations from gliding into the precipitate. A disagreement between the interatomic potential and DFT on the predicted value for the APB energy is observed, already reported in Reference [5]. The APB energy obtained by means of first-principle calculations is fully compatible with the one reported in Reference [158].

GSFE mj/m^2	ϵ_{CSF}	ϵ_{US1}	ϵ_{APB}	ϵ_{US2}	ϵ_{SISF}
DFT	220	264	188	557	62
EAM	213	308	277	541	40

Table 3.9: Comparison between DFT and EAM for the extrema of the GSF energy curve in the γ' phase.

As a consequence, the EAM potential is expected to underestimate the distance between super-partial dislocations in γ'. This is not expected to be an issue, as in this work only dislocation in the γ channel and at the interface are studied, and in the second case the relevant value of the GSF curve is the CSF, for which the prediction of the IP is accurate.

Effect of impurities on GSF energies

In the previous subsections the ability of the EAM potential to reproduce accurate GSF energies was tested. Here this analysis is extended to Ni-based matrices containing chemical impurities. A $2 \times 2 \times 1$ supercell of the model system for γ is used, so that the impurities atoms are not nearest neighbours. With this setting, each (111) layer contains 8 atoms. In the first set of calculations, the GSF energy surface is evaluated for Al impurities, and results from DFT and from the IP potential are compared for different Al concentrations and configurations (Figure 3.13).

The simplest case of an isolated Al impurity, corresponds to an Al percentage of 12.5% in the single layer and of 0.7% in the whole crystal, is presented in panel (a). The calculated GSF energy curve has the same shape as in pure γ (Fig. 3.10). The chemical impurity lowers the values for both

the ISF and USF energies (cf. Table 3.10). As a direct consequence, the theoretical equilibrium distance between SP is increased. The agreement between DFT and EAM in evaluating the GSF energy profile is satisfactory.

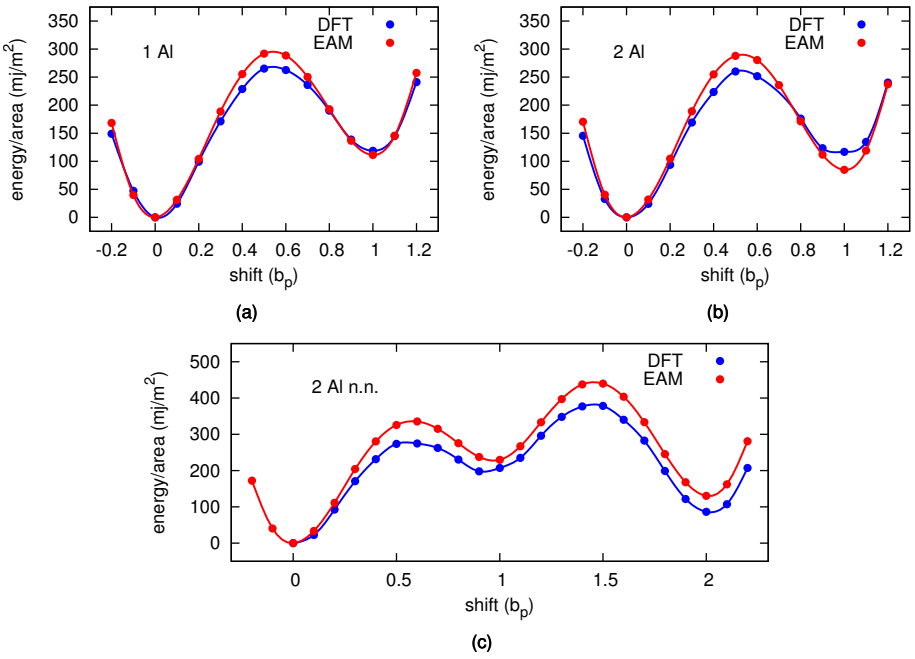

Figure 3.13: GSF energy curve for model systems of the γ phase including Al impurity atoms: comparison between EAM and DFT results for (a) an isolated impurity, (b) Al rich (25%) layer and (c) two Al impurities that become nearest neighbours upon shifting.

Adding a second chemical impurity to the matrix can have different effects: if the distance between atoms is preserved by the shift, i.e. if they belong to the same (111) layer, the ESF energy is proportional to the inverse of the concentration of impurity atoms. This is reported in Reference [58] for a number of different chemical impurities in the γ matrix. Results of calculations with 25% Al concentration in a single layer are displayed in Figure 3.13 (c).

The values for the USF and ESF energies, reported in Table 3.10, are lower than the previous set of calculations, confirming the trend. A less good agreement between simulation methods is observed, as the EAM potential overestimates the USF and underestimates the ESF energy, effectively predicting higher barriers to dislocation gliding.

GSFE (mj/m^2)					
system	calculator	USF	ISF	USF2	APB
γ Al1	EAM	292	111	-	-
γ Al1	DFT	265	119	-	-
γ Re1	DFT	282	101	-	-
γ Al2	EAM	287	85	-	-
γ Al2	DFT	260	117	-	-
γ Al2 n.n.	EAM	335	230	439	130
γ Al2 n.n.	DFT	274	197	378	86
γ Re2 n.n.	DFT	337	140	359	86

Table 3.10: Effect of Re and Al impurities of extrema of the GSF energy surface in the γ phase. Comparison between EAM and DFT results, and between different pair configurations for the chemical impurities.

When chemical impurities are located in neighbouring (110) layers, the applied shift will modify the relative distance between defects, and energetically unfavourable configurations can be obtained, forming obstacles and pinning sites for dislocation glide. The resulting GSF energy profile is consequently affected, with higher values for the USF and ISF energies. The previously adopted curve can be continued along the same path used in the case of γ', so that a second minimum, corresponding to an APB, is encountered. Results from this set of simulations are presented in Figure 3.13 (c). The values for the extrema are lower with respect to the the case of γ', but high enough to cause dislocation pinning, as demonstrated in Reference [159] by means of MD simulations. Only qualitative agreement with QM data is found, as the IP is overestimating a large part of the profile.

The same analysis is repeated for systems including rhenium impurity atoms, using the same settings for the DFT calculations. Results for the isolated defect are reported in Figure 3.14 (a).

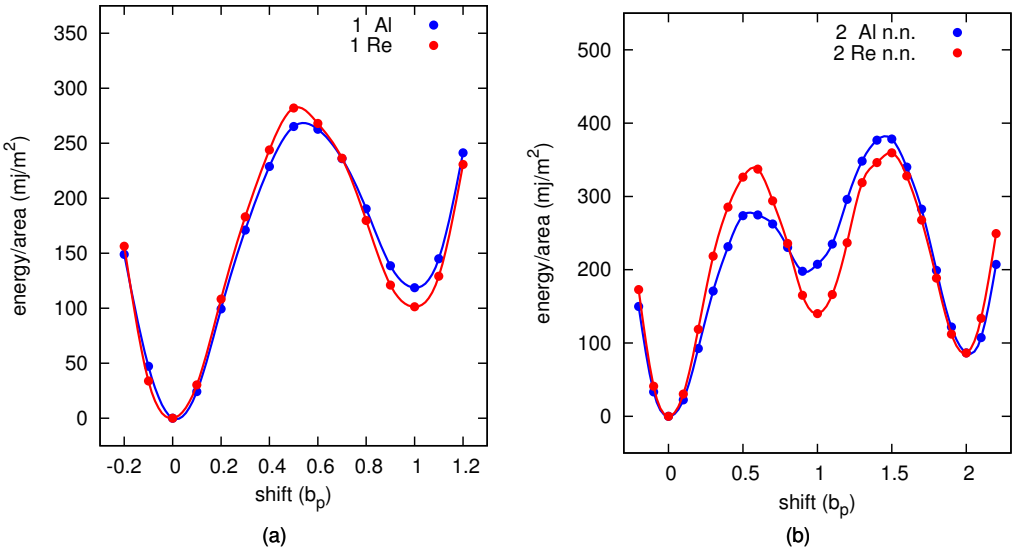

Figure 3.14: GSF energy curve for model systems of the γ phase including Re or Al impurity atoms: DFT for (a) an isolated impurity and (b) two impurities that become neighbours upon shifting.

The curve for rhenium is similar to the one for Al, with the only difference of having a lower ISF and a higher USF energy. This is consistent with the *ab initio* calculations performed in Reference [58] where Re, together with W and other heavy atoms, is shown to be one of the atomic species that have the larger effect on stacking fault energies. The extended GSF energy curve is then computed (Figure 3.14 (b)) for a system including impurity atoms in adjacent (111) layers. In this case, the first USF energy peak is as large as the second, and the ISF is further reduced with respect to the previous case. This means that both the SP dislocations face obstacles to glide.

3.7 Summary

A selection of quantum and classical simulations has been presented in this Chapter, with the aim of characterising energetic properties of nickel alloys and verifying the accuracy of the EAM interatomic potential. The latter is proven to be remarkably accurate in reproducing a large number of properties for γ and γ' model systems, including elastic constants and formation and migration energies for vacancies. Deviation from *ab initio* results is observed for some systems, as the potential has a limited chemical transferability. The examples of an isolated Al chemical impurity in the γ phase and of the elastic response of hcp nickel are reported. An underestimation for the expansion coefficient is also observed, due to the lack of a beyond-harmonic approximation for thermal effects. The GSF energy surfaces are correctly reproduced, despite a deviation from DFT for some configurations such as the minimum corresponding to the APB in γ'.

First-principle calculations are used for characterising rhenium, tungsten and Aluminium impurities in nickel alloys. The segregation of heavy atoms (Re, W) in the γ phase is studied, finding excellent agreement with experiments and with published *ab initio* data. Finally, the effect on the GSF energy profile of the abundance of impurities and of their distribution is explored. The curve is found to have a different shape in the case of Re and Al substitutional atoms. Whilst this certainly affects dislocation glide in the matrix, it can not be interpreted as the cause of the rhenium effect, as this feature would not be suppressed at low temperatures.

CHAPTER 4

Dislocations in fcc Materials

4.1 Introduction

This Chapter is devoted to the study of dislocations in Nickel alloys using the classical EAM potential developed in Reference [5]. In Section 4.2 basic concepts of the theory of dislocation in fcc crystals are outlined, focussing on their dissociation into Shockley partials (SP). In Section 4.3 linear isotropic elasticity theory is shown to give an analytic formula for the elastic energy of a dislocation. This describes the long-range interaction, and is not valid within a small region centred at the dislocation core. The latter contribution, purely due to local bond rearrangement, is calculated. This Section includes a discussion on the boundary conditions used for atomistic descriptions of systems including dislocations. In Section 4.4 two methods are presented for calculating the deformation tensor in order to locate the dislocation core. This leads to the identification of the Nye tensor, in Section 4.5, as the most robust method for locating and characterising dislocations. Molecular Dynamics simulations are used in Section 4.6 for measuring glide velocities in γ as a function of the temperature of the system and the applied shear stress. Finally, in Section 4.7, constant strain simulations are used to study the process of dislocation pinning at the γ/γ' interface.

4.2 Dislocations in fcc metals

The material properties most relevant to plastic deformation are related to the mobility of dislocations, and to their interactions with other defects. The most useful definition of a dislocation is given in terms of the Burgers vector. Consider an atom in a dislocated crystal, outside the core dislocation region. A closed loop, known as the Burgers circuit, can be constructed by nearest neighbours hopping, as in Figure 4.1. If the same path is followed in a perfect crystal, and the circuit is not closed, than the Burgers circuit encloses one or more dislocations, and the vector required to complete the circuit is called the Burgers vector $\mathbf{b}$. For perfect dislocations, it is one of the translation vectors of the lattice. The dislocation line ξ is the unit vector normal the Burgers circuit. The character of a dislocation is defined by the relation between $\mathbf{b}$ and ξ: the dislocation is identified as edge (screw) if the Burgers vector is orthogonal (parallel) to the line vector.

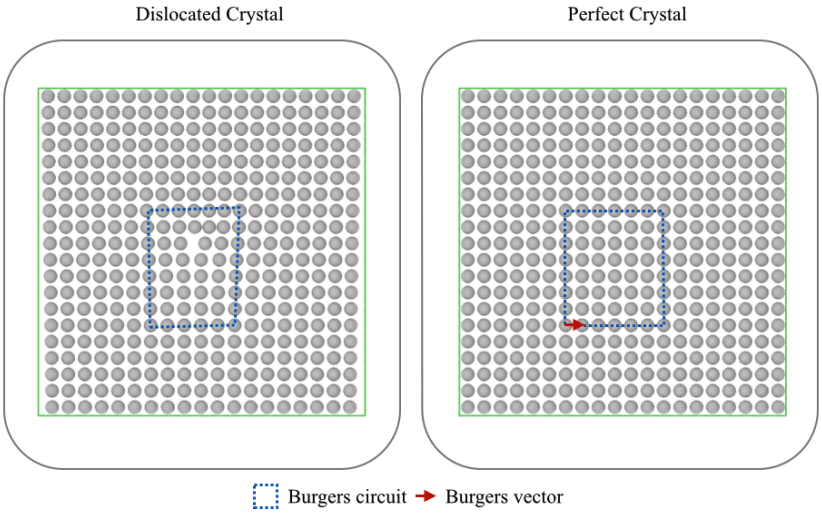

Figure 4.1: Burgers circuit and Burgers vector for an edge dislocation in a simple cubic crystal.

Dislocations can have mixed character. In this case it is possible to decompose the Burgers vector into a screw and an edge component. According to the Frank energy criterion [29] only dislocation with the shortest Burgers vector are stable. This means that the only active slip systems are the ones associated with the close packed family of planes. In fcc materials, this is the $\{111\}$, and perfect dislocations have Burgers vector $\mathbf{b} = \frac{1}{2}[110]$, in units of the lattice parameter of the cell. The notation $\frac{1}{2}\langle 110\rangle\{111\}$ is used, in which the slip plane is also indicated. Perfect dislocations in fcc materials are usually dissociated into two Shockley partials (SPs), according to the reaction [29]

$$\frac{1}{2}[110] \longrightarrow \frac{1}{6}[211] + \frac{1}{6}[12\bar{1}] \tag{4.1}$$

and separated by a stacking fault. The energetic cost for creating such a defect compensates the elastic repulsion between SP dislocations, leading to the equilibrium distance

$$d_{\mathrm{eq}} = \frac{\mu}{2\pi\gamma_{\mathrm{sf}}}\left\{(\mathbf{b}_1 \cdot \xi)(\mathbf{b}_2 \cdot \xi) + \frac{(\mathbf{b}_1 \times \xi)(\mathbf{b}_2 \times \xi)}{1-\nu}\right\} \tag{4.2}$$

where $\mathbf{b}_1, \mathbf{b}_2$ are the Burgers vector for the SP, ξ the common line direction, μ the shear modulus, ν the Poisson ratio, and γ_{sf} the ISF energy. This formula does not accurately describe the equilibrium distance in an atomistic models, as in the continuum treatment the size of dislocation cores is assumed to be negligible. The dislocation dissociation into SPs has a direct influence on dislocation motion. Screw dislocations are constrained to glide in the plane containing the stacking fault, and cross-slip to a different plane is a rare event as it first requires dislocation constriction, as described by the Friedel-Escaig model [29].

4.3 Long Range Elasticity and Core Region

The Elastic Energy

Classical elasticity theory allows the deformation induced by a dislocation to be treated as a continuous quantity far from the core region. The displacement field for a screw dislocation in given by [29]:

$$u_z = \frac{b}{2\pi} \arctan\left(\frac{y}{x}\right) \tag{4.3}$$

where the dislocation line is parallel to z and b is the modulus of the Burgers vector. This elastic displacement is over imposed to an atomistic system is Figure 4.2. The $\frac{a}{2}\langle 110\rangle\{111\}$ screw dislocation is placed at the centre of the cell.

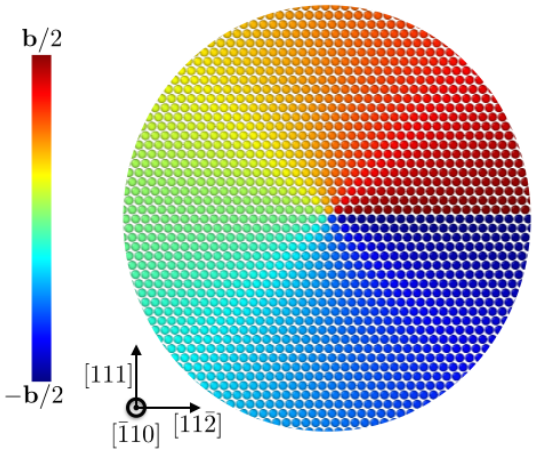

Figure 4.2: Elastic displacement for a screw dislocation in the γ phase.

For an edge dislocation, the displacement in the (x, y) plane is:

$$\mathbf{u}_{xy} = \frac{b}{2\pi}\left[\arctan\left(\frac{y}{x}\right)\hat{\mathbf{x}} + \frac{(1-2\nu)}{4(1-\nu)}\hat{\mathbf{y}} + \frac{xy}{2(1-\nu)(x^2+y^2)}(\hat{\mathbf{x}}+\hat{\mathbf{y}})\right] \tag{4.4}$$

From the expressions (4.3), (4.4) the strain is obtained as $\frac{1}{2}(\partial_j u_i + \partial_i u_j)$ and the elastic energy as

$$U = \frac{1}{2} \sum_{ijkl} C_{ijkl} \epsilon_{ij} \epsilon_{kl} \tag{4.5}$$

where C_{ijkl} are the elastic constants. The integration of (4.5) over a cylinder coaxial with ξ leads to the expressions [29] for the energy stored by the elastic strain of respectively a screw and an edge dislocation:

$$\frac{E_{\mathrm{s}}}{\ell} = \frac{\mu b^2}{4\pi} \log\left(\frac{R}{r}\right) \quad , \quad E_{\mathrm{e}} = \frac{E_{\mathrm{s}}}{1-\nu} \tag{4.6}$$

where ℓ is the length of the dislocation line, R and r the radii of the cylinder and of the core region respectively. Linear elasticity is not applicable within the latter, and an extra energy term is added to account for the local bonding rearrangement, quantifiable only by means of atomistic simulations.

Boundary Conditions

In performing atomistic simulations for dislocation properties, it is important to understand the periodicity of the simulated system. A system can be fully (3D) periodic only if

$$\sum_{i=1}^{N_d} \mathbf{b}_i = 0 \tag{4.7}$$

where N_d is the total number of dislocations in the system and $\mathbf{b}_i$ the Burgers vector of the i-th one. In the case of a single screw dislocation, it is clear from the the elastic displacement (4.3) and from Figure 4.3 that the system is periodic only along the dislocation line. Geometrical optimisation of such a system would proceed by nucleation of dislocations at the boundary, in order to restore the periodicity of the system by satisfying the condition (4.7).

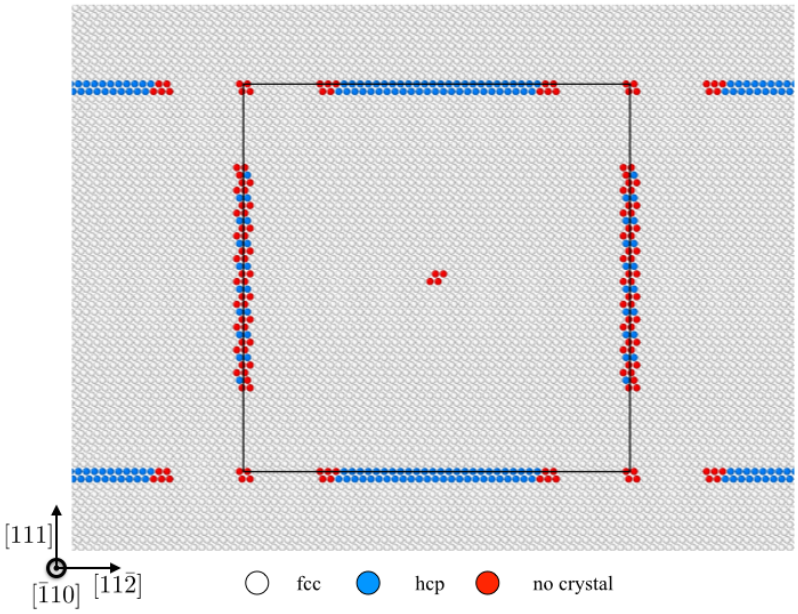

Figure 4.3: Unrelaxed screw dislocation in the γ phase. The lattice is indicated with a black box. The system does not have the periodicity of the bulk, as indicated by the atoms at the boundary of the cell which deviate from the fcc structure.

The best solution for obtaining a periodic system, proposed for the first time in Reference [160] for the *ab initio* simulation of a 90° dislocation in Silicon, is to set a quadrupole of dislocations with alternating sign of the Burgers vector, ensuring by symmetry vanishing forces on the cores, and further limiting finite-size effects. A smaller periodic system containing only a dislocation dipole, necessary for satisfying Equation (4.7), can be extracted from the latter, using the monoclinic lattice indicated in green in Figure 4.4.

It is sometimes desirable to have open boundary conditions (obc), so that a force can be applied to an open surface, allowing constant stress simulations of the system. This approach is useful e.g. for calculating glide velocities, and widely used in the literature [6; 121; 159].

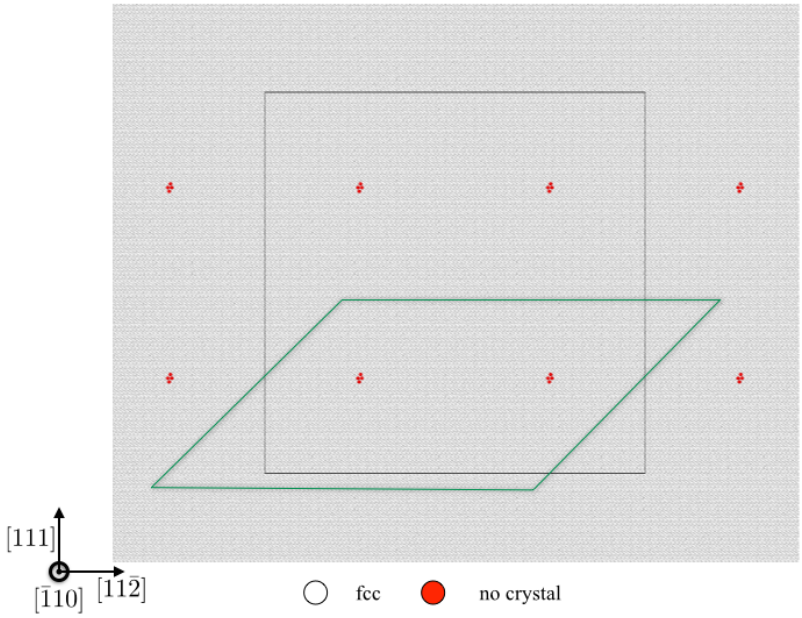

Figure 4.4: Unrelaxed quadrupole of screw dislocations (opposite sign of the Burgers vector) in the γ phase. The system is has the full periodicity of the bulk fcc structure.

In other cases a velocity gradient is applied, together with a shear strain, to the atoms at the boundaries of the cell, in order to simulate conditions that would allow for the nucleation of dislocations [20]. It is possible to restore the periodicity along the direction of motion of a dislocation [161]. This is desirable when calculating the glide velocity, as long simulation times are required before reaching the steady state, especially when thermal effects are dominating with respect to stress. In the case of a screw, this is realised by removing a complete (112) layer and rescaling the lattice accordingly. This corresponds to the application of forces balancing the lattice rotation associated with dislocations. Larger cells are required to minimise its influence on dislocation properties. Size convergence tests for this class of simulations are presented in Section 4.6. Similar tests are also performed in Reference [161].

Core Energy

An EAM potential can be used to evaluate the core region contribution to the energy of the system. The crystal is oriented so that the z axis is parallel to the line direction $[\bar{1}10]$. The x, y directions are chosen to be respectively along $[11\bar{2}]$ and $[111]$. A $N_x \times N_y \times 1$ supercell is created, for $N_y \approx N_z\sqrt{2}$ so that the length of the lattice vectors along is the same along x and y (cf. Table 4.1). A quadrupole of screw dislocations is introduced by applying the elastic displacements (4.3), and the system is optimised using a force convergence threshold of 1 meV/Å. The total energy for the relaxed structure is calculated and compared to bulk system of the same number of atoms.

N_x	17	24	33	41
N_y	12	17	24	29
d (nm)	3.66	5.17	7.11	8.84

Table 4.1: Distances between n.n. dislocations of opposite Burgers vector sign within $N_x \times N_y$ γ-Ni supercells.

The elastic energy for a system including a quadrupole of screw dislocations is given by

$$E = 4E_c(r_c) + \frac{kb^3}{\pi}\left[\log\left(\frac{d}{r_c}\right) + A\left(\frac{d_1}{d_2}\right)\right] \tag{4.8}$$

where E_c is the core energy, r_c the radius of the core region. The function $A\left(\frac{d_1}{d_2}\right)$ takes into account the elastic interaction between dislocation quadrupoles. Since in this set of simulations $d_1 \approx d_2 = d$, is just a constant energy shift, which can be evaluated numerically by means of an Ewald summation, as in Reference [162]. Linear fitting of equation (4.8) using E_c as a free parameter returns 0.657 eV as an estimate for the core energy per Burgers vector. This is consistent with the value of 0.54 eV obtained in Reference [163] using the Sutton-Chen potential [164].

4.4 Calculation of the Deformation Tensor

The Von Mises Strain Invariant

The Von Mises invariant is a simple recipe for evaluating the strain tensor in cubic materials. Consider an atoms i within a crystal with cubic symmetry and indicate with $\mathbf{q}_{ij} = \mathbf{r}_j - \mathbf{r}_i$, $j = 1, 2, \cdots, N$, where N is the coordination number, the difference vector with respect to its neighbours. The quantity

$$M_i = \sum_{j=1}^{N} \mathbf{q}_{ij} \mathbf{q}_{ij}^T \tag{4.9}$$

can be shown to be proportional to the identity. An affine transformation J changes the coordinates $\mathbf{q}_{ij} \to \mathbf{q}'_{ij} = J\mathbf{q}_{ij}$, and (4.9) accordingly:

$$M'_i = \sum_{j=1}^{N} \mathbf{q}'_{ij} \mathbf{q}'^T_{ij} = J\mathbf{q}_{ij}\mathbf{q}_{ij}^T J^T = \alpha_0 J J^T \tag{4.10}$$

where α_0 is a constant depending on the crystal symmetry. This relation is valid only if the number of neighbours is conserved by the transformation. The local atom-resolved Lagrangian strain, defined as

$$\epsilon = \frac{1}{2}(J^T J - \mathbb{1}) \tag{4.11}$$

is therefore easily evaluated. This scheme is easy to implement, but it has a drawback arising from the requirement of conservation atoms coordination. This number fluctuates significantly during high-temperature MD simulations, and neighbouring shells at the dislocation core are distorted. This can be addressed by recalculating the connectivity so that the neighbours are preserved, or by averaging atomic coordinates during MD simulations. There is no solution when the system includes a vacancy, as the initial assumption of M_i being proportional to the identity matrix is not valid.

This technique is used to study the strain field due to misfit dislocations at the γ/γ' IPB. The y direction is aligned with the normal to the [100] interface, and x, z are parallel to the [011] and [01$\bar{1}$] directions respectively. The unit cell is repeated along x N and $N-1$ times γ' respectively, where $Na_\gamma \approx (N-1)a_{\gamma'}$. The ideal value for N is found to be 70. Repetition of the unit cells along y is made so that cubic structures are created for both the phases. The resulting supercell size is $24.6 \times 49.2 \times 0.25$ nm^3. Geometry optimisation is performed with the IP using the conjugate gradient algorithm with a force convergence threshold of 10^{-2} eV/Å. The average shear component of the von Mises strain for the relaxed structure is displayed in Figure 4.5.

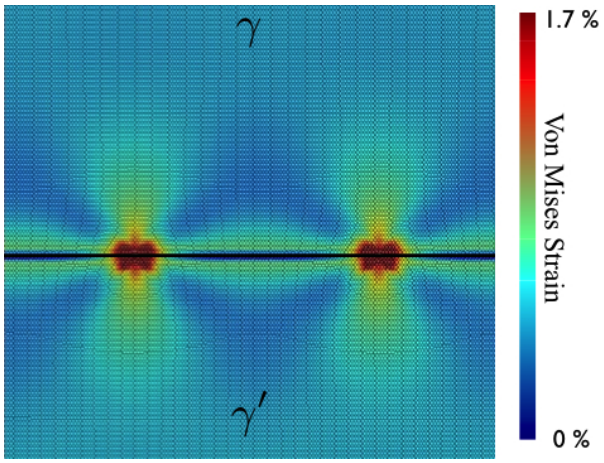

Figure 4.5: Von Mises strain for misfit dislocations at a sharp γ/γ' interface.

The maxima of the strain field are located in the core region, where the deviation from the perfect crystal is larger. The minima are encountered near this region, as the misfit dislocation relaxes the interfacial strain, thus creating a coherent interface. The strain monotonically increases with the distance from the defect, and its maximum is reached where the distance between dislocations is maximised.

The Correspondence Tensor

In this Section, a more robust method for evaluating the deformation tensor is presented. Its greater stability with respect to the Von Mises method arises from the fact that an average over neighbouring atom positions is performed, some of which can be disregarded without a loss of accuracy, given the high coordination numbers of fcc crystals. This allows for calculations of the deformation tensor around a vacant site, or for atoms pertaining to an intrinsic stacking fault (for which the correspondence with the perfect lattice is not unique). The method has been introduced in Reference [165], and later employed in Reference [166] for evaluation of the Nye tensor, following the same procedure reported here in Section 4.5.

A formal description is provided here for this quantity and for the numerical methods related to its calculation. Let us define a set of basis vectors $\mathbf{i}_\alpha$ for the perfect lattice and another set $\mathbf{e}_i$ for the dislocated one. Note the usage of Greek and Latin indexes for designating different lattices. In every point P of the lattice, a deformation tensor $\mathbf{F}(P)$ can be defined so that

$$\mathbf{e}_i = \sum_\alpha \mathbf{F}_i^\alpha \mathbf{i}_\alpha \quad \text{and} \quad \mathbf{i}_\alpha = \sum_i (\mathbf{F}^{(-1)})_\alpha^i \mathbf{e}_i \tag{4.12}$$

where the label P is dropped for simplicity. Let us now introduce a third reference system $\mathbf{g}_i$ in order to define a common reference frame, and denote the transformation matrices as $\mathbf{L}_i^\alpha = \mathbf{i}_i \mathbf{g}^\alpha$ and $(\mathbf{L}_a^{\prime)\ k}$. The relation between the two lattices can then be rewritten as

$$\mathbf{L} = \mathbf{L}'(\mathbf{F}^{-1})^T \tag{4.13}$$

The latter deformation tensor $(\mathbf{F}^{-1})^T$ is known as the correspondence tensor and it is usually indicated as $\mathbf{G}$. It is the transpose of the correspondence function originally defined in Reference [165].

Equation (4.13) can be directly solved in order to obtain the correspondence tensor, but the choice of a suitable basis set for atoms neighbouring a dislocation core is often complicated. The numerical algorithm used here for the evaluation of this tensor is instead based on an average over neighbouring atoms. Only atoms lying within a certain cutoff radius are selected. For each vector connecting the central atom to one of its neighbours, a corresponding vector is found in the perfect reference lattice by minimising the angular deviation. Note that this would not lead to unique solutions for fcc systems including stacking faults. Atoms presenting this kind of ambiguity are discarded. Once this problem is solved, the correspondence tensor $\mathbf{G}$ is constructed as

$$\mathbf{P} = \mathbf{Q} \cdot \mathbf{G} \tag{4.14}$$

where $\mathbf{P}$ and $\mathbf{Q}$ are $n_{\text{neighb}} \times 3$ matrices containing points in the perfect and in the dislocated lattice respectively. Note that Equation (4.14) is overdetermined, and the mean square solution has the form $\mathbf{G} = \mathbf{Q}^{\dagger}\mathbf{P}$ where

$$\mathbf{Q}^{\dagger} \equiv (\mathbf{Q}^T\mathbf{Q})^{-1}\mathbf{Q}^T \tag{4.15}$$

is the generalised inverse of $\mathbf{Q}$, also known as the Moore-Penrose matrix.

This method provides an atomically resolved deformation tensor. The stability of the method is given by the high coordination number in metallic structures. The region included within the shell of neighbours used for the evaluation of the deformation tensor corresponds to the 'point' to which continuum description refer. In this work, the calculation of the correspondence tensor is the first step towards the calculation of the Nye tensor, which allows for dynamical identification of the location of the QM region for multiscale atomistic simulation within the LOTF method.

4.5 The Nye tensor

Theoretical Description

The Nye tensor α_{ij}, originally introduced in Reference [167], is formally defined as the quantity relating the normal $\mathbf{l}$ to a Burgers circuit of unit area to the associated Burgers vector via the relation:

$$b_i = \sum_{ij} \alpha_{ij} l_j \tag{4.16}$$

The Nye tensor, originally defined within the frame of continuum dislocation theory, is now used for providing an atomic-resolved characterisation of dislocation cores, as shown in Reference [166]

A brief demonstration is given on how the Nye tensor can be calculated if the crystal deformation in known. Let us consider a Burgers circuit $\mathcal{C}'$ in a dislocated crystal. The circuit is made by lattice vectors $\Delta\mathbf{x}'$ such as:

$$0 = \sum_{\mathcal{C}'} \Delta\mathbf{x}' \tag{4.17}$$

If the relation is translated into a perfect reference lattice, the same summation along the path would define the Burgers vector

$$\mathbf{b} = -\sum_{\mathcal{C}} \Delta\mathbf{x} \tag{4.18}$$

The two crystals $\mathbf{x}$ and $\mathbf{x}'$ are related by the deformation tensor $\mathbf{G}$, so that Equation (4.18) can be recast, in the continuum limit, in the form:

$$\mathbf{b} = -\int_C d\mathbf{x} = -\int_{C'} d\mathbf{x}' \cdot \mathbf{G} \tag{4.19}$$

Application of Stokes' theorem to the line integral in (4.19), allow for a redefinition of the Burgers vector as

$$\mathbf{b} = -\int_{\mathcal{A}} dS\ \mathbf{n} \cdot \nabla \times \mathbf{G} \tag{4.20}$$

where $\mathcal{A}$ is the surface enclosed by the Burgers circuit and $\mathbf{n}$ its normal unitary vector. This equation can be directly compared with Equation (4.16), from which the following relation between the Nye tensor and the deformation tensor follows:

$$\alpha = \nabla \times \mathbf{G} \tag{4.21}$$

The Nye tensor can therefore be computed directly from the atomic positions of the crystal, and the Burgers vector is easily obtained through surface integration as in (4.20). Most of the components of the Nye tensor α_{ij} are vanishing (or they have a certain symmetry around the dislocation core so that the surface integral is zero), as not all the slip systems are observed in realistic materials. It is understood from Equation (4.16) that diagonal components correspond to screw dislocation (Burgers vector parallel to the normal to the circuit) and off-diagonal to edge dislocations (Burgers vector in the same plane as the circuit).

Evaluation of the Burgers Vector

The Nye tensor analysis is here applied to a selection of structures including perfect dislocations (screw, edge and 60° mixed $\frac{1}{2}\langle 110\rangle 111$) in γ-Ni. This allows the atoms pertaining to the dislocation core to be located, distinguishing them from the surrounding ones whose deformation is due to the stacking fault. The Burgers vector is evaluated from Equation (4.20), by interpolating relevant components of the Nye tensor on a fine grid. This analysis depends on the number of atoms included within the nearest neighbours cutoff radius, used for evaluating the deformation tensor, as in (4.13). Ambiguities on the

definition of the n.n. shell might arise while dealing with strongly deformed regions such as along a dislocation line.

Calculations are performed using supercells of nickel fcc large enough to accommodate the stress field of a dislocation. The orientation of the crystal depends on the character of the dislocation. Crystal and Burgers vector orientation for each of the three model systems are shown in Table 4.2. The dislocation line direction ξ is always chosen perpendicular to the z axis. With this convention, the only non-vanishing components of the Nye tensor α_{ij} are α_{33} and α_{31}. I will refer to them respectively as the screw and the edge component of the tensor. The length of the system along directions orthogonal to the dislocation line (xy plane) is about 130 Å. The cell is periodic along the line direction ξ by construction.

	$\hat{x}$	$\hat{y}$	$\hat{z}$	$\hat{b}$
screw	$[11\bar{2}]$	$[111]$	$[1\bar{1}0]$	$[1\bar{1}0]$
60° mixed	$[100]$	$[011]$	$[01\bar{1}]$	$[101]$
edge	$[\bar{1}10]$	$[111]$	$[11\bar{2}]$	$[\bar{1}10]$

$\hat{\xi} \equiv \hat{z}$ dislocation line direction

Table 4.2: Crystal and Burgers vector orientations for model systems of dislocation cores in the γ phase.

A dislocation of the selected character is introduced at the centre of the structure by imposing the elastic displacement field from continuum theory. Atoms with a relative distance smaller than 2 Å are then removed. This is never the case for screw dislocations, as the elastic displacement is along z, and therefore the projection of distances in the xy plane is preserved, and they are greater than 2 Å by construction. However, the removal of these atoms is particularly important in the case of edge dislocations, where they prevent the formation of symmetric Shockley partials. Open surfaces are then introduced at the boundaries in order to avoid the formation of dipoles or quadrupoles. The vacuum region is selected to be 15 Å thick (twice the potential cutoff radius r_{cut}), to avoid any interaction between periodic images.

Since the potential is radial, the original square is turned into a circle whose diameter has the same length of the side of the square. An external shell of atoms is kept fixed during the relaxation of the system, its thickness is chosen to be 15 Å in order to avoid interaction between the active region and the surfaces. A schematic view of the system is offered in Figure 4.6.

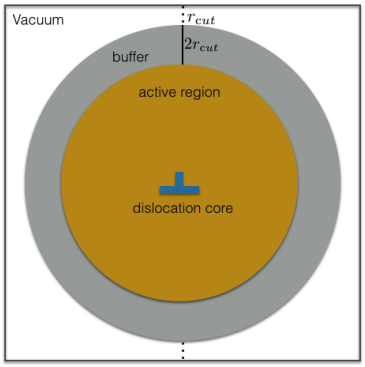

Figure 4.6: Schematic view of model used for simulating a dislocation.

The Burgers vector is characterised (screw or edge) and integrated by interpolation on a fine grid. Good convergence is obtained using a point every 0.05 Å. This analysis is then repeated after structural optimisation of the system (conjugate gradient algorithm, with a convergence threshold of 10^{-2} eV/Å). Results for both unrelaxed and relaxed configuration are displayed in the upper panels of Figure 4.7. The modulus of the full Burgers vector is underestimated in both cases whenever only true n.n. are considered for evaluating the deformation tensor. The correct value is recovered when all the atoms within 3.2 Å are included for the unrelaxed configurations. This is a mark of the strong deformation around core atoms, as no neighbour shell of the fcc geometry corresponds to this distance.

In the case of relaxed dislocation structures the full Burgers vector is obtained when interactions up to the second shell of neighbours are included. In the range 3.5–5.0 Å the integrated value presents oscillations as large as 20%, due to background noise from atoms not pertaining to the core region.

The correct value is obtained once again at 4.1 Å, values corresponding to the third shell of neighbours for the hcp structure. For neighbour cutoff distances greater than 5 Å the background noise becomes dominating.

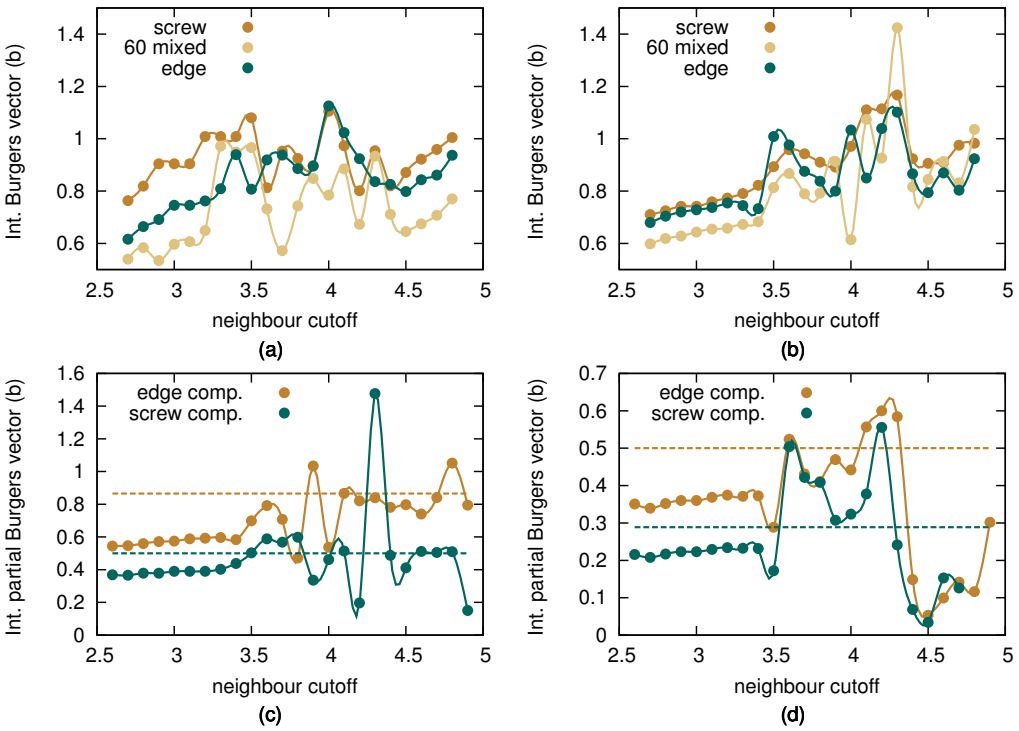

Figure 4.7: Burgers Vector, evaluated as the surface integral of relevant components of the Nye tensor as a function of the n.n. cutoff, for edge, screw and 60° mixed dislocations in the (a) unrelaxed and (b) relaxed configurations. Shockley partials characterisation for (c) edge and (d) 60° mixed dislocations.

Results are less accurate in the case of a mixed dislocations, as in this case the edge and the screw components are evaluated separately. Single SP are characterised in Figure 4.7 (c,d) for an edge and a 60° mixed dislocation respectively. Results are more accurate in the case of an edge dislocation, because of the larger distance between SP dislocations.

Visualisation of a Dislocation Core

The Nye tensor analysis can be used for visualising the distribution of surface Burgers vector density in the plane normal to the dislocation line. The major contribution ($\sim 70\%$) comes from only a few atoms, clustered in region of a few Angstroms radius, as shown in Figure 4.8 for a screw dislocation, thus identified as the core of a dislocation. This analysis can be used for locating the QM region, as discussed in Section 5.3.

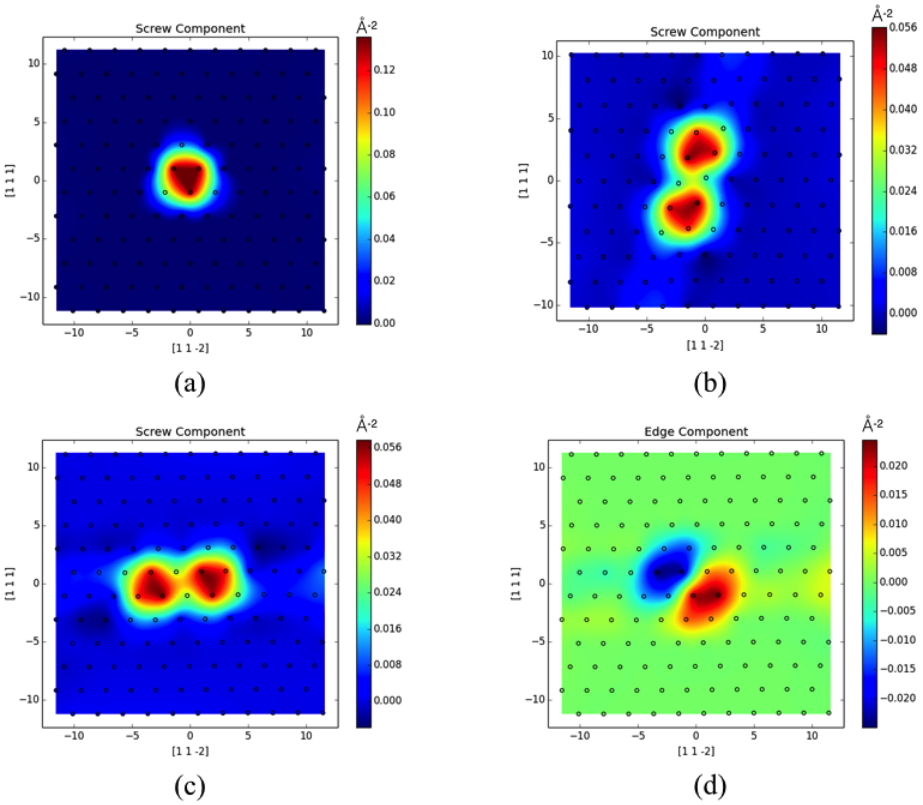

Figure 4.8: Nye tensor analysis for a screw dislocation. Distribution of Burgers vector surface density in a (110) layer. The screw component is displayed in panel (a) for an unrelaxed geometry, and in panel (b) and (c) for two equivalent extended dislocation cores. The edge component for the latter geometry is displayed in panel (d).

In panel (a) the system is displayed before the structural optimisation, so that only a single dislocation core can be observed. A cutoff of 3.3 Å is used for evaluating the deformation tensor. This value corresponds to the correct value for the Burgers vector as shown in Figure 4.7. Such a dislocation can dissociate into two equivalent (111) planes, both perpendicular to the dislocation direction. The screw component of the Nye tensor corresponding to these configurations is shown in panel (b) and in panel (c) of Figure 4.7. The edge components for Shockley partials is displayed in panel (d). They have opposite signs, and integration over the plane gives no contribution to the Burgers vector as expected. The same analysis is reported in Figure 4.9 for an edge and a 60° mixed dislocation. The Nye tensor is evaluated using a cutoff of 3.6 Å, corresponding to an accurate integrated Burgers vector for the edge dislocation and to a 10% deviation from the theoretical value for the mixed one. In the first case, displayed in panels (a) and (b), the two edge components are identical while the screw ones have opposite sign. In the second case the Shockley partials present different shape and character as the starting configuration has a mixed character. The first presents a large edge component, while the screw one is dominating in the second case, accordance with theory, which predicts screw components of $b/2$ and 0 and edge components of $b/2\sqrt{3}$ and $b/2\sqrt{3}$. There is a non-vanishing screw component for the second partial, which explains the overestimate for the screw component observed in Figure 4.7 (d).

The Nye tensor is proven to be sub-optimal for characterising mixed dislocations. In this work, this analysis is developed in order to track dislocation cores during QM/MM Molecular Dynamics simulations for QM region updating. It is therefore not crucial to obtain the exact value for the integrated Burgers vector, but to construct a robust algorithm capable of following dislocation cores as they glides. Out of these considerations, an ideal cutoff value for the evaluating the deformation tensor is smaller than 3 Å, so that the peaks and the oscillatory behaviour shown in Figure 4.7 are avoided.

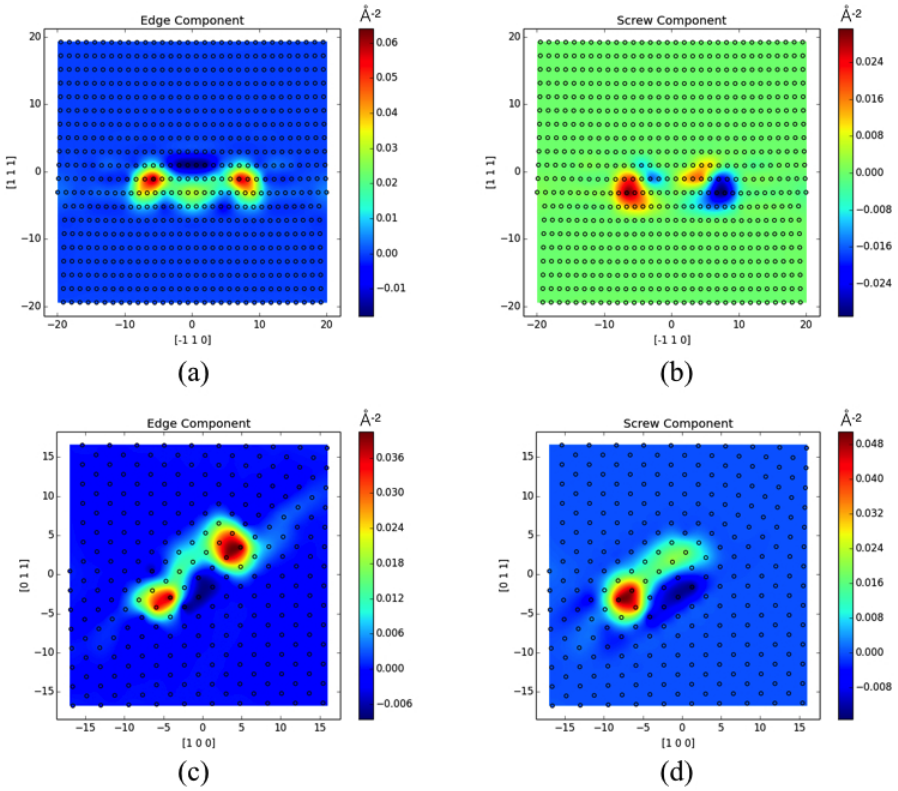

Figure 4.9: Nye tensor analysis for edge (a,b) and 60° mixed (c,d) dislocations. Screw (a,c) and edge (b,d) components of the Burgers vector density are displayed.

High Temperature Effects

The purpose of this section is to verify the robustness of the Nye tensor approach when thermal noise is included. An accurate dislocation tracking method would allow the usage of QM regions of minimal size, as discussed in 2.7, thus accelerating the overall LOTF calculation. This is tested using the model 4.6 for a screw dislocation, replicating the system along the line direction ξ to avoid self-interactions. The length of the lattice along ξ should be ideally at least twice the cutoff of the IP ($\sim$ 12 Å, corresponding to 10 (110) layers). On the other hand, increasing the length of the system along ξ corresponds to enlarging the QM region. This can be addressed by splitting the QM region into subdomains and taking advantage of massively parallel machines for QM calculation [168]. In this work, splitting occurs naturally because of the dissociation into SP dislocations. A further subdivision of each QM region is required for large systems, necessary e.g. for the study of dislocation defects such as jogs and kinks. This is not addressed here, and the future development of such a scheme will constitute a further step ahead towards QM/MM modelling of plasticity in metals.

The testing is performed by means of MD simulations, comparing systems of different width. The velocity of the atoms is rescaled to twice the target temperature, and the dynamics is then simulated for 5 ps. The Burgers vector is evaluated as the surface integral of the screw component of the Nye tensor every 0.2 ps, using a cutoff radius of 2.8 Å for deformation tensor evaluation and averaged over the (110) layers. This integral is found to be unstable for $L_\xi < 5$ Å. Values corresponding to systems with 8, 12 and 16 (110) laters (respectively 10, 15 and 20 Å length along ξ) are displayed in Figure 4.10. The amplitude of the oscillations for the integrated Burgers vector is inversely proportional to the length of the system along ξ. Large deviation from the ideal value ($\sim$ 80%) can still be observed whenever the system length along ξ is larger then twice the IP cutoff.

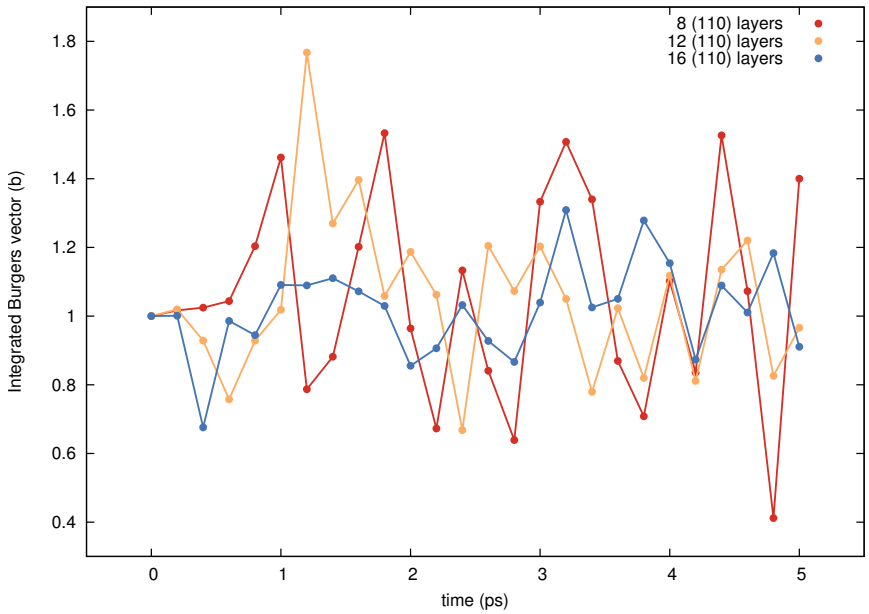

Figure 4.10: Integrated Burgers vector for a system including a screw dislocation during MD simulations at 1200 K. Different curves correspond to different length of the system along the dislocation line direction.

The validity of the Nye tensor method is debatable whenever temperature effects are introduced, as the atoms do not lie exactly on the same plane. Despite the low accuracy for the calculation of the Burgers vector, this algorithm is capable of tracking dislocations during a dynamics, as shown in Figure 4.11, where the relaxed geometry (a) is compared to configurations observed during the dynamics. The screw component of the Nye tensor is always maximised in a small region, identified with the dislocation core. This is true for a variety of cases observed during a classical MD, including SP further away from each other (b) and constriction (c). In panel (d) a cross-slip phenomenon is observed. In every case observed, the are of the dislocation core region is $\sqrt{(2)}b^2$ or smaller. This allow for a definition of a minimal QM region. The locality of the EAM force error for crystal defects is verified in Section 5.3.

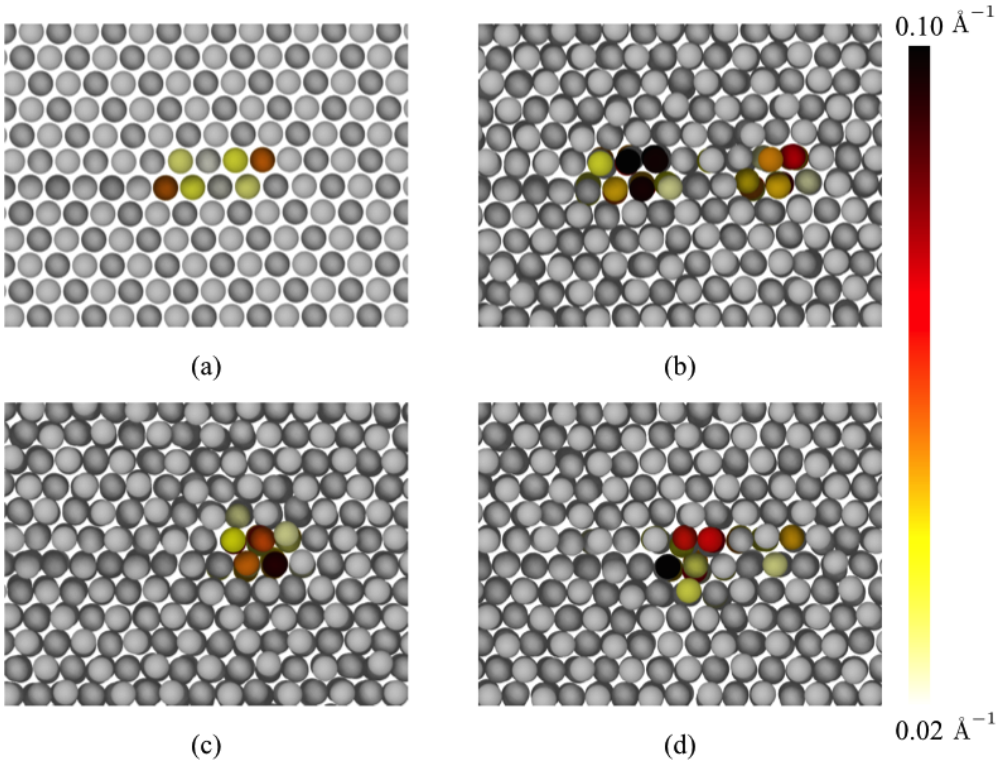

Figure 4.11: Nye tensor analysis as a tool for dynamical tracking of dislocations. Comparison between the relaxed system (a) and three configurations observed during the dynamics: (b) SP further away from each other, (c) recombination of SP and (d) transitions between equivalent slip systems.

4.6 Dislocation Glide

In this Section a phonon drag model is used for describing the glide of dislocation in an infinite (periodic along the direction of motion) box. The dislocation core is tracked using the Nye tensor, and glide velocities are studied as a function of the simulation temperature and the applied shear stress.

Phonon Drag Model

Consider a dislocation in metal at finite temperature, subjected to a certain stress. If the crystal does not include defects that can form pinning sites for the dislocation, the highest barrier against its motion is the Peierls one, due to bond rearranging at the dislocation core every time it moves an atomic distance. Consider external conditions such that this is overcome, the dislocation glide attains a viscous character and becomes determined mainly by energy dissipation due to elementary crystal excitations. Quasi-momentum exchange with crystal phonons is known to have a prominent role in defining the viscous drag [169]–[171]. Scattering of conduction electron in metals is another mechanism contributing to the damping of dislocation velocities [172], but it is known to be negligible for temperatures larger than 20% the Debye temperature Θ_{D} [173].

A dislocation parallel to ξ, moving in direction $\mathbf{x}$ with velocity $\mathbf{v} = \dot{\mathbf{x}}$ can be described by the following equation of motion:

$$\frac{\partial}{\partial t}\left(m\frac{\partial \mathbf{x}}{\partial t}\right)+B\frac{\partial \mathbf{x}}{\partial t} - \Gamma\frac{\partial \xi}{\partial \mathbf{x}} = \mathbf{F} \tag{4.22}$$

where $\mathbf{F}$ is the total force accelerating the dislocation (in the absence of obstacles it is the Peach-Koehler force $\mathbf{F} = \sigma\mathbf{b}$, where σ is the resolved shear stress and $\mathbf{b}$ the Burgers vector), B the damping coefficient, m an effective mass and Γ the line tension, which minimises the energy along the line as the dislocation moves. For small velocities with respect to the speed of sound in

the material, the steady-state velocity $\mathbf{v}_{ss}$ assumes the form

$$B(T)\mathbf{v}_{\mathrm{ss}} = \mathbf{b}\sigma \tag{4.23}$$

where the dependance on temperature of the damping coefficient $B(T)$ is made explicit. For temperatures exceeding $\Theta_{\mathbf{D}}$, B is found to have a linear dependence on T [174; 175], as the damping is proportional to the phonon density, and the latter depends on temperature linearly when the quantum effects can be neglected. Since the simulations in this Chapter are conducted using an IP, the quantum contribution can not be observed, independently of the simulation temperature.

Simulation Settings

The dynamics of an infinitely long dislocation is simulated by means of MD within the NVT ensemble. The defect is created by applying the elastic displacement (4.3), and it is periodic along the dislocation line $z = \xi$. A $[11\bar{2}]$ layer is removed to restore periodicity along the direction of motion, as discussed in 4.2, and a vacuum (15 Å thickness) is introduced along y in order to decouple the surface atoms from periodic images of the system. The lattice parameter is rescaled to the value predicted in Section 3.3 for the target temperature, and the atomic positions are optimised using a conjugate gradient algorithm with 10^{-2} eV/Å convergence threshold. The atomic velocities are rescaled, and the system is thermalised with a 10 ps MD simulation. The positions of the last three (111) layers are kept frozen along y. After thermalisation, a constant force field $F = \sigma/A$, where $2A = b^2\sqrt{3}$ is applied on these atoms, where A is the cross-sectional area. A deformation tensor consistent with the target stress is applied to the crystal.

Size Effects on Dislocation Glide

The MD simulations of crystal defects characterised by a long range stress field are influenced by the size and the shape of the simulation box. In pure MM simulations large systems can be treated, so that not only are size effects avoided but also systems locally resembling experimental samples (from a geometrical rather than chemical perspective) are described [6]. On the other hand, for QM/MM simulations, enlarging the QM region has a high computational cost, and should be avoided if not necessary.

For simulation of this kind, the size of the system has different effects depending on the direction considered. Using boundary conditions along the direction of motion x, a periodic array of dislocations is created, and fictitious interactions may arise between dislocations and emitted phonons. Two simulations are performed at low temperature with 100 MPa stress, with box length along x of 17 nm and 34 nm. The resulting dislocation velocities, obtained from linear fitting, are 1.59 ± 0.02 and 1.58 ± 0.02 nm/ps, indicating a good convergence. The length of the simulation box along y, the only direction along which the system is not periodic, affects the duration of the transient required before $\mathbf{v}_{ss}$ is reached, but not the velocity itself [161]. This is shown in Figure 4.12 (a), for low temperature simulations with a shear load of 100 MPa, using boxes of 23, 26 and 36 nm along y. Velocities are obtained by linear fitting on data subsets (3 ps time interval).

The size of the system along z is proportional to the length of the dislocation line. Dislocations with short line length are stiffer and stress/temperature fluctuations are therefore more likely to influence the motion of the whole defect at once. The convergence of the system along this direction is explored by simulations at 300 K at 100 MPa. Temperature is crucial for this test, as it affects periodicity along the line. In Figure 4.12 (b) the dislocation velocities obtained from data subsets (5 ps time interval) for systems of 0.5 1.0 and 1.5 nm are presented. Large fluctuations can be observed during the transient regime, which is much longer than the low temperature case,

but when the steady state velocity is reached there is not much difference between the three systems.

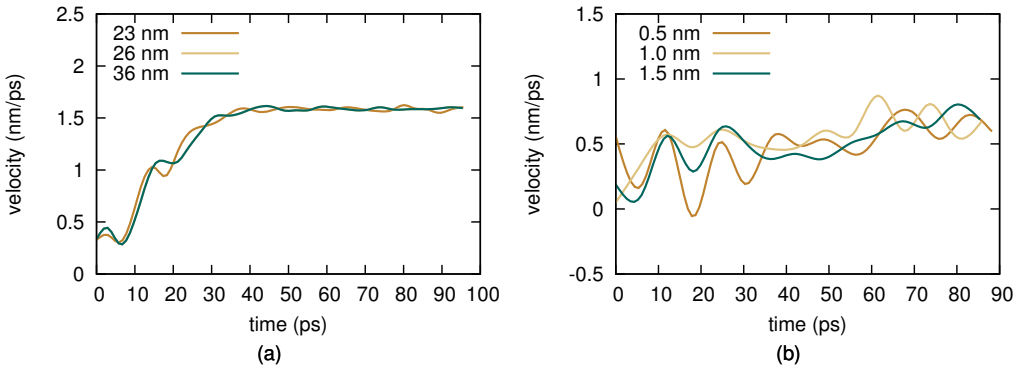

Figure 4.12: Size tests for MD simulations of dislocation glide in the γ phase for (a) the non-periodic direction of the system and (b) the line direction.

Dislocation Velocities: Results

The dislocation velocities are here evaluated as a function of temperature and stress. Values of the latter relevant to experimental application [57] are chosen (50–300 MPa). The simulation is chosen so that the stress temperature ratio is below 1 MPa/K. At this regime the steady state velocity is not expected to present large deviation from the linear regime [161].

The model systems are initially equilibrated by means of 10 ps of molecular dynamics. The deformation tensor is then applied to the crystal, together with force boundary conditions. The dynamics of the system is then simulated for 500 ps, saving a trajectory frame every 0.5 ps. The Nye tensor analysis is used for locating the dislocation core as

$$\mathbf{r}_c = \frac{1}{Z}\sum_{i=1}^{N} \alpha_s^{(i)} \mathbf{r}_i, \;\; Z = \sum_{i=1}^{N} \alpha_s^{(i)} \tag{4.24}$$

where $\alpha_s^{(i)}$ is the screw component of the Nye tensor for the i-th atom.

The resulting values of $\mathbf{r}_c \cdot \mathbf{x}$ as a function of time are presented in Figure 4.13 (c,d). The transient depends on the simulation conditions and can be as long as 100 ps if the temperature effects are dominating ($\frac{\sigma}{T} < 0.2\ \frac{\text{MPa}}{\text{K}}$). The dislocation velocities are calculated by linear fitting of the time/position curve for data collected after the transient. The calculated data is reported in Table 4.3 and plotted in Figure 4.13 (a) as a function of σ for the systems at different simulation temperature. In panel (b) the same data is plotted as a function of σ/T. The two curves overlap, so that assumption $B(T) = B_0 T$ for the drag coefficient is verified.

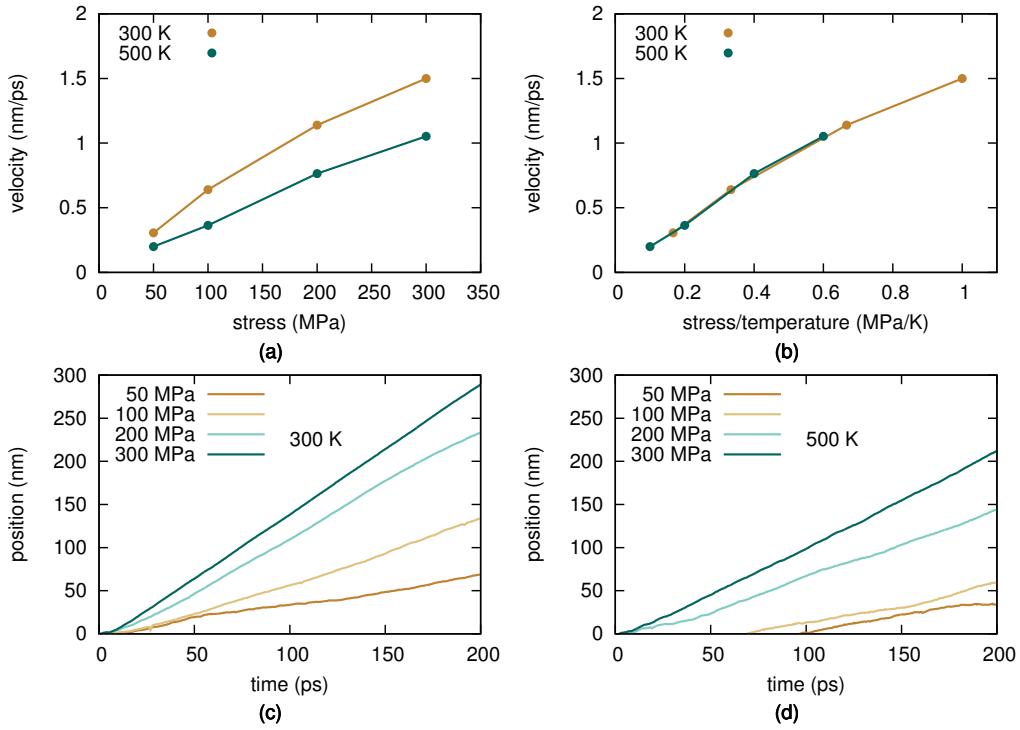

Figure 4.13: Dislocation velocity as a function of stress and temperature (a) and their ratio (b). Core position of a gliding dislocation as a function of time for simulations at 300 K (c) and 500 K (d) for increasing values of the shear stress.

The average value of (0.131 ± 5) μsPa/K at $\sigma/T < 1/3$ is in good agreement with previous results making use of the same potential [109; 161], despite the fact that smaller systems are used in this work. In Reference [176] a drag coefficient smaller by a factor of two is predicted, using an EAM potential developed in [177]. In Reference [159] a steady state velocity of 0.8 nm/ns is evaluated for low temperature simulation with applied stress of 100 MPa, using an EAM potential developed within the group.

	300 K			
σ (GPa)	0.050	0.100	0.200	0.300
v_{ss} (nm/ps)	0.306	0.640	1.139	1.500
B_0 (μsPa/K)	0.136	0.129	0.146	0.166
	500 K			
σ (GPa)	0.050	0.100	0.200	0.300
v_{ss} (nm/ps)	0.200	0.364	0.764	1.053
B_0 (μsPa/K)	0.124	0.137	0.130	0.142

Table 4.3: Steady state dislocation velocities and drag coefficients for simulations at 300 and 500 K.

4.7 Dislocation at the Interphase Boundary

In this Section, MD simulations of the glide of a screw dislocation towards the γ/γ' interface are presented in the case of a coherent IPB, and for a system in which the misfit strain is partially relaxed by the presence of a misfit edge dislocation. In the first case, an attractive interaction between the matrix dislocation and the precipitate is observed, and whenever the Peierls barrier is overcome the first SP will deposit at the γ/γ' interface. In the second case, a larger energy barrier is found.

The size of the simulation cell is $28 \times 16 \times 1$ nm^3, and the orientation of the crystal is the same as in the previous Section. The dislocation is created at the centre of the cell, at a starting distance $d = 25$ Å from the IPB.

The steady state gliding velocity is not reached, as a larger distance would be required. The effect of the applied strain/stress on the simulation cell is consequently underestimated. Periodicity along the direction of motion is not required for this set of simulations, as the dislocation does not cross the boundary of the cell. For the same reason, the outermost layers of the cell can be kept frozen, and the simulation performed at constant strain. In constructing the simulation cells, geometry optimisation is used at multiple times in order to avoid the overlap of stress fields, which can result larger then the Peierls stress and thus cause spurious dislocation glide. Every optimisation is performed using a conjugate gradient algorithm with a force convergence threshold of 10^{-3} eV/Å.

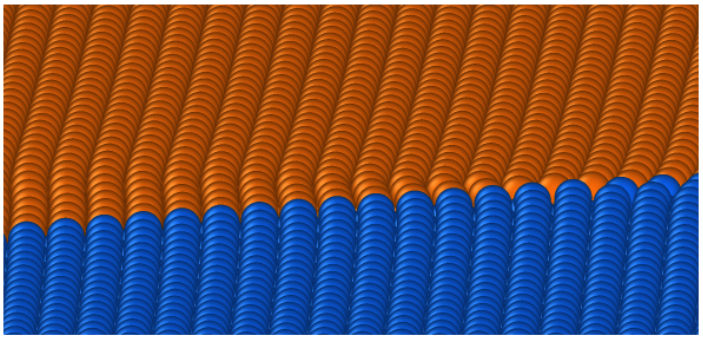

Figure 4.14: Interface between the γ (orange) and γ' (blue) phases. The edge character of the misfit dislocation is evident from the system geometry.

The initial configuration for the coherent IPB system is generated using the following procedure. The atomic positions for the system, composed only of Ni atoms, are optimised in order to minimise the stress field of the {111} surfaces. The matrix dislocation is introduced by applying the elastic displacement (4.3), and the system optimised again in order to obtain dissociation into SP dislocations. At this point, atoms at the open surface are frozen, Ni atoms are converted to Al in order to form the precipitate, and the system is optimised again to relax the interfacial strain. The start-

ing configuration for the system including the misfit dislocation is obtained starting from this one. The most external {111} layer is removed, and the atomic positions are rescaled accordingly to the equilibrium lattice parameter for each phase. Finally, the constraint on surface atoms are removed, and relaxation of the system leads to the formation of a misfit dislocation, displayed in Figure 4.14.

A deformation tensor is then applied to these initial configurations, and the dynamics integrated for 30 ps at low temperature. This is repeated for different values of the shear stress, evaluated from the applied strain using the elastic constants. In the case of a coherent IPB, simulations are performed at 10, 50 and 100 MPa. In the first case, the Peierls barrier is not overcome and dislocation glide does not occur. In the other two cases, a qualitatively similar behaviour is observed. The energy profile during the dynamics at 50 MPa is reported in Figure 4.15, and various frames of the dislocation/interface geometry corresponding to the extrema of the energy curve are displayed.

The dislocation is initially gliding in response to the applied strain, as illustrated in frames 1 and 2 . When the distance between the dislocation and the interface is shorter than twice the cutoff of the IP, the dislocation is attracted towards the IPB (energy gain between frames 2 and 3). The minimum potential energy is reached in configuration 3, whenever the leading SP enters the precipitate, and a complex stacking fault is formed. The second SP is pinned at the IPB, as the applied stress is not large enough to cause the formation of an APB, as suggested by the GSF profile in Figure 3.12. As the leading partial penetrates further into the precipitate, a second complex stacking fault is formed, and a (local) maximum of the potential energy is observed (frame 4). At this point, the dislocation is subjected to a strain of opposite sign with respect to the initial one, as understood from the distribution of velocities before and after dislocation pinning (Figure 4.13). The positive/negative velocity lobes observed in (LHS) are dispersed

in the precipitate, and another distribution of opposite sign arises (RHS). The dislocation starts gliding in the opposite direction, until this strain field is relaxed (frame 5). At this point, the combined effect of the applied stress and the SP trapping in the precipitate reverts again the direction of motion. An oscillatory behaviour is finally observed, with one SP trapped within the precipitate and the other one incapable of penetrating it due to the large energy barrier associated with the formation of an APB.

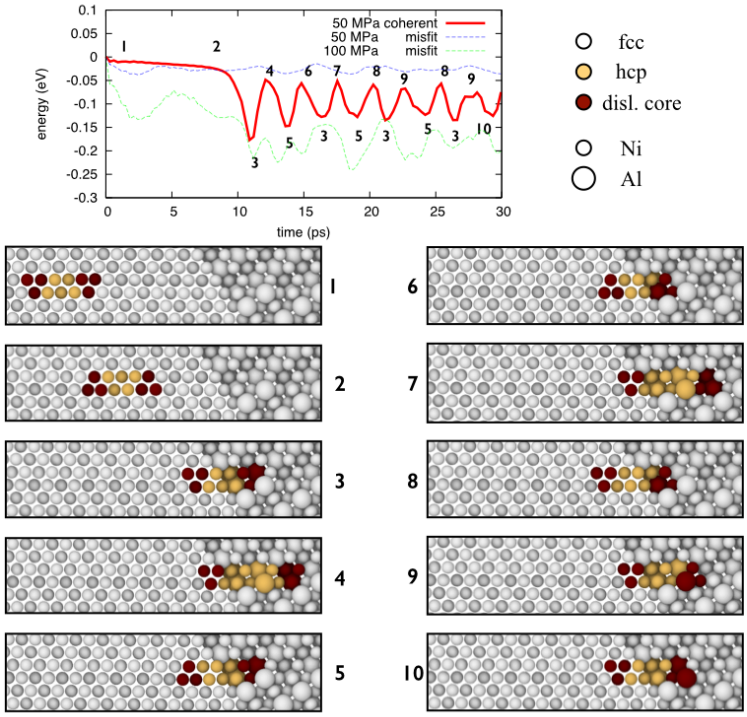

Figure 4.15: Energetics and relevant trajectory frames for dislocation pinning at the γ/γ' coherent interface.

A low temperature dynamical simulation of the system including a misfit dislocation is performed with applied stresses of 50 MPa and 100 MPa. The resulting energy profile and relative configurations for the first simulation are reported in Figure 4.16. The dislocation starts gliding towards the interface

in response to the deformation (frame 2). The system reaches its minimum total energy whenever the distance between the IPB and the dislocation is 16 Å (frame 2). When it becomes smaller than twice the potential cutoff, the energy increases, and a maximum is observed in frame 3. A repulsive interaction between the dislocation and the interface is thus observed, as the misfit strain is partially relaxed because of the misfit dislocation. The formation of a complex stacking fault is unfavourable with respect to the previous case, and the leading partial is not able to penetrate the precipitate. Starting from frame 4, the dislocation glides backwards because of this repulsive interaction. The initial core position is not reached because of the deformation of the system, and oscillatory gliding within the γ channel is instead observed.

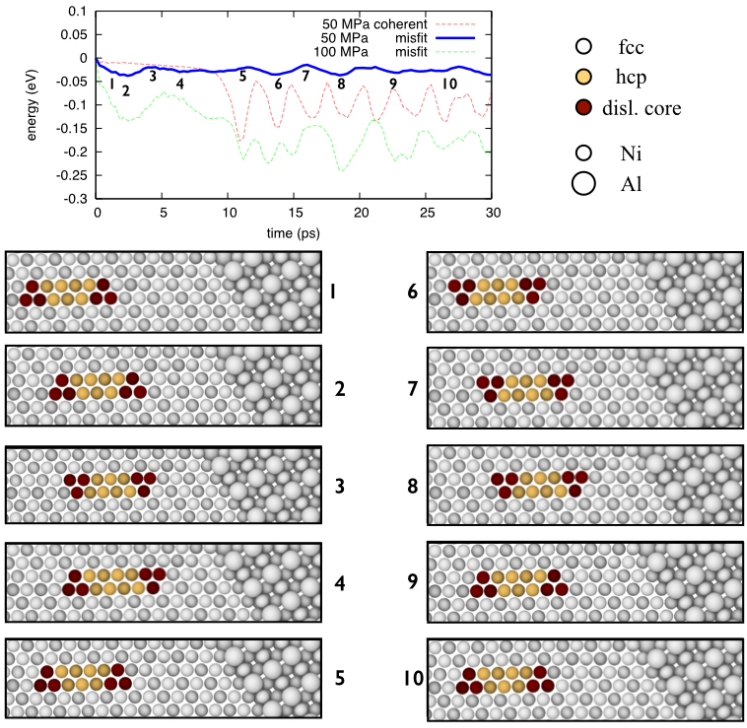

Figure 4.16: Energetics and relevant trajectory frames for a dislocation gliding towards a γ/γ' interface including a misfit dislocation: low stress regime.

When the stress is increased to 100 MPa, a different behaviour is observed, as reported in Figure 4.17. The dislocation is initially gliding towards the interface, in response to the applied deformation, thus minimising the total energy of the system (frame 2). Whenever the distance between the defect and the interface is less then twice the IP cutoff, a repulsive interaction is observed. A total energy maximum is observed at 12 Å distance, as in the previous calculation. In this case, the elastic deformation is enough to overcome this barrier, and starting from $d = 6$ Å, an attractive interaction is observed and the leading SP penetrates the precipitate. A behaviour similar to the case of a coherent IPB is observed.

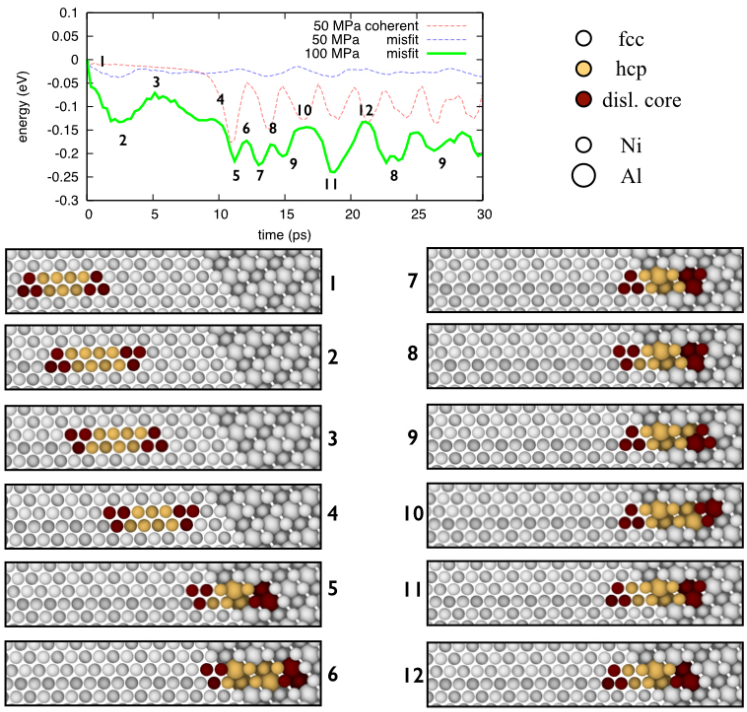

Figure 4.17: Energetics and relevant trajectory frames for a dislocation pinned at a γ/γ' interface including a misfit dislocation.

We conclude that, as dislocation reaches the γ/γ' interface and rearranges to minimise the misfit strain, the barrier for entering the precipitate is increased for other dislocations. Thermal effects are found to have a retarding effect: for a simulation at 500 K, the first SP enters the precipitate after 25 ps of dynamics. If the temperature is further increased at 1200 K, no penetration is observed after the first 30 ps, and cross-slip of the matrix dislocation occurs several times.

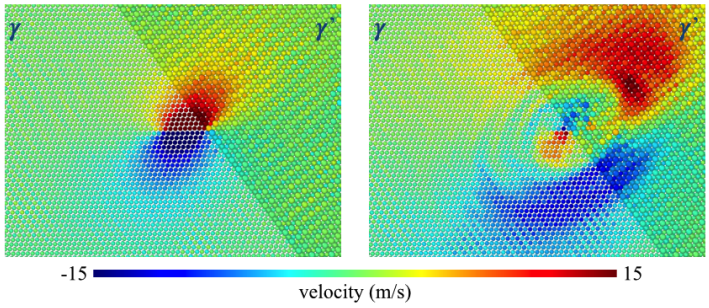

Figure 4.18: Velocity distribution for a gliding dislocation, before (LHS) and (RHS) being trapped at a γ/γ' interphase boundary.

4.8 Summary

In this Chapter a study of dislocation glide is presented. The continuum elasticity theory is briefly reported, and validated by calculating the core contribution to the total energy of a dislocation core by EAM calculations. A phonon drag model is used for describing the dislocation glide in the γ phase, for which the drag coefficient is found to be a function of the ratio between temperature and shear stress. Finally, the study of dislocation trapping at the γ/γ' is reported for different deformation and for different geometers of the interface (fully coherent and with a misfit dislocation) is presented, comprehensive of a detailed description of the atomistic mechanism.

CHAPTER 5

Multiscale Simulations

5.1 Introduction

This Chapter is devoted to the implementation of QM/MM simulations for the dynamics of dislocation cores in nickel alloys. Careful testing is presented beforehand, in order to determine the ideal size of the QM region and the minimum buffer width necessary for obtaining accurate forces. This analysis is carried out for a number of crystal defects in Ni-alloys, and extended to the case of the α phase of iron, a more challenging material because of its magnetic properties. The usage of a QM/MM scheme offers an improved description of the local geometry of the dislocation cores, and it is crucial to describe Shockley Partials at high temperature regimes, in particular when a significant of aluminium is present in the matrix composition.

In Section 5.2, a simple example is presented to offer insight about the reliability of an EAM potential when the system is far from its structural minima. The compression of the bond between two atoms causes charge rearrangement to screen the ionic interactions, breaking the EAM ansatz of an exponentially decreasing charge density. In Section 5.3 a detailed study of the convergence of the QM forces calculated using subsets of the periodic system (clusters) is presented for a selection of crystal defect including vacan-

cies, dislocations and chemical impurities in the γ phase. The minimal size of the region requiring the QM augmentation is determined, by calculating the MM force error with respect to DFT references and by analysing the convergence of electronic properties, such as magnetic moments, using auxiliary QM calculations. A digression on the α phase of iron is offered in Section 5.4, showing that the convergence of forces is much more difficult when dealing with materials with larger magnetic moments than nickel. In Section 5.5 the convergence of the electronic structure, rather than the Hellmann-Feynman forces, is studied for an atom at the centre of a cluster, for both nickel and iron. Finally, in Section 5.6, a set of LOTF simulation of dislocation cores in γ is presented, for increasing temperature, stresses and chemical complexity. The results are compared with MM simulations, indicating that the EAM approach can be very inaccurate in certain conditions.

5.2 Necessity of QM Regions

Comparisons between data obtained using DFT and with EAM potentials, carried out in Chapter 3, revealed that the MM method is overall accurate in describing the basic properties of Ni alloys, with only a few exceptions, related to chemical transferability issues. In Section 3.4, for instance, a large overestimation for the binding energy of an Al impurity in the γ phase was found, due to incompatibility between the energetics of this system and of the γ' phase, presenting the same local environment (nearest neighbours) for the Al atom. Another example of the lack of the transferability of the IP is provided in Section 3.5, where an underestimation of the elastic energy of hcp Ni is found, due to incompatibility of the pair-interaction energy term in modelling the shells of neighbours of hcp crystals. A poor description of the energetics is also found for the run-on stacking fault in Section 3.6. The latter is not to a serious issue, as this configuration is energetically very unfavourable, and therefore not likely to occur during a typical MD run.

The data suggests that the EAM potential is inaccurate only for a very limited set of cases. On the other hand, the tests presented so far are mostly focussed on the minima of the PES. While the energetics of these structures are crucial, further testing is required to verify the ability of the EAM potential to reproduce DFT forces in configurations obtained with MD simulations, as would be necessary to correctly predict thermodynamic observables [148]. Even for the most accurate IP, these forces are likely to be correct only when the atomic geometries are deformed below a certain threshold.

In this Section, I show how the QM and the MM forces get progressively further apart as the system is moved away from equilibrium, even for bulk structures, using a simple model in which a Ni atom is shifted towards one of its nearest neighbours. A $3 \times 3 \times 3$ 108-atom supercell is used to isolate this atom from its periodic replica, and the force as a function of the bond length is calculated using DFT and EAM. Resulting data, displayed in Figure 5.1 (a), indicate a significant deviation between the two approaches for atomic forces larger than 2.5 eV/Å. Moreover, the EAM force is linearly increasing for decreasing values of the bond length, while the DFT one deviates significantly from this regime. This can cause the system to visit unfavourable configurations during MD simulations using the classical potential. The effects of the underestimation of the repulsive forces for systems out of equilibrium are already observed in Section 3.3, in which the thermal expansion coefficient calculated using the EAM potential is much smaller with respect to the reference experimental value.

Similarly, a failure of the EAM model is observed in Reference [104], from a charge density perspective rather then for the atomic forces. The EAM ansatz of an exponentially decreasing charge density is tested against deformations of a Cu crystal by calculating its value in a (vacant) octahedral site. When a second nearest neighbour to the vacant site moves towards it, the site loses charge in favour of the region comprised between the approaching atom and its nearest neighbours, violating the EAM ansatz.

The same calculation is repeated here for the previously described Ni system, and a similar behaviour is observed in charge density difference between the crystal and isolated atoms, as shown in Figure 5.1 (b).

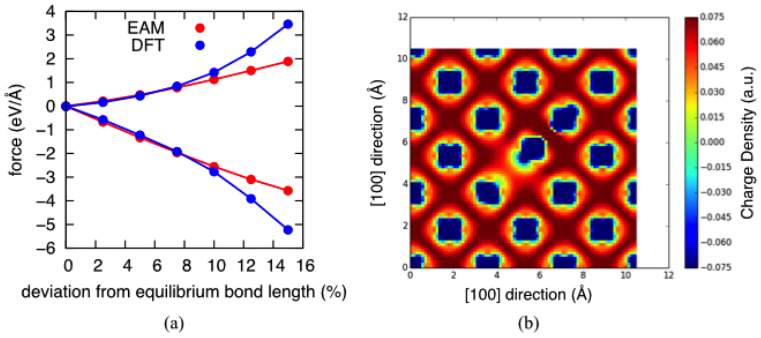

Figure 5.1: (a) EAM and DFT forces calculated for a Ni atom displaced from its equilibrium position along the [110] direction towards a neighbouring fcc site. (b) Charge difference with respect to isolated Ni atoms in a 100 plane for a bulk system with a single atom displaced towards one of its neighbours along the [110] direction by 12% of the equilibrium bond length.

While these effects are often negligible for bulk systems, as a modification of the bond length of 10% or more is unlikely to occur at temperatures below the melting point, they are more likely to be observed near a crystal defect. Two classes of defects can therefore be defined. The first one includes the defects not treatable with the EAM potential, because of transferability issues or because they are not parametrised (e.g. impurities). For defects such as vacancies, belonging to the second class, the minima of the PES are accurately characterised by the IP, but a significant deviation between the QM and the MM atomic forces arises when the system is out of equilibrium, e.g. during a high-temperature MD simulations. In the next Section, the typical EAM force errors are studied for a number of defects pertaining to both classes, for configurations thermalised at 1200 K, the typical operational temperature of Ni-based alloys turbines.

5.3 Width of the QM Subsystem

Cluster QM Calculations for Bulk Systems

One of the main advantages of force mixing QM/MM techniques over energy mixing methods is the absence of edge effects. On the other hand, very accurate forces are required for this scheme, and the QM calculation is performed not only on the QM region, but on a larger cluster comprehensive of a buffer region, as explained in Section 2.7. The size of this buffer region should be chosen so that the forces in the QM region are identical to those that would be obtained in a full QM calculation of the entire system. In practice, this can lead to very large QM clusters, resulting in not affordable calculations, given the cubic scaling of DFT methods. A threshold for the force accuracy has therefore to be set, small enough to guarantee a certain level of chemical accuracy, but large enough to make the calculation affordable. In this Section, the behaviour of the QM forces evaluated using a cluster (cluster DFT) is studied for clusters of increasing size. The force error is defined as the difference between the so-evaluated force and a fully-periodic reference calculation. This is also compared with the MM force deviation with respect to the same DFT reference. In the case of crystal defects, this allows to determine the width of the QM region, as the IP is likely to became more accurate when the system recovers a bulk-like configuration. These QM regions are expected to be small, because of metallic screening. As will be clear from the rest of the Section, a sensible choice for the force error threshold of cluster DFT calculation is 0.1 eV/Å, achievable for most of the systems here considered using clusters with less than 100 atoms, and accurate enough when compared to the typical DFT force accuracy of ~ 0.02 eV/Å. Note that very large clusters (at least 200 atoms) are required in order to lower the threshold to 0.05 eV/Å, as shown in Figure 5.13 (b).

As a starting point, the convergence of QM forces using clusters of increasing size is tested for bulk system of γ and γ'. Since crystal defects are not present, and no chemical reactions are occurring, the width of the buffer region necessary to decouple the QM region from spurious surface states determined in this Section is the minimum one associated with the material, and therefore constitutes an effective calculation of the force locality. The 108-atom configurations described in Section 3.3 for both γ and γ' are used. For each of them, an atom is selected, with the modulus of the force acting on it larger then 0.5 eV/Å, and is treated as a monoatomic QM region. The forces for clusters of increasing size are compared with the reference ones for the periodic system. In the case of γ', the force convergence is checked separately for Ni and Al atoms. Each cluster is separated from its periodic images by 10 Å of vacuum. Because of the large system size this leads to, the BZ is sampled using only the Γ point. The other parameters for the DFT calculations are the same as those reported in Section 3.1. The resulting force errors are displayed in Figure 5.2, averaging over 10 configurations and over the cubic axes.

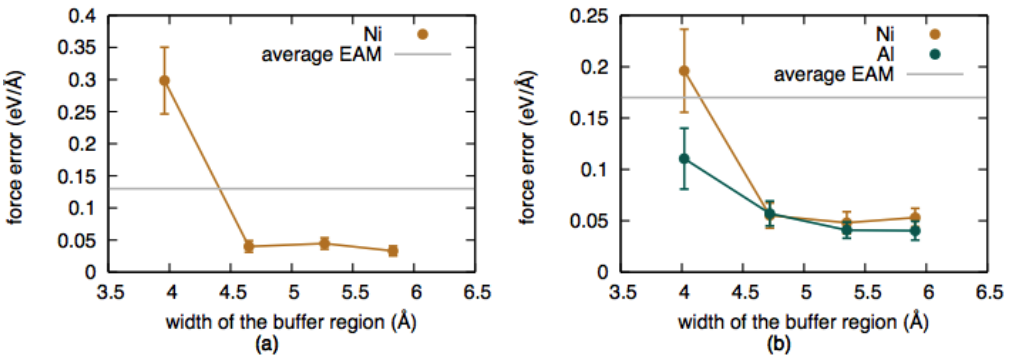

Figure 5.2: (a) Convergence of the QM cluster forces for Ni atoms in γ, (b) Ni and Al atoms in γ' (b). The average EAM force error with respect to DFT is indicated with grey lines.

A rapid convergence of the QM force is observed for cluster radii larger than 4.3 Å, i.e. including the first three shells of neighbours for the central QM atom. The average EAM error with respect to the full-DFT force is indicated with grey lines. Lower force errors are observed in the case of γ', in particular for the Al atom. This is attributed to the absence of a magnetic moment for the latter, and to the overall small magnetisation of the system. A further observation about the importance of magnetic properties for the locality of the QM forces is provided in Section 5.4, where the present analysis is extended to the α phase of iron.

Point Defects

In this Section the required size of a QM region in the proximity of a point defect is studied. Only data for the γ phase are presented, as Re and W are known to partition there (cf. Section 3.4), and only vacancies in γ are relevant to this work, because of their interaction with matrix dislocations. For each system, 10 uncorrelated configuration frames are generated by means of MD simulations, at the target temperature of 1200 K. In the case of the vacancy and of the Al impurity, the EAM potential is used, with the same simulation parameters previously described in Section 3.3. For systems including a W or Re chemical impurities, *ab initio* MD is used, with the same settings as in the calculations reported in Section 3.4. These simulations are carried out within the NVT ensemble, using a 2 fs time step and a Nosé-Hoover thermostat with mass corresponding to an 80 fs oscillation period. The systems are equilibrated for 2 ps, and a configuration frame is saved every 200 fs during the next 2 ps production calculations.

The distribution of the EAM force error with respect to reference DFT data is obtained by counting the number of occurrences of an error on a single component of the force vector. Bin of 0.05 eV/Å width are used, and the plots are smoothened using cubic splines. This error distribution is shown in Figure 5.3 (a) for the atoms neighbouring the vacant site.

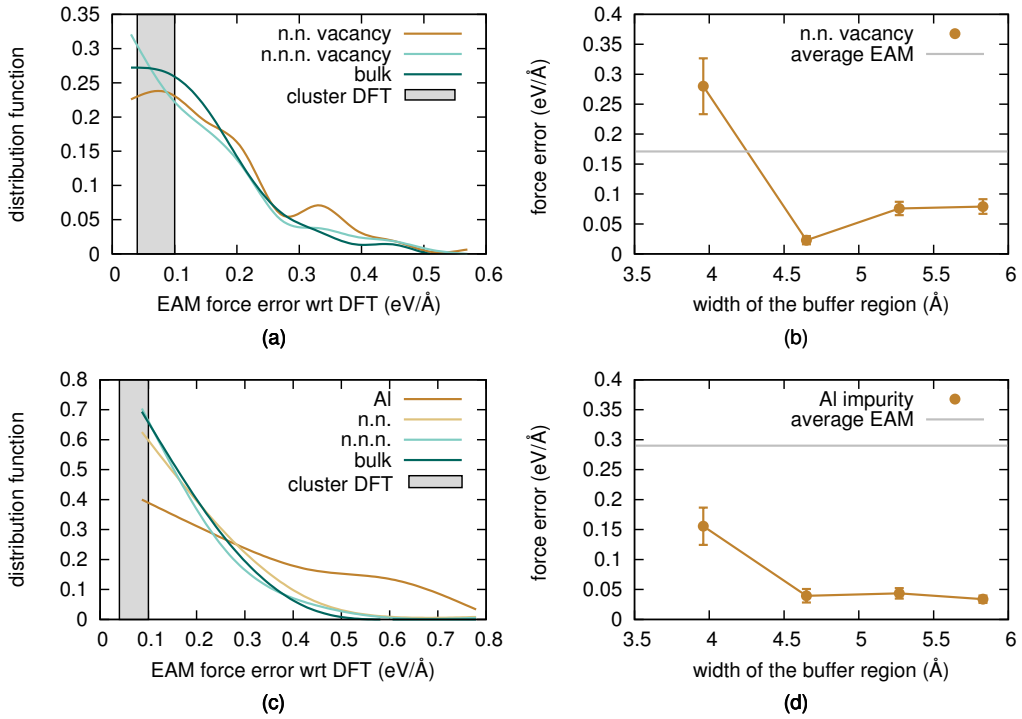

Figure 5.3: EAM force error distribution with respect to reference DFT calculations for (a) atoms neighbouring a vacancy and (c) a chemical Al impurity. Convergence of the QM cluster force for both cases (c,d).

The different line colours correspond to different distances from the vacancy: on average 2.5 Å for n.n. and 3.5 Å for n.n.n. atoms. Results for atoms farther than 4.3 Å from the defect are included for reference. For the latter set, 50% of the data points have an absolute force error below 0.1 eV/Å and only 20% exceed 0.2 eV/Å, in line with the results reported in Section 3.3 for bulk atoms. For the n.n. to the vacancy the error distribution is broader. While for 40% of the data points the error is below 0.1 eV/Å, a larger population of forces deviating by 0.3 eV/Å appears, including errors as large as 0.8 eV/Å. The error distribution for n.n.n. has an intermediate behaviour.

The EAM potential is in fact by design accurate enough for modelling the dynamics of vacancies, as both the formation and the migration energies are included in the fitting database used to develop the IP [5]. However, although the EAM forces integrate to the correct migration barrier, the local description of the PES is not as accurate for the n.n. of vacancies as it is for the bulk-like atoms. As a result, the potential could easily fail to describe the interaction between a vacancy and other defects such as dislocations.

The force convergence with respect to the width of the buffer is presented in Figure 5.3 (b). In this case, the QM region is composed of 12 atoms, so that the radius of the buffer region does not correspond to the radius of the whole cluster as in the previous case. The convergence of the forces is reached when the first three shells of neighbours of QM atoms are included within the buffer region, as in the case of the bulk systems (cf. Figure 5.2)

The same analysis is carried out for an Al impurity in the γ matrix. The error distribution, displayed in Figure 5.3 (c), shows that the QM forces on the impurity atom are not reproduced by the classical potential, with only 20% of the forces within 0.1 eV/Å from the reference values and 50% of the errors larger than 0.3 eV/Å. This is in line with the overestimation for the Al impurity binding energy observed in Section 3.4. An overestimation of the forces acting on the Al atom is expected to be associated to this energy difference. This is verified by comparing the absolute value of the force error with the deviation between force moduli, as reported in Table 5.1.

$\mu(\lvert f_{\mathrm{MM}} - f_{\mathrm{QM}}\rvert)$	$\mu(\lvert f_{\mathrm{MM}}\rvert - \lvert f_{\mathrm{QM}}\rvert)$	$\mu(\lvert f_{\mathrm{QM}}\rvert)$
0.29± 0.07 eV/Å	0.28± 0.07 eV/Å	0.72 ± 0.11 eV /Å

Table 5.1: Average EAM force error for an Al impurity in the γ phase.

The Al impurity therefore requires a QM augmentation. The Al–Ni pair interaction can be refitted to the correct energetics for this defect. This would on the other hand cause a significantly reduced accuracy for the γ' phase, as the first shell of neighbours of the Al atom is identical in the two cases.

The convergence of the cluster QM forces for increasing size of the buffer region is presented in Figure 5.3 for the Al atom. The forces converges using small clusters, as in the previous cases. Here, also a minimal cluster including only the first two neighbour shells (18 atoms) produces more accurate results than the EAM potential.

In the case of Re and W impurity atoms in the γ matrix, the width of the QM region cannot be determined by direct comparison with EAM data, as the IP is not capable of modelling atomic species other then Ni and Al. A set of auxiliary systems is used, for which the impurity atom is substituted with a Ni one. The deviations with respect to the original set of configurations are calculated for the atomic forces and for the magnetic moments, the latter evaluated using Bader analysis [75]. The MM region is then defined as the region in which the difference between these quantities for the two systems is below a certain threshold. The chemical impurities considered here do not produce significant charge transfer. The calculated atom-polarised charge show a depletion below 0.5% for n.n. Ni atoms in the case of Re and below 1% in the case of W. No difference can be observed for next nearest neighbours. Whilst the charge transfer is negligible, its rearrangement due to the impurity atom leads to lower magnetic moments for its neighbours, as shown in Figure 5.4 (a).

The corresponding force difference is presented in 5.4 (b). The Re atoms are introducing a larger deviation with respect to W ones, despite the weaker chemical effect observed in panel (a). This plot indicates that the mechanical effect of impurity atoms is limited to n.n. atoms. A peak is observed for the shell at 5 Å, equidistant from the periodic images of the impurity atom, below the accuracy threshold of 0.1 eV/Å. Purely electronic properties, such as the Density of States, converge later more slowly than the atomic forces, as shown in Section 5.5, so that an inaccurate value for the magnetic moments of n.n.n. is not to be considered a major problem.

The convergence of QM forces with respect to cluster size is reported in Figure 5.4 for Re (c) and W (d). In this case, larger clusters are required in order to obtain QM forces within the accuracy threshold of 0.1 eV/Å. In both cases, a cluster of ~ 7 Å radius is required, corresponding to the first 8 shells of neighbours of the impurity atom. The forces on the chemical impurity and its neighbours converge simultaneously in both cases, indicating strong coupling between these atoms. As clusters required to obtain converged QM forces contain at least 130 atoms, a full QM/MM simulation for this system would be much more expensive than an Al impurity atom in γ.

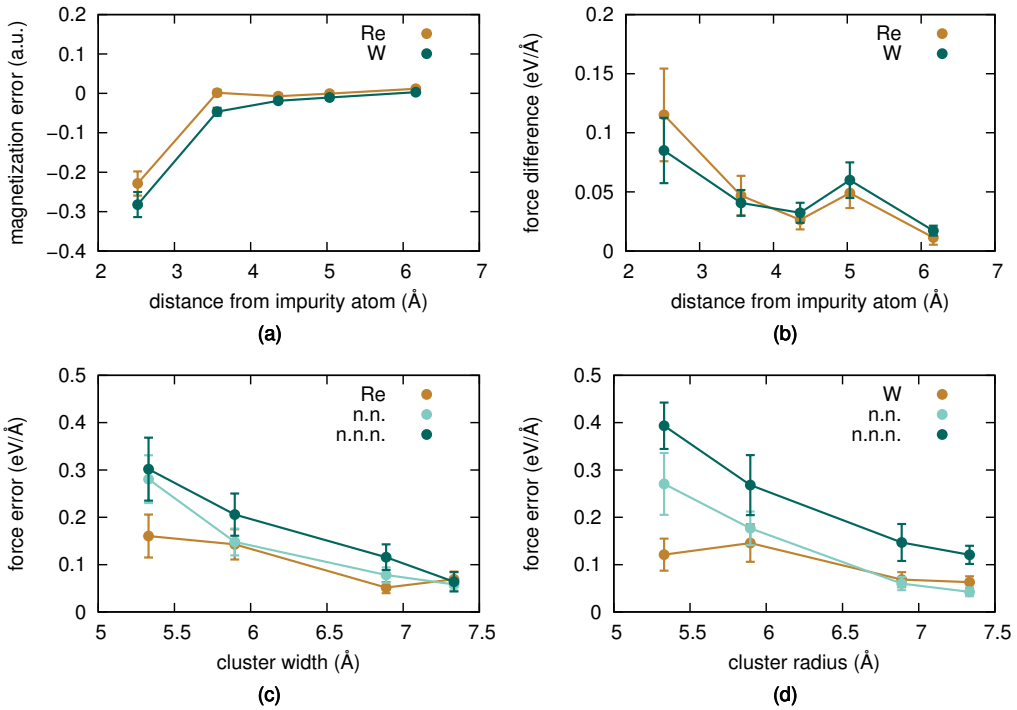

Figure 5.4: Comparison between magnetic moment (a) and atomic forces (b) between a system including a chemical impurity (Re,W) and an auxiliary one, with only Ni atoms in the same positions. Convergence of the cluster QM forces on an impurity atom and its neighbours for Re (c) and W (d).

The overestimation of the binding energy for an Al impurity observed in Section 3.4 may lead to some considerations: firstly, the EAM potential is clearly not describing this kind of defect correctly, because of its intrinsic lack of transferability. Secondly, this can be turned to our advantage, as large binding energies in γ are usually associated with heavy atoms such as Re and W. In Figure 5.5, three error distributions are compared for a chemical impurity (a) and its neighbours (b). The configurations are the same generated for the case of an Al impurity, but QM calculation have been repeated changing the type of this atom into Re and W.

The resulting data indicates that, in the case of an isolated impurity within the γ matrix, the MM Ni-Al parametrisation is in fact more closely describing a Ni-Re or Ni-W system. About 33% of the error points are below 0.1 eV/Å (to be compared with 20% for Al), and less than 10% are above 0.3 eV/Å (50% for nickel). No difference can be observed for the description of neighbouring atoms. The accuracy in modelling these atoms is at the ionic level, and important features of the systems such as the shape of the GSF energy curve (cf. Figure 3.14) cannot be reproduced. However, the potential can still be used to describe 'on average' the multi compositional γ phase typical of commercial Ni alloys.

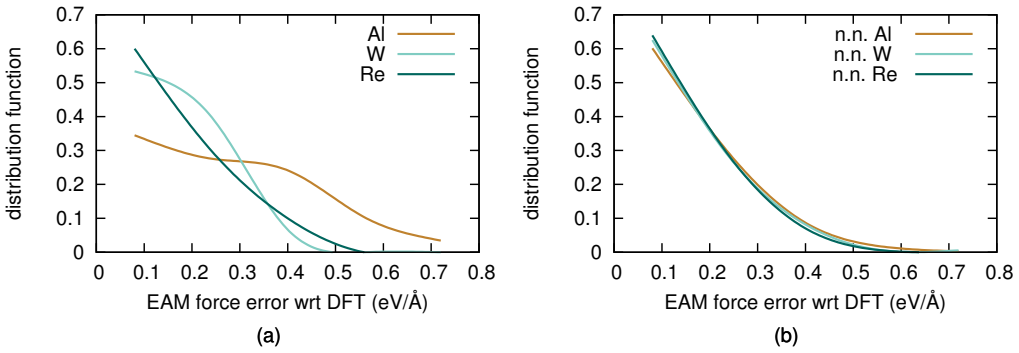

Figure 5.5: Comparison of EAM force error distributions for different chemical impurities for (a) the impurity atom and (b) its neighbours

Dislocation Core

As a next step, a screw dislocation in the γ phase is considered. The crystal is oriented along the orthorhombic cell axes $x = [11\bar{2}]$, $y = [111]$, $z = [\bar{1}10]$, and a $48 \times 34 \times 8$ supercell of the 6-atom elementary system (78336 atoms) is used. A single screw dislocation is introduced at the centre, and open boundary conditions are imposed adding a vacuum region of 15 Å width along x and y, as discussed in Section 4.2. The cores of the SP dislocations are located by means of the Nye tensor, using Equation (4.24), and atoms are classified accordingly to the distance from these points. The n.n. atoms, located within 2 Å from the dislocation core, are characterised by a screw component of the Nye tensor larger than 0.04 Å^{-1}, thus contributing about 70% of the Burgers vector. The n.n.n. atoms are those within 4 Å of the dislocation core, and present an average screw component of about 0.01 Å^{-1}.

DFT calculations cannot be performed on the whole system because of its size. The convergence of QM cluster forces at dislocation cores can still be monitored, as displayed in Figure 5.6 (b,d). The reference values are taken from a larger cluster, not shown in the plot, including 9 neighbouring shells, corresponding to 177 atoms. The average error is decreasing for increasing system sizes, and falls below the threshold of 0.1 eV/Å with a cluster radius of 5.5 Å. A dependance on the crystallographic direction is observed: while along x the force converges using the same cluster radius as in bulk systems (cf. Figure 5.2), an additional neighbour shell is required along the y direction. The force convergence can be improved by increasing the width of the Gaussian smearing of occupancies to 0.5 eV, as displayed in Figure 5.6 (b,d). The corresponding accuracy loss for the electronic structure is not significant, as for this cluster size the density of electronic states is not fully converged, as discussed in Section 5.5. A set of 30 atoms is then selected from each reference frame, and DFT calculations are performed for each of them using 5.5 Å radius clusters. The accuracy of the EAM potential is tested by direct comparison. The analysis is carried out separately along x and y.

The EAM potential performs reasonably well in both cases, with only 40% and 35% of the forces deviating by more than 0.2 eV for x and y directions respectively. Note that the corresponding value for the bulk system is 25%. Errors along x are slightly higher, and the presence of vacancies yielding the formation of jogs during diffusion will very likely increase the force error along y. Moreover, in both cases, there is a significant probability of incurring force deviations as large as 0.6 eV/Å for both n.n. and n.n.n. atoms. The latter present larger force errors along the x direction, due to the lattice distortion from the linking of the two SPs across the stacking fault region.

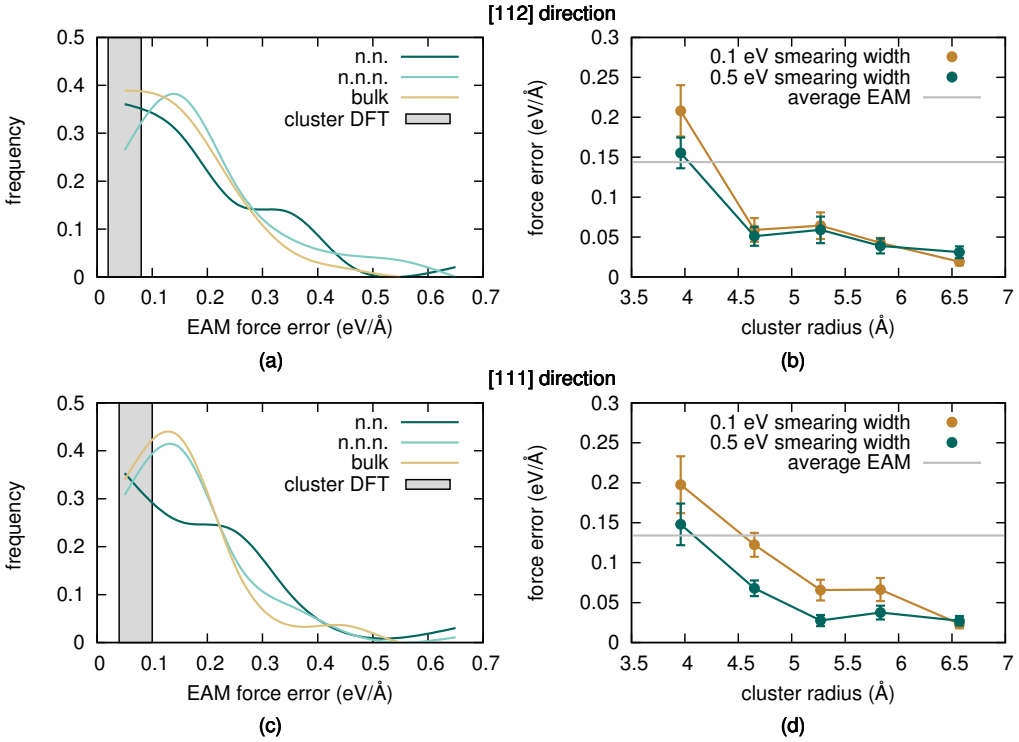

Figure 5.6: Distribution of EAM force error for atoms neighbouring a dislocation core along x (a) and y direction (c). Convergence of the cluster QM forces for different smearing widths (b,d)

5.4 Extension to other Materials: α iron

While the main focus of this work is on Ni-based alloys, it is interesting to investigate the cluster QM force convergence for other materials, thus providing insight about the feasibility of QM/MM simulations in a wide range of systems. In Reference [178], these data are provided for Si-based systems. Converged QM forces are obtained using a ~ 5 Å width buffer for a perfect Si crystal and a ~ 7 Å width buffer for a (001) surface. Whenever the ionic interactions of the system becomes more complicated due to a more complex chemical composition, as in the case of α-quartz and of amorphous silica, much larger clusters (~ 12 Å) are required.

Here, a strong chemical dependence on the required size of the buffer region is also observed, for instance in the case of Re and W impurities in the γ matrix, as shown in Figure 5.4. In this section, this analysis is carried out for a system, α-iron, that is significantly challenging to model using a QM/MM scheme, as the magnetisation is much larger than in nickel alloys. Spurious spin rearrangement at the open surfaces of the QM clusters will be higher, so that Fermi-level crossing effects become more likely to propagate to the centre of the QM region, and affect the calculated forces on the central atom. Because of this effect, large QM clusters are typically required in order to obtain well converged QM forces.

Various heuristic approaches to accelerate the convergence are investigated in this work, including (i) imposing a larger Gaussian smearing width, (ii) allowing the QM zone to host a net charge to boost convergence, or (iii) constraining the magnetic moment of each atom to the zero temperature bulk value. Test calculations show that the dipole correction, applied using the algorithm originally proposed in Reference [179] and later implemented within the VASP package, does not significantly affect the computed forces, indicating that the interaction between electric dipoles generated on the QM clusters by surface effects is negligible.

The convergence of forces with respect to the cluster radius is studied for two systems: a $4 \times 4 \times 4$ 128-atom supercell of bulk α-Fe and a larger system centred on a $\frac{a}{2}\langle 111 \rangle \{110\}$ screw dislocation. The reciprocal space is sampled using a $4 \times 4 \times 4$ MP grid in the first case. All cluster DFT calculations are performed using only the Γ point. The classical calculations use a high quality EAM potential [12] originally developed for self-diffusion studies on Fe surfaces. All simulated systems were thermalised at 1200 K using classical MD simulations following the same protocol detailed for Ni systems.

As a starting point, the magnetic behaviour of full-shell Fe clusters is studied by means of DFT calculations. The neighbour shell resolved magnetic moment difference with respect to perfect bulk, obtained by means of Bader analysis for these systems at 0 K, are shown in Figure 5.7. Atomistic models of the clusters are displayed in the inset. From the reported data, it is not only clear that undercoordinated surface atoms have a magnetic moments about 50% larger with respect to a periodic structure ($2.2\mu_B$), but also that this effect propagates towards the centre of the cluster, so that, if one cluster is not large enough, the central atom is also significantly affected.

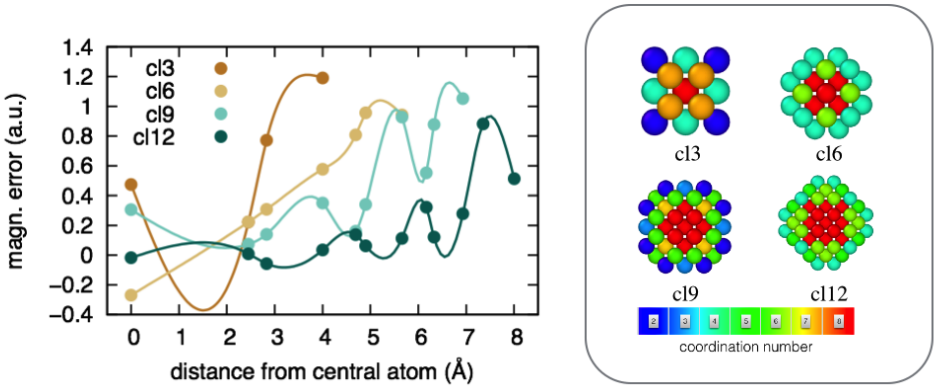

Figure 5.7: Neighbouring shell resolved magnetic moment difference with respect to a bulk structure for clusters of different size at room temperature, and atomistic models of Fe clusters.

The convergence of the cluster QM force for the bulk system is displayed in Figure 5.8. As is clear from panel (b), the convergence is much slower than for Ni-based systems, and a cluster of at least 7 Å radius is required to obtain QM forces accurate within the 0.1 eV/Å threshold, corresponding to clusters of about 137 atoms (9 shells of neighbours). In the case of nickel the same accuracy level is obtained using 43-atom clusters for both γ and γ', as reported in Figure 5.2. Since the scaling of the cost of a DFT calculation with respect to the number of atoms is cubic, QM/MM calculations for Fe systems would be more expensive by one order of magnitude. It is therefore worth trying to accelerate the convergence of the QM force. In this spirit, a non-magnetic (NM) Fe model is simulated, and the same analysis as in the ferromagnetic (FM) case is carried out. These forces are significantly different with respect to the set obtained with the ferromagnetic model. In this case, the convergence is much faster, as shown in Figure 5.8 (a). This indicates that the locality of the QM forces is strongly coupled to the magnetic properties of the system. Constraining the magnetic moment of all the atom to the equilibrium bulk value could therefore accelerate the recovery of the electronic structure of a periodic system.

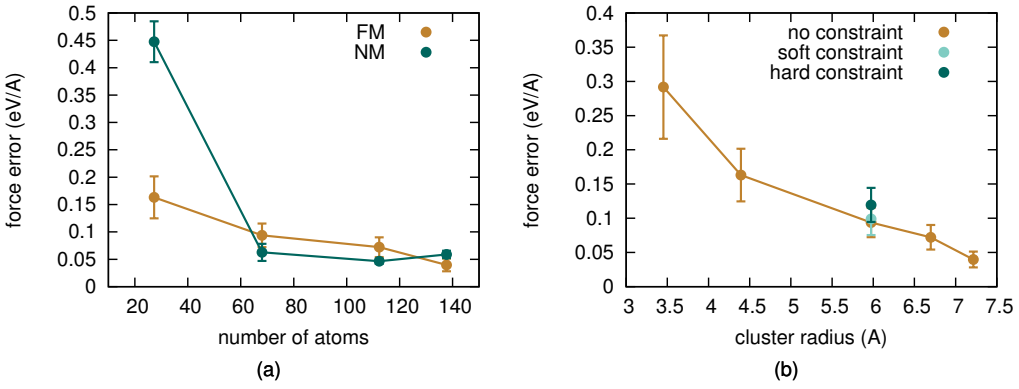

Figure 5.8: (a) Cluster DFT force convergence: comparison between ferromagnetic α iron and a non-magnetic fictitious model. (b) Effect of constraining the magnetic moments of iron atoms.

This kind of calculation is implemented in VASP for the case of non-collinear magnetism, in which the magnetisation density is a vector field. The constraint is applied by adding a penalty term to the total energy of the system, of the form

$$E_p = \sum_{i=1}^{n} \lambda(\mu_i - \mu_{\mathrm{t}}^{(i)})^2 \tag{5.1}$$

where λ is a constant, $\mu_{\mathrm{t}}^{(i)}$ the target magnetic moment for atom i and μ_i the magnetic moment, calculated by atomic orbital projections of the wave-function within a sphere centred on the atomic site i. Calculations are performed for the set of clusters including the first 7 shells of neighbours (89 atoms), and the resulting force error is plotted in Figure 5.8 on top of the original curve for the unconstrained system. Values of $\lambda = 1$ (soft constraint) and $\lambda = 5$ (hard constraint) are used. Remarkably, both these calculations produce larger deviations of the forces from the correct QM target values, as the weight λ is increased to higher values, indicating that the magnetic moment constraint cannot easily be used to speed up force convergence.

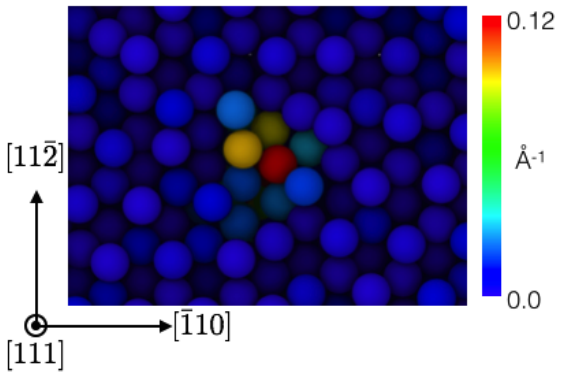

Figure 5.9: Screw dislocation in α-Fe, thermalised at 1200 K using the EAM potential. Atoms are coloured using the screw component of the Nye tensor.

The other approaches for obtaining a faster QM force convergence are tested on the dataset for the dislocated system. The geometry of the core, identified using the Nye tensor analysis, is reported in Figure 5.9. The convergence of the QM force for increasing values of the cluster radius is displayed in Figure 5.10 (a). As in the case of bulk iron, a large cluster, including the first 9 shell of neighbours, is required in order to obtain forces accurate within 0.1 eV/Å from the target values (evaluated in this case on a larger cluster, not shown in the plot). A set of simulations with larger smearing width was also performed. This reduces the error for some intermediate size clusters, but not within the desired threshold. Similarly, adding or removing electrons in a self-consistent fashion does not yield any significant improvement in the convergence of the QM forces, so that achieving occupancy balance of quasi-degenerate surface cluster states by charge addition or depletion (in the ± 5 e range, while using a neutralising background charge density in the DFT calculations) does also not lead to faster force convergence with QM cluster size. This is exemplified by the results shown in Figure 5.10 (a), for a 59 atom cluster at 1200 K, showing an essentially flat force error profile.

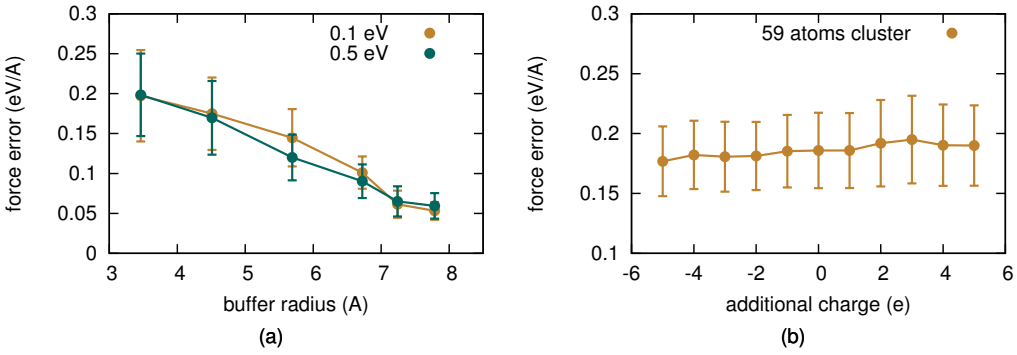

Figure 5.10: (a) Convergence of the cluster DFT force for atoms located at the core of a screw dislocation in α iron for different values of the Gaussian smearing width. (b) effect on adding/removing electrons to the system.

5.5 Convergence of Electronic Properties

In the previous Sections the convergence of QM forces evaluated on subsets of the main systems (clusters) of increasing size is studied. The QM force are meant to be used within the LOTF scheme, presented in Section 2.7, in order to propagate the dynamics of the system describing a certain region, usually defined in the proximity of a crystal defect, with greater accuracy and DFT-level chemical transferability. This approach can be described as the QM-augmentation of a pre-existing MM potential. The goal of this Section is to understand whether it is also possible to obtain information at the electronic level (e.g. charge transfer) using these cluster QM calculations.

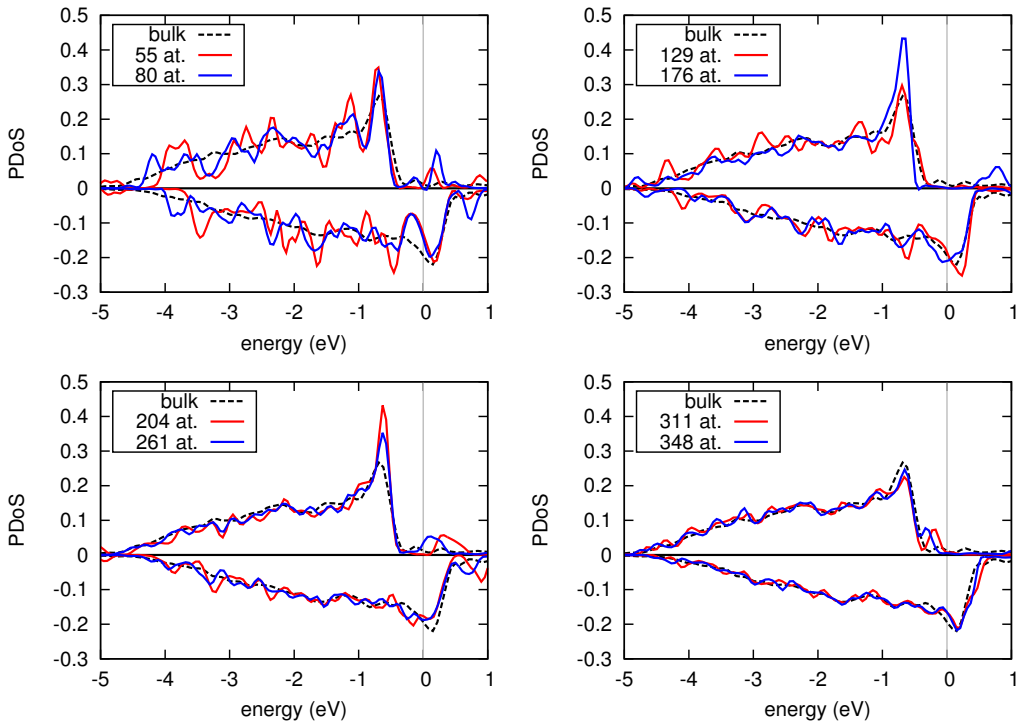

Figure 5.11: Projected density of states for the central atoms of Ni clusters of increasing size. The grey line indicates the Fermi level.

This is particularly important for large systems (1000 or more atoms) for which a full periodic QM treatment is not possible, e.g. the γ/γ' interface including misfit dislocations. The convergence of the overall electronic structure for the central atoms is monitored by studying the PDoS, and in particular its stability at the Fermi level, where surface states are localised. Convergence with respect to the BZ sampling grid is verified, and accurate results are obtained using only the central point Γ. The Methfessel-Paxton smearing scheme is used for PDoS calculations. Bulk PDoS references are evaluated using a $4\times4\times4$ MP grid. The resulting profiles, reported in Figure 5.11 and 5.12 indicate that very large clusters ($\sim$ 300 and $\sim$ 400 atoms for Ni and Fe respectively) are required to converge the electronic structure.

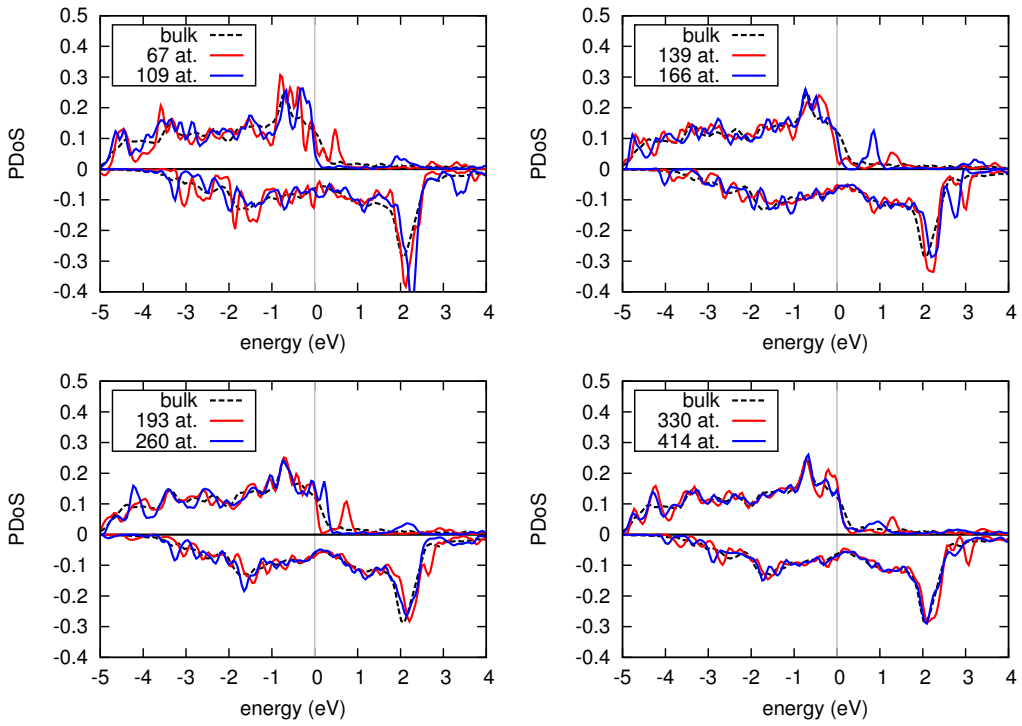

Figure 5.12: Projected density of states for the central atoms of Fe clusters of increasing size. The grey line indicates the Fermi level.

The PDoS of a cluster systems is more localised with respect to the bulk reference, and sharper peaks are therefore observed. Starting from clusters of 176 atoms, the PDoS for the Ni central atom becomes similar to the bulk reference, with the exception a peak at -0.5 eV from the Fermi level. Clusters of at least 311 atoms are required to mitigate this effect, and another smaller peak arises between -0.5 eV and the Fermi level, not observed for the bulk reference profile. For $n = 348$ this peak merges with the previous one, and the PDoS almost overlaps the bulk reference profile.

In the case of α-Fe, a greater instability at the Fermi level can be observed, especially for the spin-up channel. The major peak of bulk Fe, at -0.75 eV from the Fermi level, is split into a series of minor peaks, which crosses the Fermi level for some configurations (cf. blue curve, 260 atoms in 5.12) Clusters as large as 330 atoms still present a double peak, and only by using a cluster of 414 atoms does the PDoS begin to resemble the reference profile.

Another method for monitoring the convergence of electronic properties is studying the convergence of the magnetic moment for the central atoms as a function of the cluster size, for instance by means of Bader analysis. The calculated magnetic moment and force errors with respect to the bulk reference are reported in Figure 5.13. Correlation between the two datasets can be observed in the first part of the curve for iron, as the variation of the magnetic moment between the first two clusters is as large as 0.6 μ_B. When the force converges below the threshold of 0.1 eV/Å (starting from the third cluster, 129 atoms), the oscillations become smoother, with variations smaller than 0.2 μ_B. The force error gets smaller than 0.05 eV/Å for clusters of ~ 200 atoms, and the QM force seem to converge with good accuracy to a value close to the reference one. On the other hand, the magnetic moment error is manifesting an oscillatory behaviour, as observed also in the case of nickel. The force error is lower than 0.05 eV/Å for clusters larger than ~ 250 atoms, while the magnetic moment keeps on oscillating, with variations as large as ~ 0.3 μ_B (50% of the total magnetic moment for a Ni atom).

The results obtained in this Section indicate that the QM clusters used for practical LOTF calculations do not describe with sufficient accuracy the electronic properties of the system. The convergence of these properties seems to be decoupled from the convergence of the atomic forces, which are instead quite stable for clusters of at least 261 atoms in the case of Ni and 193 for Fe. This justifies the approaches taken in Sections 5.3 and 5.4, in which Gaussian smearing with widths as large as 0.5 eV is used in order to minimise the size of the cluster used for the calculation of QM forces. The system does not resemble the bulk reference for clusters of that size, so that the smoothing does not compromise the accuracy of the calculation.

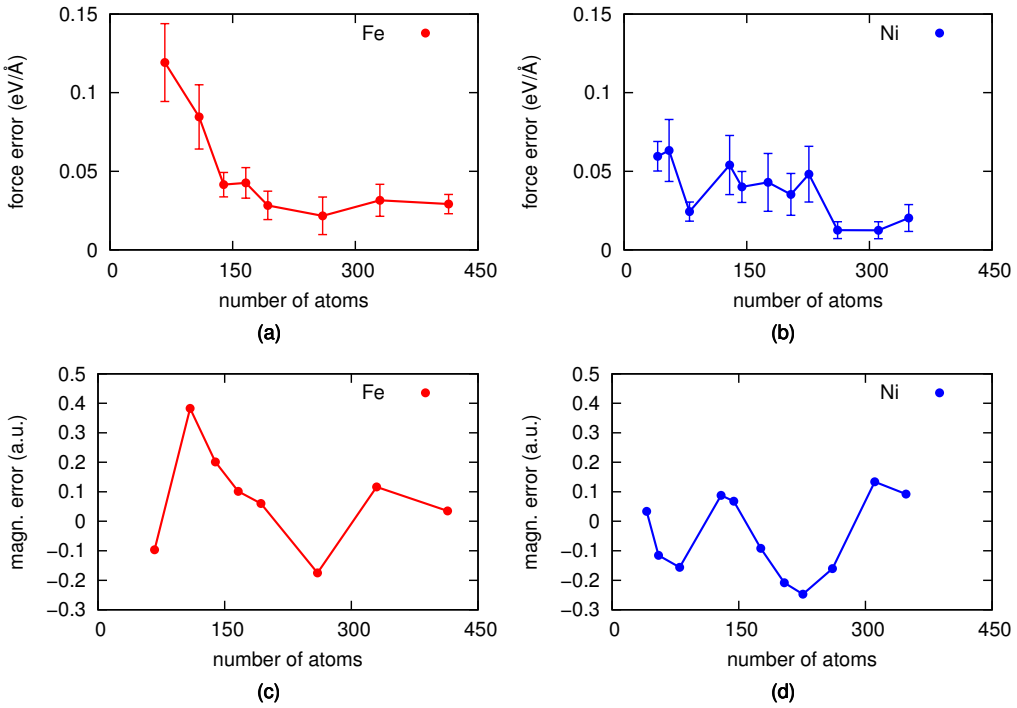

Figure 5.13: QM force (a,b) and magnetic moment (c,d) error for clusters of increasing size in γ-Ni (a,c) and α-Fe (b,d).

5.6 LOTF Simulations of Dislocation Cores

Simulation Set up

In this Section, the LOTF scheme is applied to simulate dislocation glide at a range of temperatures and stresses, for models of the γ phase containing increasing Al percentages, up to a maximum of 15%. A simulation cell containing a quadrupole of screw dislocations is used to model a fully periodic system. This system set-up allows the simultaneous simulation of 8 SP dislocation cores (ensemble parallelism over QM regions), fully exploiting the capabilities of massive parallel architectures. The length of the system along the $[11\bar{2}]$ and the [111] directions is ~ 170 Å, corresponding to a distance of 80 Å between dislocation cores, after dissociation into SPs. The length of the system along the line direction $[\bar{1}10]$ is 5 Å, corresponding to two elementary units. This allows the usege of a 1-dimensional periodic simulation set for DFT force evaluations, greatly accelerating the overall simulation speed. The complete system used for these simulations is shown in Figure 5.14, colouring the atoms using the screw component of the Nye tensor $\alpha_{33}(\mathbf{R})$, $\mathbf{R}$ being the atomic position, emphasising the alternate Burgers vector sign of the quadrupole. A QM region is defined for each partial core, and dynamically updated using this scheme:

1. The system is divided into four separated subregions, each of which contains a full dislocation core. Each region is treated independently.

2. The particles satisfying the condition $\alpha_{33}(\mathbf{R}) > 0.04$ Å^{-1} are selected. The two atoms maximising their respective distance are taken as the first guess of the core positions.

3. The distance d between the SP dislocation cores is calculated and a circular region of radius $d/2$ around each core is selected.

4. For each of the circular regions defined in point 3., the core position is calculated using Equation (4.24).

5. The hysteretic QM selection scheme centred at the dislocation core (cf. Figure 2.4) is used for defining the QM regions. The radii of the circles are selected to be 3 Å and 5 Å (5 Å and 7 Å for high temperature simulations).

6. The buffer region is added using again a hysteretic selection scheme. The radii of the circles are selected to be 5 Å and 7 Å.

7. The core position is used as a starting guess for the next iterative step. Restart from point 3.

In the case of dislocation constriction the distance between the SP dislocation cores becomes comparable to the bond length of the fcc crystal ~ 2.5 Å. As a result, the procedure described in 5.6 (point 3) would select only a single atom, thus making the scheme unable to correctly update the core position (the average (4.24) would always return the starting position of the selected atom). This is addressed by moving apart the initial guess for the core positions 2 Å apart before the selection (point 3). As this is done before the evaluation of the QM cores (point 4), the scheme is still capable of recognising the correct QM region. Note that this adjustment would also prevent complete overlap of the QM regions, allowing the system to recognise a successive re-dissociation into SP without reiterating (point 1,2).

The procedure creates 8 QM systems of about 150 atoms. As the system is periodic along z, a $1\times1\times7$ MP grid is used for BZ sampling, corresponding to four points in the irreducible Brillouin Zone, over which DFT calculations are parallelised. The Nye tensor selection scheme, shown in Figure 5.15 for a pair of SP dislocations, is applied prior every DFT calculation. Accurate testing reveals that, using the LOTF predictor/corrector scheme, a QM calculation is required every 7 integration steps (of 2 fs each) for maintaining the average force error below 0.1 eV/Å through the interpolation of the dynamics.

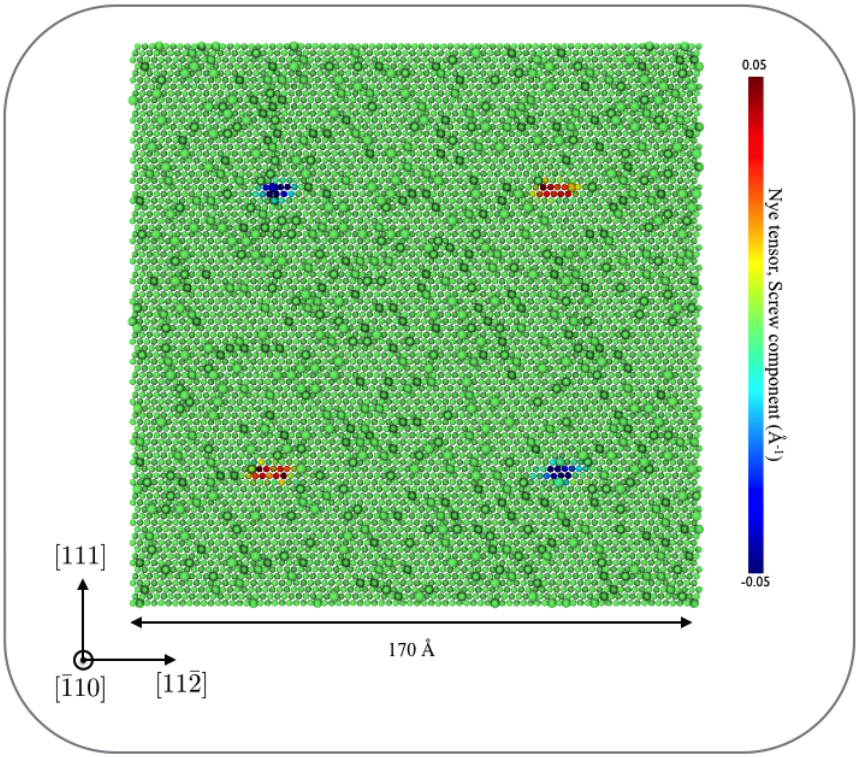

Figure 5.14: Periodic system including a quadrupole of dislocation, used for LOTF dynamics. The orientation of the crystal is indicated, and atoms are coloured by the screw component of the Nye tensor.

In order to set up the temperature conditions, the atomic positions of the system are rescaled to the value predicted by thermal expansion for the target temperature, and the initial velocities distributed according to a Maxwell-Boltzmann function. After a 5 ps thermalisation using the MM potential, a shear strain ϵ_{yz}, where y is the normal to the close-packed family of planes and z the Burgers vector direction, is applied, and the dynamics further propagated for another 1 ps. For high temperature simulations, bad starting points are often encountered because of an unphysically large distance between SP dislocations. In these cases, the MD simulation is continued until a reasonable starting point is encountered.

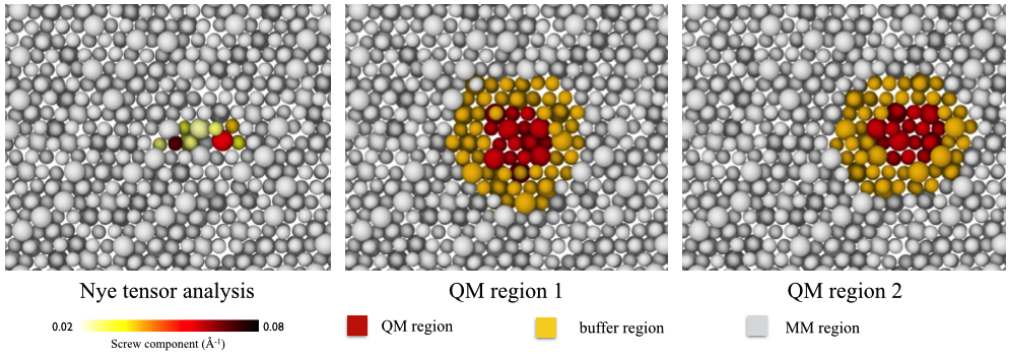

Figure 5.15: Dislocation core identification and definition of QM regions during a LOTF simulation.

Comparison of LOTF and EAM results

As a starting point, a system consisting of pure nickel is simulated, at low temperature and stress conditions (50 K, 100 MPa). The EAM potential is supposed to perform well under these conditions, as a pure phase is simulated. A deviation between LOTF and EAM is observed in the distance between SP, calculated using the previously described method. Its values as a function of simulation time are reported in Figure 5.17 for two pairs of SPs, using a time average to suppress fast oscillations.

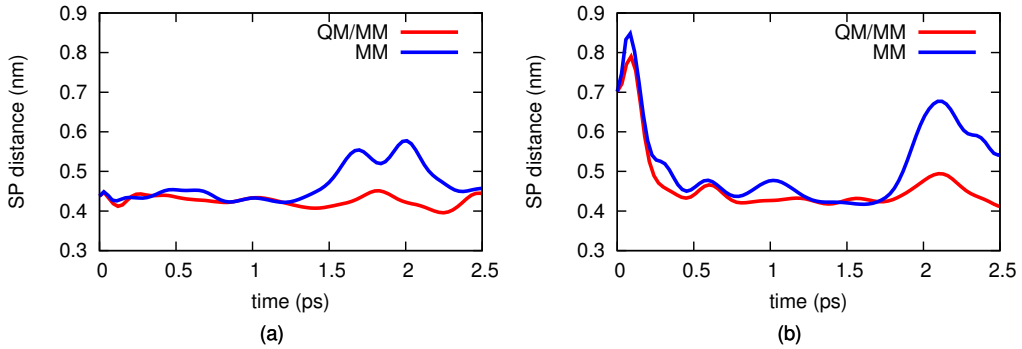

Figure 5.16: Distance between Shockley partials for two extended core regions as a function of time. Comparison between QM/MM and MM results.

While the equilibrium distance is the same ($\sim$ 4.3 Å) in both cases, in accordance with the correct EAM predictions for the elastic constants and the ISF energy (cf. Tables 3.1 and 3.8), larger fluctuations are observed in the MM case. This is attributed to the underestimation of the stiffness for the hcp phase, reported in Section 3.5.

The simulation is then repeated, including 5 % of aluminium in the matrix in order to make the alloy chemistry more complex. Note that the EAM potential is not capable of describing Al impurity atoms correctly, as shown in Section 5.3, and therefore a more significant difference between the QM/MM and the MM calculations is expected. The distance between SP for this calculation is reported in Figure 5.17.

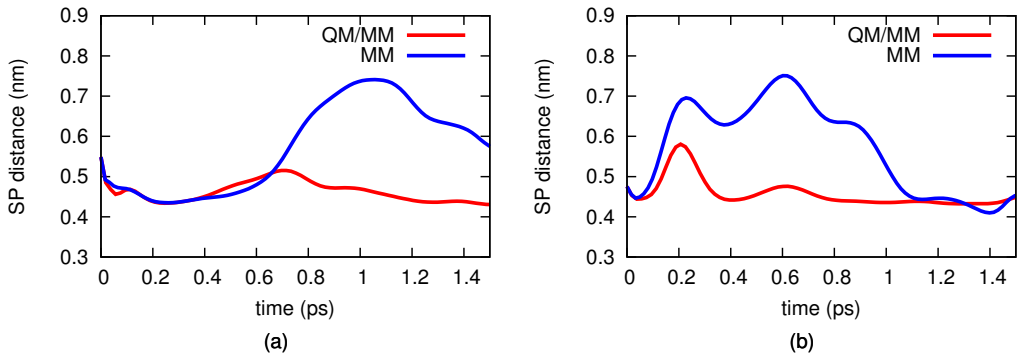

Figure 5.17: Distance between Shockley partials for two extended core regions as a function of time. Comparison between QM/MM and MM results, at low temperature/stress (50 K, 100 MPa) for 5% Al in the matrix.

Its equilibrium value is increased, consistently with the lower value for the ISF energy calculated in presence of impurity atoms (cf. Table 3.10). The new equilibrium value for the LOTF simulation is 4.7 Å. In the MM simulation instead much larger SP distances dominate. This is attributed to an underestimation of the ISF energy for Al impurities, for high Al percentages, reported in Figure 3.13.

When the Al percentage is increased to 15 %, the deviation increases, as shown in Figure 5.18. In panel (a), the distance between SP dislocations linearly increases starting from $t = 0.3$ ps, with an average rate of 2.8 nm/ps. The maximum value reached is 1.9 nm, larger then the expected equilibrium distance by a factor of four. The initial increase of this quantity is physically meaningful, as it is due to an increased presence of Al atoms in the proximity of the extended dislocation core. A similar behaviour is observed also in the LOTF case, however with the smaller expansion rate of 1.2 nm/ps, up to a maximum distance of 0.9 nm, twice as large as the initial equilibrium distance. This can be interpreted as a limitation of the approach, and indicates that larger QM regions might be required for chemically complex alloys. In panel 5.18, the distance between SP dislocation observed using the LOTF scheme is close to the expected value, while in the MM case it converges to a value twice as large.

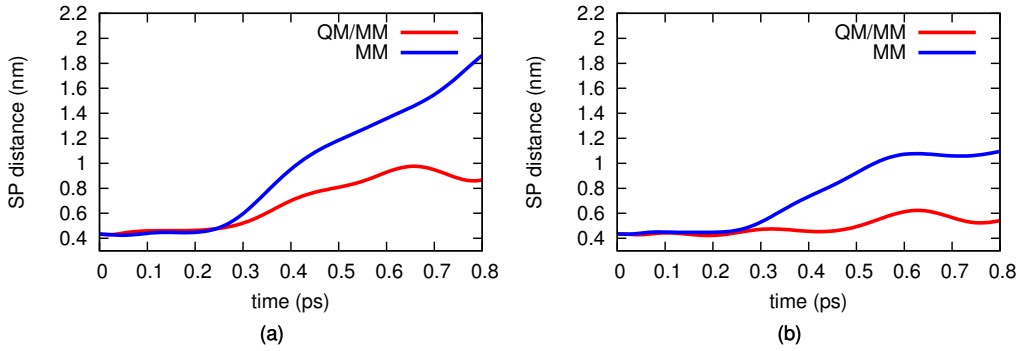

Figure 5.18: Distance between Shockley partials for two extended core regions as a function of time. Comparison between QM/MM and MM results, at low temperature/stress (50 K, 100 MPa) for 15% Al in the matrix.

The simulation temperature is then increased to 1000 K, and the shear stress to 200 MPa. At this conditions, the barrier associated to dislocation constriction can be overcome, and cross-slip can occur, according to the Friedel-Escaig model [29]. The SP distances for LOTF and MM simulations are reported in Figure 5.19, for a Ni matrix containing 5% Al.

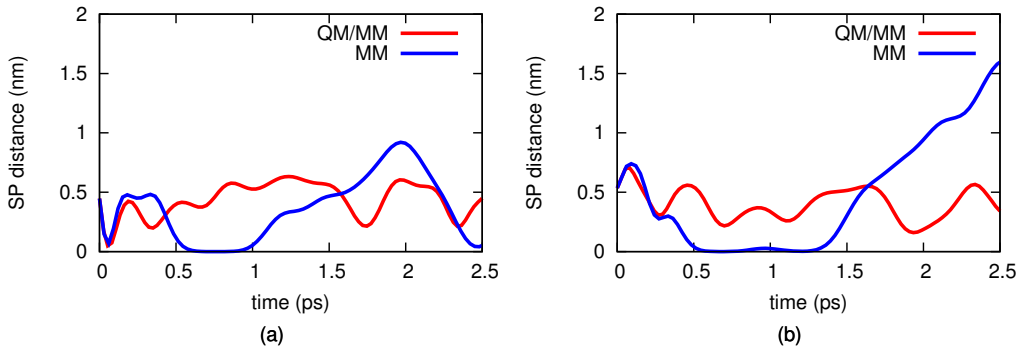

Figure 5.19: Distance between Shockley partials for two extended core regions as a function of time. Comparison between QM/MM and MM results, at high temperature conditions (1000 K, 200 MPa) for 5% Al in the matrix.

Much larger fluctuations are observed in both QM and QM/MM cases, due to thermal disorder. As opposed to the previous simulations set, the MM SP distance is most of the time shorter than the LOTF results, with frequent constriction and cross-slip processes. Large distances are sometimes still observed. In panel 5.19(b), for instance, its value gets as large as 15 Å, with an average expansion rate of 1.33 nm/ps. Selected trajectory frames of the simulation are reported in Figure 5.20. Constriction of SP dislocation is observed in the 0.6 ps frame, while at 0.8 ps the dislocation, still constricted, starts to cross slip. The glide of a perfect screw dislocation is then observed, until at 1.4 ps another cross-slip process occurs, and the dislocation dissociates into SP in a plane of the same family as the starting one. At this point, the distance between partials increases, due to the presence of more Al atoms in the current (111) layer. In the QM/MM case, the distance between SP oscillates, but cross-slip phenomena are not observed. The frequency of cross-slips processes can be used as input parameters to higher scale methods, and it is particular relevant ion order to describe plasticity as this would be the process with the lowest energy cost that would allow the change of slip plane for a screw dislocation.

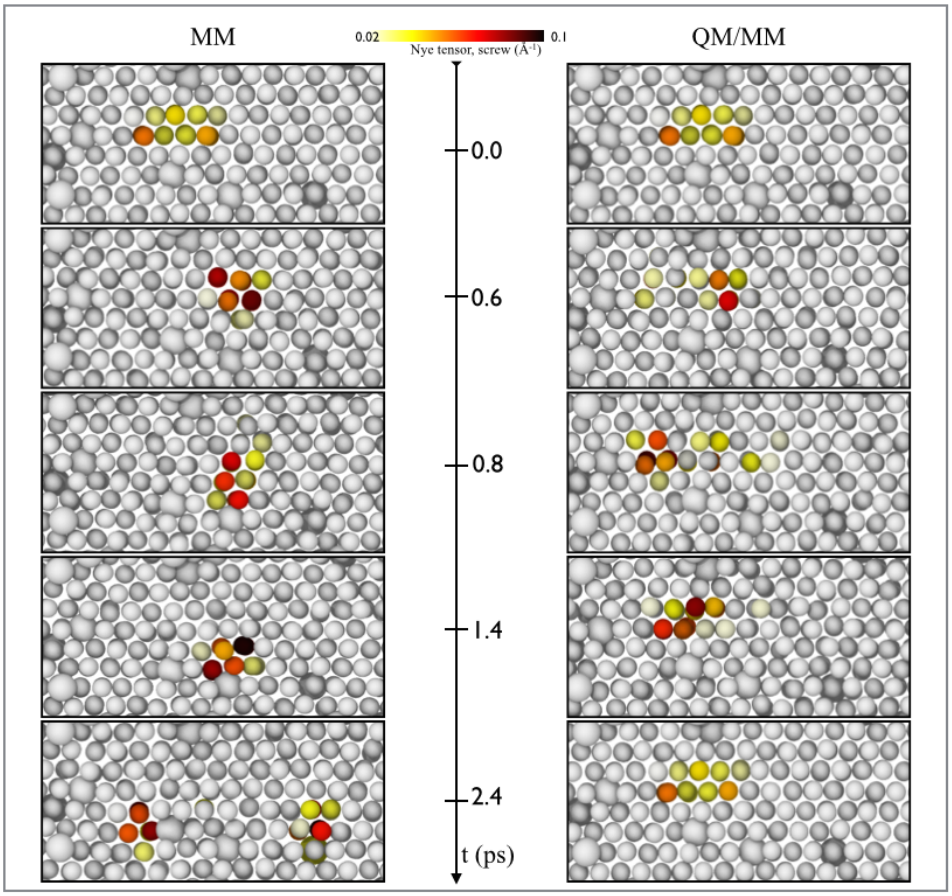

Figure 5.20: Comparison between trajectory frames for a QM/MM and a MM simulation at high temperature conditions (1000 K, 200 MPa 5% Al).

Another set of high temperature simulations was performed, at a larger Al percentage (15 %). In this case cross-slip is never observed with either method and the MM simulations present a distance between Shockley partials consistently larger than the QM/MM value. In one particular case, detailed in Figure 5.21, a maximum distance of 30 Å is observed, corresponding to a 500% error with respect to the LOTF value. This indicates that the EAM potential is not adequate to simulate dislocations at high temperature conditions, especially when the overall chemistry of the system is complex.

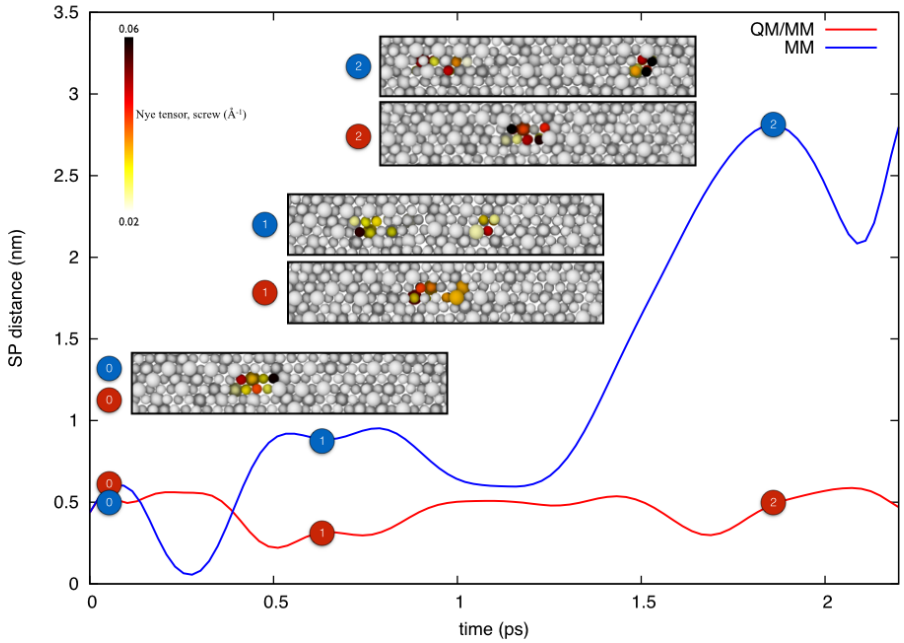

Figure 5.21: Comparison between SP distances and trajectory frames for a QM/MM and a MM simulation at high temperature conditions (1000 K, 200 MPa) for an alloy containing 15% Al.

5.7 Summary

In this Chapter the LOTF method is successfully developed and used for describing the dynamics of SP dislocation in the γ matrix at different conditions. Accurate testing is performed in order to determine the minimal size of the quantum and the buffer region for a selection of crystal defects. This constitutes an excellent starting point for future QM/MM works, as it provides information about the embedding of chemical impurities, fundamental for the design of modern alloys. Moreover, this analysis is extended to the α phase of iron, a more challenging material due to its magnetic properties.

The present work has revealed critical considerations and its extension to metallic system. In particular, it is found that the clusters in use for standard QM/MM calculations are too small for capturing electronic properties, such as the magnetic moment of the QM region. The 'DFT accuracy' claimed to be obtained in LOTF simulation has to be interpreted as accuracy for semi-local quantities, such as the Hellmann-Feynman forces, sufficient to generate accurate trajectories.

Finally, the effects of the lack of chemical transferability of the EAM potential on dislocation cores are observed, both as a function of chemical complexity and of simulating temperature. The QM augmentation of the system proved in most of the cases to be capable of providing an accurate description of the PES for dislocation cores, effectively correcting the local deficiencies of the MM potential. The method can be used for accurate prediction of the dislocation glide velocities or climb rates to be used as inputs for larger scale modelling approaches such as discrete dislocation dynamics.

CHAPTER 6

Future Plans and Conclusion

6.1 Future Plans

The major accomplishment of this thesis is the is the validation of the LOTF scheme for Ni-based superalloys, and the consequent QM/MM simulation of gliding dislocations at different temperature and stress conditions. Using the tools developed here, a variety of calculations can be performed to further investigate the interactions between dislocations and other crystal defects, thus introducing in the model systems some of the chemical complexity typical of realistic materials. In this Section a brief overview of these calculations is provided, some of which are already underway.

Extension to Mixed Dislocations

In Chapter 5 LOTF calculations are performed for the simple case of a screw dislocation in the γ phase. This study can be extended to the case of 60° partial dislocations, relevant to diffusion processes at the γ/γ' interphase boundary, as suggested by experimental evidence in Reference [17].

Preliminary calculations using the EAM potential show that, as previously observed for a screw dislocation (cf. Section 5.6), the distance between SP dislocations increases during the dynamics, as shown in Figure 6.1 by plotting the relevant components of the Nye tensor.

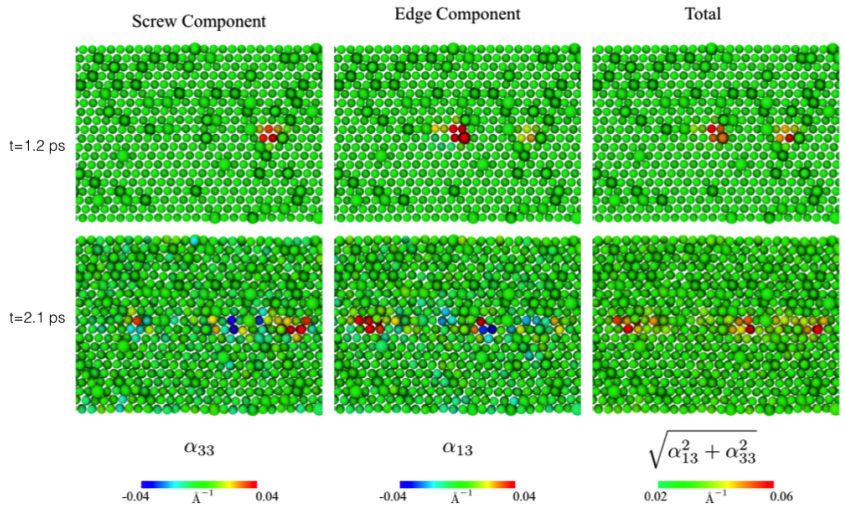

Figure 6.1: Components of the Nye tensor during a classical molecular dynamics simulation at high temperature (1200 K) for a 60° mixed dislocation.

In this case, both the screw and the edge component are relevant, as the two dislocations are not equivalent. The images presented in Figure 6.1 are from a simulation at 1200 K, with no applied strain and 4% Al in the matrix. In the first configuration (top panels) the two partials are clearly distinguishable. One of them presents mainly a screw character, the other one is instead closer to an edge dislocation. This analysis does not provide a complete characterisation of the Burgers vectors, as Nye tensor evaluations do not accurately describe mixed dislocations (cf. Figure 4.7) and because of thermal instabilities, which are shown in Figure 4.10 in the case of a screw dislocation. The tracking of the QM region is therefore more complicated, and different approaches can be used. One can calculate a separate component of the Nye tensor for different dislocations. This would

allow for accurate tracking of dislocations, provided that constriction does not occur, as this would causes a local modification of the Burgers vector surface density. Another possibility is to use the surface density of the modulus of the Burgers vector as α_{mod}, defined as:

$$\alpha_{\text{mod}} = \sqrt{\alpha_{33}^2 + \alpha_{31}^2} \tag{6.1}$$

where α_{33} and α_{31} are respectively the screw and edge components of the Nye tensor for a dislocation whose line is parallel to z, and y is the normal to the slip plane. This quantity would ideally produce symmetric results for the two partials, as can be appreciated in the top-right panel of Figure 6.1. Issues may arise in configurations such as the one shown in bottom panels, in which local Nye tensor dipoles are present. These atoms do not contribute to the total Burgers vector as the Nye tensor contributions integrate to zero, but considering them without taking into account the sign, as in Equation 6.1, would create ill defined QM regions, as is clear from the bottom left panel of Figure 6.1, in which three separate peaks are observed. On the other hand, such configurations might not be observed during a QM/MM simulation, as they are related to an unphysically large distance between SP dislocations. Another possible approach for the defining QM region can be based on the Dislocation Analysis (DXA) technique [13; 180], which reconstruct the full dislocation line, facilitating the identification of kinks and jogs.

A natural extension of this work would be the study of dislocation climb at the γ/γ' interface. The physical process, as described in [84], involve gliding of the screw-like SP dislocation towards the IPB. The edge-like 'trail' dislocation will then be deposited at the interface, where interaction with vacancies will lead to the formation of jogs and eventually to climb. The dislocation will then move along the interface, according to a combination of glide and climb processes (climb-assisted glide), until the corner of the cubic γ' precipitate is reached.

The atomistic modelling of these processes will involve vacancies, necessary for dislocation climb, which will define independent QM regions. Chemical impurities can also be introduced, to increase the chemical complexity of the model, making it more similar to realistic materials. The QM-accurate dynamical study of the effect of Re atoms on the climb of the dislocation can help shed some light on the nature of the 'Rhenium effect', as DFT studies present in literature do not include the typical strains of a γ/γ' interface, nor the actual presence of a dislocation. This study may provide parameters for higher level methods, such as discrete dislocation dynamics, allowing an improved description of plasticity-related processes in superalloys.

Impurity effect on Gliding Dislocations

Another natural extension of the present work includes studying the effect of chemical impurities on a dislocation gliding in the γ phase. An isolated impurity is expected to simply increase the distance between SP dislocations, without hindering in any way the process of gliding, as can be understood from the GSF energy surfaces presented e.g. in Figures 3.14 (a). Whenever the impurity atoms would become neighbours because of dislocation glide, following the same process that leads to the formation of an APB in γ', more complicated energy profiles are observed, as was shown in Figure 3.14 (b).

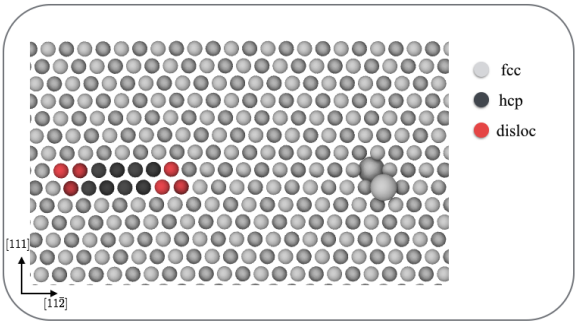

Figure 6.2: Matrix screw dislocation gliding towards chemical impurities.

In particular, different profiles are observed for Al and Re atoms, and it would be interesting to see whether this would cause different effects on the gliding dislocation. The simulation set is shown in Figure 6.2, and it is very similar to the one used in section 4.7 for studying the interaction between a screw dislocation and the interphase boundary. Two separated DFT calculations would be required for the impurity atoms, as the cluster (QM region + buffer) would be too large for standard QM calculations. A dynamical DFT-accurate trajectory for this process would enrich the knowledge of the effect of chemistry on dislocation motion in superalloys, typically not accessible to interatomic potentials.

6.2 Conclusions

In conclusion, this thesis offers a collection of calculations of interest for multiscale atomistic modelling of superalloys.

Electronic structure calculations based on DFT are used to characterise typical defects present in Ni-based superalloys, including vacancies and heavy atom impurities such as Rhenium and Tungsten. The partitioning of these elements to the γ phase is verified, and their effect on the generalised stacking fault energy surface is studied. The latter set of calculations is novel, as only the minima of the curve have been reported in literature, and provides further understanding on their effect on dislocation glide

A classical potential based on the EAM method is used to describe the glide of matrix dislocations, studying the dependance of steady state velocities on temperature and applied stress. Dislocation pinning at the interphase boundary has been verified, and the steps of the process studied focussing on the atomistic details.

Finally, the two simulation methods are coupled, and the first set of DFT-accurate simulations of dislocation glide in γ have been performed. The QM embedding corrects the deficiencies of the classical potential, stabilising the

distance between SP dislocations and thus providing an improved description of dislocation core geometries. This proves that multi-precision QM/MM calculations, despite being orders of magnitude more expensive with respect to the standard EAM approach, provide immediate benefits on the accuracy of MD simulations. The quantities calculated using these methods may be used to parameter higher level models, leading to a more chemically-informed scheme for material modelling. The climb rate of dislocations at the γ/γ' surface can be used for modelling a discrete dislocation dynamics method, placing impurity atoms in the neighbourhood of the dislocation to verify their effect on the mobility of the latter, simulating (i) the correct chemical environment with QM-accuracy and (ii) simulation temperatures relevant to practical applications. The only drawback of the method is the large computation time required. On the other hand, this approach would create large databases of QM-accurate configurations/forces that can be used to inform newly developed machine learning technique (see e.g. Reference [181]).

Concluding, the LOTF method (DFT-level accuracy) has been successfully exported to metallic systems, and in particular to the study of dislocation cores. The accuracy of the method is comparable with *ab initio* MD (0.1 eV/Å versus 0.02 eV/Å force accuracy), but the size of the system simulated can be orders of magnitude larger, provided that the QM zone is well localised. This method can explicitly simulate high temperature conditions, and has full chemical transferability.

Bibliography

[1] Reed R 2006 *The Superalloys: Fundamentals and Applications* (Cambridge University Press)

[2] Durand-Charre M 1998 *The Microstructure of Superalloys* (CRC Press)

[3] Burke K 2012 *J. Chem. Phys.* **136** 150901

[4] Daw M S and Baskes M I 1984 *Phys. Rev. B* **29** 6443–6453

[5] Mishin Y 2004 *Acta Materialia* **52** 1451–1467

[6] Prakash A, Guénolé J, Wang J, Müller J, Spiecker E, Mills M, Povstugar I, Choi P, Raabe D and Bitzek E 2015 *Acta Materialia* **92** 33–45

[7] Csányi G, Albaret T, Payne M C and De Vita A 2004 *Physical Review Letters* **93** 175503

[8] Kermode J R, Albaret T, Sherman D, Bernstein N, Gumbsch P, Payne M C, Csányi G and De Vita A 2008 *Nature* **455** 1224–1227

[9] Dziedzic J, Bobrowski M and Rybicki J 2011 *Physical Review B* **83** 224114

[10] Kresse G and Hafner J 1993 *Physical Review B* **47** 558–561

[11] Kresse G and Furthmüller J 1996 *Physical Review B* **54** 11169–11186

[12] Chamati H, Papanicolaou N I, Mishin Y and Papaconstantopoulos D 2006 *Surface Science* **600** 1793–1803

[13] Stukowski A 2010 *Modelling and Simulation in Materials Science and Engineering* **18** 015012

[14] Williams T and et al C K 2010 Gnuplot 4.4: an interactive plotting program

[15] Hunter J D 2007 *Computing In Science & Engineering* **9** 90–95

[16] Gell M, Duhl D N and Giamei A F 1980 *Superalloys 1980* 205–214
[17] Kolbe M, Dlouhy a and Eggeler G 1998 *Materials Science and Engineering: A* **246** 133–142
[18] Eggeler G and Dlouhy a 1997 *Acta Materialia* **45** 4251–4262
[19] Carroll L J, Feng Q and Pollock T M 2008 *Metallurgical and Materials Transactions A: Physical Metallurgy and Materials Science* **39** 1290–1307
[20] Zhu Z, Basoalto H, Warnken N and Reed R C 2012 *Acta Materialia* **60** 4888–4900
[21] Rae C M F and Reed R C 2007 *Acta Materialia* **55** 1067–1081
[22] Srinivasan R, Eggeler G F and Mills M J 2000 *Acta Materialia* **48** 4867–4878
[23] Yashiro K, Naito M and Tomita Y 2002 *International Journal of Mechanical Sciences* **44** 1845–1860
[24] Zhu T and Wang C Y 2005 *Physical Review B - Condensed Matter and Materials Physics* **72** 1–6
[25] Wu W P, Guo Y F, Wang Y S, Müller R and Gross D 2011 *Philosophical Magazine* **91** 357–372
[26] Voter A F and Chen S P 1986 *Accurate Interatomic Potentials for Ni, Al and Ni3Al* (*MRS Proceedings* vol 82)
[27] Woodward C, van de Walle A, Asta M and Trinkle D 2014 *Acta Materialia* **75** 60–70
[28] Zhu Y, Li Z and Huang M 2013 *Computational Materials Science* **70** 178–186
[29] Hirth J and Lothe J 1992 *Theory of dislocations* (Malabar, FL: Krieger Pub. Co)
[30] Mälzer G, Hayes R, Mack T and Eggeler G 2007 *Metallurgical and Materials Transactions A* **38** 314–327
[31] Yu X X and Wang C Y 2009 *Acta Materialia* **57** 5914–5920
[32] Giamei A F 1978 *AFOSR Annual Report FR-11009*

[33] Karunaratne M, Carter P and Reed R C 2000 *Materials Science and Engineering: A* **281** 229–233

[34] Karunaratne M and Reed R C 2003 *Acta Materialia* **51** 2905–2919

[35] Janotti a, Krčmar M, Fu C and Reed R 2004 *Physical Review Letters* **92** 85901

[36] Giamei A F and Anton D L 1985 *Metallurgical Transactions A* **16** 1997–2005

[37] Diologent F and Caron P 2004 *Materials Science and Engineering A* **385** 245–257

[38] Mottura A and Reed R C 2014 *MATEC Web of Conferences* **14** 01001

[39] Blavette D, Caron P and Khan T 1986 *Scripta Metallurgica* **20** 1395–1400

[40] Wanderka N and Glatzel U 1995 *Materials Science and Engineering: A* **203** 69–74

[41] Warren P J, Cerezo A and Smith G D W 1998 *Materials Science and Engineering: A* **250** 88–92

[42] Rüsing J, Wanderka N, Czubayko U, Naundorf V, Mukherji D and Rösler J 2002 *Scripta Materialia* **46** 235–240

[43] Mottura A, Warnken N, Miller M K, Finnis M W and Reed R C 2010 *Acta Materialia* **58** 931–942

[44] Mottura A, Wu R T, Finnis M W and Reed R C 2008 *Acta Materialia* **56** 2669–2675

[45] Koteski V, Mahnke H E, Belošević-Čavor J, Cekić B and Schumacher G 2008 *Acta Materialia* **56** 4601–4607

[46] Gan B and Tin S 2010 *Materials Science and Engineering: A* **527** 6809–6815

[47] Mottura A, Finnis M W and Reed R C 2012 *Acta Materialia* **60** 2866–2872

[48] Levy O, Jahnátek M, Chepulskii R V, Hart G L W and Curtarolo S 2011 *Journal of the American Chemical Society* **133** 158–163

[49] Maisel S B, Schindzielorz N, Mottura A, Reed R C and Müller S 2014 *Physical Review B - Condensed Matter and Materials Physics* **90** 1–5
[50] Okamoto H 1992 *J. Phase Equilib* **13** 4744
[51] Zhu T, Wang C y and Gan Y 2010 *Acta Materialia* **58** 2045–2055
[52] Krčmar M, Fu C, Janotti A and Reed R 2005 *Acta Materialia* **53** 2369–2376 ISSN 13596454
[53] Danas K and Deshpande V S 2013 *Modelling and Simulation in Materials Science and Engineering* **21** 045008
[54] Mordehai D, Clouet E, Fivel M and Verdier M 2008 *Philosophical Magazine* **88** 899–925
[55] Goswami K N and Mottura A 2014 *Materials Science and Engineering A* **617** 194–199
[56] Schuwalow S, Rogal J and Drautz R 2014 *Journal of physics. Condensed matter : an Institute of Physics journal* **26** 485014
[57] Ma S, Carroll L and Pollock T M 2007 *Acta Materialia* **55** 5802–5812
[58] Shang S L, Zacherl C L, Fang H Z, Wang Y, Du Y and Liu Z K 2012 *Journal of physics. Condensed matter : an Institute of Physics journal* **24** 505403
[59] Rao S, Hernandez C, Simmons J P, Parthasarathy T A and Woodward C 1998 *Philosophical Magazine A* **77** 231–256
[60] Sinclair J E, Gehlen P C, Hoagland R G and Hirth J P 1978 *Journal of Applied Physics* **49** 3890–3897
[61] Rao T A, Parthasarathy C and Woodward S 1999 *Philosophical Magazine A* **79** 1167–1192
[62] Woodward C and Rao S I 2001 *Philosophical Magazine A* **81** 1305–1316
[63] Woodward C and Rao S I 2002 *Physical review letters* **88** 216402
[64] Woodward C and Rao S I 2004 *Philosophical Magazine* **84** 401–413
[65] Cawkwell M J 2005 *Science* **309** 1059–1062
[66] Woodward C, Trinkle D R, Hector L and Olmsted D 2008 *Phys. Rev. Lett.* **100** 45507

[67] Mishin Y, Farkas D, Mehl M and Papaconstantopoulos D 1999 *Physical Review B* **59** 3393–3407

[68] Srinivasan S G, Liao X Z, Baskes M I, McCabe R J, Zhao Y H and Zhu Y T 2005 *Phys. Rev. Lett.* **94**(12) 125502

[69] Trinkle D R 2008 *Physical Review B* **78** 1–11

[70] Trinkle D R and Woodward C 2005 *Science* **310** 1665–7

[71] Leyson G P M, Curtin W a, Hector L G and Woodward C F 2010 *Nature materials* **9** 750–755

[72] Nair A K, Warner D H, Hennig R G and Curtin W A 2010 *Scripta Materialia* **63** 1212–1215

[73] Bernstein N, Kermode J R and Csányi G 2009 *Reports on Progress in Physics* **72** 026501

[74] Zamora R J, Nair A K, Hennig R G and Warner D H 2012 *Physical Review B* **86** 1–5

[75] Henkelman G, Arnaldsson A and Jónsson H 2006 *Computational Materials Science* **36** 354–360

[76] Choly N, Lu G, Weinan E and Kaxiras E 2005 *Physical Review B* **71** 1–16

[77] Svensson M, Humbel S, Froese R D J, Matsubara T, Sieber S, and Morokuma K 1996 *The Journal of Physical Chemistry* **100** 19357–19363

[78] Ligneres V L and Carter E A 2005 An introduction to orbital-free DFT *Handbook of Material Modeling* pp 137–148

[79] Lu G, Tadmor E B and Kaxiras E 2006 *Physical Review B - Condensed Matter and Materials Physics* **73** 1–4

[80] Tadmor E B, Ortiz M and Phillips R 1996 *Philosophical Magazine A* **73** 1529–1563

[81] Liu Y, Lu G, Chen Z and Kioussis N 2007 *Modelling and Simulation in Materials Science and Engineering* **15** 275–284

[82] Nosé S 1984 *The Journal of Chemical Physics* **81** 511–519

[83] Hoover W G 1985 *Physical Review A* **31** 1695–1697

[84] Hafez Haghighat S M, Eggeler G and Raabe D 2013 *Acta Materialia* **61** 3709–3723

[85] Titus M S, Mottura A, Viswanathan G B, Suzuki A, Mills M J and Pollock T M 2015 *Acta Materialia* **89** 423 – 437

[86] Born M and Oppenheimer R 1927 *Annalen der Physik* **389** 457–484 ISSN 1521-3889

[87] Feynman R P 1939 *Phys. Rev.* **56**(4) 340–343

[88] Hohenberg P and Kohn W 1964 *Phys. Rev.* **136**(3B) B864–B871

[89] Kohn W and Sham L J 1965 *Phys. Rev.* **140**(4A) A1133–A1138

[90] Vosko S H, Wilk L and Nusair M 1980 *Canadian Journal of Physics* **58** 1200–1211

[91] Perdew J P and Zunger A 1981 *Phys. Rev. B* **23**(10) 5048–5079

[92] Perdew J P, Burke K and Ernzerhof M 1996 *Physical Review Letters* **77** 3865–3868

[93] Becke A D 1993 *J. Chem. Phys.* **98** 1372

[94] Perdew J P and Schmidt K 2001 *AIP Conference Proceedings* **577** 1–20

[95] Kittel C 1986 *Introduction to Solid State Physics* 6th ed (New York: John Wiley & Sons, Inc.)

[96] King-Smith R D, Payne M C and Lin J S 1991 *Phys. Rev. B* **44**(23) 13063–13066

[97] Vanderbilt D 1990 *Phys. Rev. B* **41**(11) 7892–7895

[98] Blöchl P E, Jepsen O and Andersen O K 1994 *Physical Review B* **49** 16223–16233

[99] Monkhorst H J and Pack J D 1976 *Physical Review B* **13** 5188–5192

[100] Methfessel M and Paxton A T 1989 *Physical Review B* **40** 3616–3621

[101] Marzari N, Vanderbilt D, De Vita A and Payne M C 1999 *Phys. Rev. Lett.* **82**(16) 3296–3299

[102] Mulliken R S 1955 *J. Chem. Phys.* **23** 1833

[103] Lennard-Jones J E 1924 *Proceedings of the Royal Society of London A* **106** 463–477

[104] Baskes M I and Srinivasan S G 2014 *Modelling Simul. Mater. Sci. Eng.* **22** 025025

[105] Baskes M I 1992 *Phys. Rev. B* **46** 2727–2742

[106] Du J P, Wang C Y and Yu T 2013 *Modelling Simul. Mater. Sci. Eng.* **21** 015007

[107] Mishin Y, Mehl M and Papaconstantopoulos D 2002 *Physical Review B* **65** 224114

[108] Purja Pun G and Mishin Y 2009 *Philosophical Magazine* **89** 3245–3267

[109] Bitzek E and Gumbsch P 2005 *Materials Science and Engineering A* **400** 40–44

[110] Haile J M 1992 *Molecular Dynamics Simulation: Elementary Methods* (New York, USA: Wiley)

[111] Rapaport D C 2004 *The Art of Molecular Dynamics Simulation* (Cambridge, UK: Camb. Univ. Press)

[112] Verlet L 1967 *Phys. Rev.* **159**(1) 98–103

[113] Berendsen H J C, Postma J P M, van Gunsteren W F, Di Nola A and Haak J R 1984 *J. Chem. Phys.* **81** 3684

[114] Andersen H 1980 *The Journal of chemical physics* **72** 2384

[115] Adelman S A and Doll J D 1976 *The Journal of chemical physics* **64** 2375

[116] Martyna G J, Klein M L and Tuckerman M 1992 *The Journal of chemical physics* **97** 2635–2643

[117] Leimkuhler B, Noorizadeh E and Theil F 2009 *Journal of Statistical Physics* **135** 261–277

[118] Parrinello M and Rahman A 1980 *Physical Review Letters* **45** 1196–1199

[119] Wolfe P 1969 *SIAM Rev.* **11** 226–235

[120] Armijo L 1967 *Pacific J. Math.* **16** 1–3

[121] Bitzek E, Koskinen P, Gähler F, Moseler M and Gumbsch P 2006 *Physical Review Letters* **97** 1–4

[122] Bulatov V, Abraham F F, Kubin L, Devincre B and Yip S 1998 *Nature* **391** 669–672

[123] Van Der Giessen E and Needleman A 1999 *Modelling and Simulation in Materials Science and Engineering* **3** 689–735

[124] Martinez E, Marian J, Arsenlis A, Victoria M and Perlado J M 2008 *Journal of the Mechanics and Physics of Solids* **56** 869–895

[125] Balint D S, Deshpande V S, Needleman A and Van der Giessen E 2005 *Materials Science and Engineering A* **400-401** 186–190

[126] Peierls R 1940 *Proc. Phys. Soc.* **52** 34

[127] Nabarro F 1947 *Proc. Phys. Soc.* **59** 256

[128] Nieminen R M 2002 *J. Phys.: Cond. Mat.* **14** 2859

[129] Bernstein N and Hess D W 2003 *Phys. Rev. Lett.* **91**(2) 025501

[130] Ogata S, Lidorikis E, Shimojo F, Nakano A, Vashishta P and Kalia R K 2001 *Computer Physics Communications* **138** 143 – 154

[131] Khare R, Mielke S L, Paci J T, Zhang S, Ballarini R, Schatz G C and Belytschko T 2007 *Phys. Rev. B* **75**(7) 075412

[132] Kohn W 1996 *Phys. Rev. Lett.* **76**(17) 3168–3171

[133] De Vita A and Car R 1998 *Mater. Res. Soc. Symp. Proc.* **491** 473

[134] Francis G P and Payne M C 1999 *Journal of Physics: Condensed Matter* **2** 4395–4404

[135] Kresse G 1999 *Physical Review B* **59** 1758–1775

[136] MacDonald J R 1969 *Rev. Mod. Phys.* **41**(2) 316–349

[137] Simmons G W H 1977 *Single crystal elastic constants and calculated aggregate properties* (Cambridge, MA: MIT Press)

[138] Megchiche E H, Pérusin S, Barthelat J C and Mijoule C 2006 *Physical Review B* **74** 1–9

[139] Benedek R, Seidman D N and Woodward C 2002 *Journal of Physics: Condensed Matter* **14** 2877–2900

[140] Pyczak F, Devrient B and Mughrabi H 2004 *Superalloys 2004* 827–836

[141] Melchionna S Ciccotti G and Holian B L 1993 *Molecular Physics* **78** 533

[142] S M 2000 *Physical Review E* **61** 6165

[143] Toulokian Y S, Kirby R K, Taylor R E and Desai P D 1975 *Thermophysical properties of matter thermal expansion* (New York: Plenum Press)

[144] CY H 1989 *Properties of selected ferrous alloying elements* (New York, Washington, Philadelphia, London: Hemisphere Publishing Corporation)

[145] Wang Y, Liu Z K and Chen L Q 2004 *Acta Materialia* **52** 2665–2671

[146] Holender J 1990 *Physical Review B* **41** 8054–8061

[147] Mitrokhin Y, Belash V P, Stepanova N N and Shudegov V 2008 *Journal of Physics: Conference Series* **98** 062036

[148] Payne M C, Stich I, De Vita A, Gillan M J and Clarke L J 1993 *Faraday Discuss.* **96** 151–159

[149] Brenner D 2000 *Physica Status Solidi (B)* **217** 23–40

[150] Zhou Y, Mao Z, Booth-Morrison C and Seidman D N 2008 *Applied Physics Letters* **93** 93–96

[151] Wang Y J and Wang C Y 2008 *Journal of Applied Physics* **104** 9–14

[152] Parsa A B, Wollgramm P, Buck H, Somsen C, Kostka A, Povstugar I, Choi P P, Raabe D, Dlouhy A, Müller J, Spiecker E, Demtroder K, Schreuer J, Neuking K and Eggeler G 2015 *Advanced Engineering Materials* **17** 216–230

[153] Volterra V 1907 *Annales scientifiques de l'école Normale Supérieure* **24** 401–517

[154] Zimmerman J A, Gao H and Abraham F F 1999 *Modelling Simul. Mater. Sci. Eng.* **103**

[155] Siegel D J 2005 *Applied Physics Letters* **87** 121901

[156] Tadmor E and N B 2004 *Journal of the Mechanics and Physics of Solids* **52** 2507–2519

[157] Voskoboinikov R E 2013 *The Physics of Metals and Metallography* **114** 545–552

[158] Paxton A and Sun Y 1998 *Philosophical Magazine A* **78** 85–104

[159] Rodary E, Rodney D, Proville L, Bréchet Y and Martin G 2004 *Physical Review B - Condensed Matter and Materials Physics* **70** 1–11

[160] Bigger J R K, McInnes D A, Sutton A P, Payne M C, Stich I, King-Smith R D, Bird D M and Clarke L J 1992 *Phys. Rev. Lett.* **69**(15) 2224–2227

[161] Bitzek E 2007 *Atomistic Simulation of Dislocation Motion and Interaction with Crack Tips and Voids*

[162] Ismail-Beigi S and Arias T A 2000 *Phys. Rev. Lett.* **84** 1499

[163] Qi Y, Strachan A, Cagin T and III W A G 2001 *Materials Science and Engineering: A* **309–310** 156–159

[164] Sutton A P and Chen J 1990 *Phil. Mag. Lett.* **61** 139

[165] Bilby B, Bullough R and E S 1955 *Proc Roy Soc A* **213** 263–273

[166] Hartley C S and Mishin Y 2005 *Acta Materialia* **53** 1313–1321

[167] Nye J 1953 *Acta Metallurgica* **1** 153–162

[168] Caccin M, Li Z, Kermode J R and De Vita A 2015 *International Journal of Quantum Chemistry* **115** 1129–1139

[169] Leibfried G 1950 *Z. Phys.* **127** 344

[170] Nabarro F R N 1951 *Proc. Roy. Soc. A* **209** 278

[171] Lothe J 1962 *J. Appl. Phys.* **33** 2116

[172] Tittman B and Bommel H 1965 *Physical Review Letters* **14** 296

[173] Nadgornyi E M 1988 *Progress in Materials Science* vol 31 (Pergamon Press)

[174] Brailsford A D 1970 *J. Appl. Phys.* **41** 4439

[175] Brailsford A D 1972 *J. Appl. Phys.* **43** 1380

[176] Olmsted D L, Hector Jr L G, Curtin W A and Clifton R J 2005 *Model. Simul. Mater. Sci. Eng.* **13** 371

[177] Daw M S, Baskes M I, Bisson C L and G W W 1986 *Modeling Environmental Effects on Crack Growth Processes: Proc. Symp.* (Warrendale: Metallurgical Society)

[178] Peguiron A, Colombi Ciacchi L, De Vita A, Kermode J R and Moras G 2015 *The Journal of Chemical Physics* **142** 064116

[179] Makov G and Payne M C 1995 *Phys. Rev. B* **51**(7) 4014–4022

[180] Stukowski A, Bulatov V V and Arsenlis A 2012 *Modelling and Simulation in Materials Science and Engineering* **20** 085007

[181] Li Z, Kermode J R and De Vita A 2015 *Physical Review Letters* **114** 096405